

Multi-Pixel Photon Counter™
characterisation for the T2K near detector
electromagnetic calorimeter

Mark Ward



High Energy Physics Group
Department of Physics & Astronomy

September 2009

Abstract

Multi-Pixel Photon Counters (MPPCs) are a vital component of a suite of detectors used by the Tokai to Kamioka (T2K) experiment, in which over 43,000 are used to read out wavelength shifting fibres. The absolute photon detection efficiency of Multi-Pixel Photon Counters has been measured at wavelengths of 473 nm and 539 nm. These measurements have been performed under two experimental configurations in order to use a pulsed LED, and Y11 wavelength shifting fibre as light sources. Absolute photon calibration was performed using a calibrated Newport optical power meter. Photon scaling was performed using calibrated neutral density filters to accurately control the exposure of the MPPC at the single photon level.

The absolute intrinsic photon detection efficiency is measured to be $30.8 \pm 1.1\%$ at 473 nm exposed to LED light, and a mean of $23.7 \pm 0.5\%$ at 539 nm when exposed to light from Y11 wavelength shifting fibre for an over-voltage of 1.3 V. Both measurements are in good agreement with published specifications. Assuming observed contributions from crosstalk, afterpulse and dark noise increases the observed PDE by a factor of 46%.

The acceptance of the Multi-Pixel Photon Counter to photons when coupled to wavelength shifting fibre is examined for different coupling configurations, in order to understand the observed behaviour of a fibre connector designed for T2K, and to improve the accuracy of absolute photon calibration. An acceptance of $94.0_{-0.010}^{+0.006}\%$ is predicted for direct coupling of a 1 mm diameter fibre with a 1.3 x 1.3 mm active surface through a 400 μm epoxy interface.

The Multi-Pixel Photon Counter is found to operate up to a gain of 1.3×10^6 with a operating voltage range of ~ 2 V. The observed dark count rate of the device is <1 MHz at high gain and <0.77 MHz at 1.3 V for the samples reviewed.

Declaration

The work described in this thesis was carried out in the Department of Physics and Astronomy at the University of Sheffield from October 2005 to September 2009. It is the original work of the author, unless otherwise acknowledged within the text. It has not been submitted previously for a degree at this or any other university.

Mark Ward

September 2009

Acknowledgements

First and foremost wish to thank my supervisor, Lee Thompson, for support, advice and guidance over the the course of these four years and giving me this great opportunity. I would like to thank Antonin Vacheret of Imperial College for his advice and insight throughout my work, and his management of the T2K photosensor group. Thanks to all the people of the Sheffield HEP group, especially Matthew Robinson and Paul Hodgson for their excellent technical support and interesting conversation throughout my time at Sheffield. I am sure I would have been left scratching my head at my computer on many occasions without them.

I wish to extend thanks to the many people I have met or worked with during my PhD, sorry that I cannot mention you all by name, but I will list a few. Hassan, thank you for the many hours spent chatting about a very wide range of subjects which often start out physics related but quickly take U-turns. Thank you Omar for your many insights on, electronics, physics and life. Thank you Ben and Greg for being wonderful office mates and colleagues and for putting up with my constant distractions. Special thanks also to Rangeen, your questions were always welcome, and often made me think more deeply about my work.

I wish to give a heart felt thank you to my parents, for giving me the support and opportunity to follow my passion of Physics from my first undertaking at school through to undergraduate and present. Without your support and dedication I would not be where I am today. Thank you Matthew for being a wonderful brother, for always believing in me and for all the encouragement over the years. Thank you to little Zachary, for always surprising me every time I see you.

Contents

List of Figures	15
List of Tables	21
1 Introduction	23
2 Neutrinos	26
2.1 History	26
2.2 The neutrino and the Standard Model	27
2.3 Solar neutrino observations and the solar neutrino problem	29
2.4 Oscillation Theory	32
2.4.1 Confirmation of oscillation in atmospheric neutrinos	33
2.4.2 Confirmation of oscillation of solar neutrinos by the Sudbury Neutrino Observatory	34
2.4.3 Studying atmospheric neutrinos using neutrino beams	37
2.4.4 Reactor neutrinos	38
2.5 Current parameters	39
3 The Tokai to Kamioka (T2K) experiment	44

3.1	Beamline	45
3.2	The INGRID detector	48
3.3	The 280m near detector	49
3.3.1	Side muon ranging detector	51
3.3.2	Electromagnetic calorimeters	52
3.3.3	π^0 detector	53
3.3.4	Fine grain detectors	55
3.3.5	Time projection chambers	55
3.3.6	ND280 Scintillators	56
3.3.7	Wavelength shifting fibres	57
3.4	Super Kamiokande	59
3.4.1	Backgrounds	62
4	Photosensors	64
4.1	Semiconducting materials	65
4.2	Charge carriers and doping	65
4.3	The p-n junction	66
4.4	Applying bias to the junction	67
4.4.1	Breakdown	68
4.4.2	Temperature dependence	69
4.5	Detecting light	69
4.6	Geiger-mode amplification and quenching	70

5	Geiger-mode avalanche multi-pixel photo-diodes	73
5.1	Schematic design	73
5.2	Gain	74
5.2.1	Temperature dependence of gain	76
5.3	Photon detection efficiency	77
5.3.1	Avalanche probability	77
5.3.2	Geometrical efficiency	78
5.4	Dynamic range	79
5.5	Crosstalk	80
5.5.1	Optical trench	82
5.6	Trapping and afterpulses	83
5.7	Thermal noise	83
5.8	Experimental operation and features	84
5.9	Experimental apparatus	84
5.9.1	Data acquisition	85
5.9.2	Control	89
5.9.3	Experimental environment	92
5.9.4	Data processing and output	93
5.9.5	Data taking and types	96
5.10	GAMPDs Studied	97
5.10.1	Metal Resistive Silicon APD	98
5.10.2	Multi-Pixel Photon Counter	99

5.10.3	SPMMini	100
5.10.4	GAMPD sample list	100
6	GAMPD Parameter extraction	103
6.1	Gain	103
6.1.1	Calculation of the gain with uncertainties	104
6.1.2	Example calculation	106
6.1.3	Experimental study	106
6.1.4	APD triggers binning	107
6.2	Breakdown voltage and APD capacitance	109
6.2.1	Breakdown voltage	109
6.2.2	APD capacitance	109
6.2.3	Experimental study	109
6.3	Dark count rate	110
6.3.1	Pedestal spectrum simulation	112
6.3.2	Simulation result and discussion	117
6.3.3	Dark count rate, crosstalk and afterpulse study	118
6.4	Electronics and the selection of GAMPD for use in T2K	119
6.4.1	CPTA — MRS APD	122
6.4.2	SensL — SPMMini	123
6.4.3	HPK — MPPC	123
7	Golden MPPC for ECal QA	127

7.1	The experimental setup	128
7.2	Temperature and light yield stability	130
7.2.1	Results	130
7.3	Filter and light source calibration	132
7.3.1	Source wavelength spectrum	135
7.3.2	MPPC photon acceptance	136
7.3.3	Preparation and data taking	146
7.3.4	Analysis	150
7.3.5	Results	152
7.4	Conclusion and discussion	156
8	Conclusion	160
	References	163

List of Figures

2.1	Solar neutrino flux spectrum	30
2.2	Observation of atmospheric neutrino flux oscillation by Super Kamiokande .	35
2.3	Artist's impression of the Sudbury Neutrino Observatory	36
2.4	Solar neutrino oscillation parameter plot from the KamLAND experiment .	41
2.5	Atmospheric neutrino oscillation parameter plot from the MINOS experiment	42
2.6	Exclusion plot for Δm_{13}^2 and $\sin^2 2\theta_{13}$ from the CHOOZ experiment	43
3.1	Muon neutrino survival probability	45
3.2	Overview of JPARC neutrino beam	46
3.3	Neutrino beam line at JPARC	47
3.4	Design and layout of the INGRID detector	49
3.5	ND280 : Exploded view	50
3.6	SMRD scintillator bar design	51
3.7	P0Dule layer and the P0D	54
3.8	Energy level diagram showing the scintillation process in organic materials .	57
3.9	Kuraray Y11 Fibre drawing	58

3.10	Kuraray Y11 Fibre drawing	58
3.11	Schematic of the Super Kamiokande detector	60
3.12	Example Super Kamiokande event displays	61
4.1	Schematic, Electric field and potential across a p-n junction	67
4.2	Energy band structure of a p-n junction	68
4.3	Current as function of external junction bias	69
4.4	Photon absorption profile through silicon	71
4.5	Normal and reverse avalanche photo-diode structure	71
5.1	Typical bias chains used with GAMPD and equivalent circuit	74
5.2	Discharge and quenching cycle of a APD in Geiger mode	76
5.3	General dimensions and features of a GAMPD	79
5.4	Effect of decreasing the pixel size on geometrical efficiency	80
5.5	Typical GAMPD linearity curve	81
5.6	Optical trenches with example photon paths	82
5.7	Typical persistence plot of a GAMPD responding to low intensity light pulses	85
5.8	Basic experimental setup	86
5.9	Load resistor and trans-impedance op-amp readout of a GAMPD	86
5.10	Circuit diagram of pre-amplifier using LMH6624	87
5.11	Circuit diagram of pre-amplifier using OPA847	88
5.12	Operation of the Sheffield LED Pulser	90
5.13	Flow chart of LabView Automation Process	92

5.14	Design of the dark-box constructed for GAMPD testing	93
5.15	Fake GAMPD used in charge calibration	95
5.16	Charge calibration example	96
5.17	Typical LED and pedestal charge spectrum	98
5.18	MRS-APD – Pixel design and surface layout	99
5.19	MPPC – Pixel design and surface layout	101
5.20	SiPMmini – Pixel design and surface layout	102
6.1	Example Spectrum	105
6.2	Gain scan for 6 test devices	108
6.3	Gain against over-voltage plot for 6 test devices	111
6.4	Example of dark count rate extraction using a pedestal spectrum (a), (b) shows the pedestal spectrum rebinned in terms of photoelectrons and (c) in integer photoelectron bin, (d) shows the result of a threshold scan using equation 6.7	112
6.5	Pedestal spectrum with	114
6.6	Crosstalk generation diagram	115
6.7	Grid search for Simulation parameters	116
6.8	Final simulation result	117
6.9	Dark count rate and crosstalk + afterpulse fraction for initial test devices	120
6.10	Hamamatsu S10362-13-050C MPPC Packaging design and ECal connector	125
6.11	Temperature Scan of a T2K ECal production MPPC	126
6.12	Breakdown voltage as a function of temperature for a T2K ECal production MPPC	126

7.1	Temperature control stage for use with T2K ECal connector	129
7.2	Experimental Setup for performing Golden MPPC measurements	131
7.3	Temperature and Light yield stability	132
7.4	Wavelength spectrum of Y-11 fibre and Blue pulser LED	136
7.5	LED intensity as a function of angle	137
7.6	Acceptance ratio with cleaved and uncleaved LED and direct comparison of light yield	139
7.7	Example of banding on fibre face due to skew photons	141
7.8	Sample photographs of Y-11 taken at different angles	142
7.9	Angle as a function of Integrated intensity for fibre simulation	142
7.10	Angle as a function of Integrated intensity for fibre simulation	143
7.11	Skew photon dark band radius vs angle	144
7.12	Example fibre simulation visualisation	145
7.13	Fibre acceptance simulation results for 50,000 photons	147
7.14	Acceptance ratio for MPPC with 1 mm fibre	148
7.15	Comparison of light yield from Y11 fibre coupled MPPCs	149
7.16	Darkrate and mean for T2K Devices tested for Golden MPPC calibration .	153
7.17	PDE dataset for device TA3001 exposed to 473 nm LED	154
7.18	Extracted Mean vs expected for fitting and counting methods	155
7.19	PDE of all tested golden MPPCs	156
7.20	Photocurrent PDE data from Hamamatsu	157

7.21 Deviations from linearity for the 1.3 x 1.3 mm MPPC, (a) shows deviation in terms of photoelectrons and (b) shows deviation in terms of input photons¹⁵⁹

List of Tables

2.1	proton-proton chain	29
2.2	Current oscillation parameters	40
3.1	Physical parameters of each ECal module in ND280	52
3.2	Čerenkov energy threshold for electrons, muons and pions in water	62
5.1	Sheffield pulse specifications	90
6.1	Breakdown voltage and capacitance of 6 sample devices during initial testing at 22.0°C	110
6.2	Specifications proposed for photosensors for the ND280 Electromagnetic Calorimeter.	122
7.1	Transmission of Kodak wratten neutral density filters at 473 nm	133
7.2	Summary of all PDE measurements	158

Chapter 1

Introduction

The interplay between the development of science and technology has brought forward many advances in the field of particle physics. It has enabled the construction of more and more accurate equipment and detectors, allowing science to probe deeper and deeper into the fundamentals of the universe. An area of great interest in particle physics is the properties of neutrinos. The neutrino is a lepton, one of the fundamental particles that make up the universe. It has no electromagnetic charge, is extremely light, and only interacts via the weak nuclear force. Neutrinos are so weakly interacting that they are typically able to pass through the Earth without interacting. The detection of this particle is therefore notoriously difficult and requires specially designed detectors with a high target mass. This has made fully understanding the key parameters surrounding their behaviour difficult, and despite the first experimental observation of the neutrino being made over 50 years ago, there are still many features of this illusive particle that are not well understood. This mainly concerns the parameters that define the propagation of the neutrino through space, allowing the neutrinos to spontaneously change flavour over large distance scales.

The Tokai to Kamioka (T2K) experiment is a second generation neutrino beam experiment. It will use a high intensity muon neutrino beam and a suite of detectors to precisely study the content of the beam at a distance of 280 m and 295 km. The detector at 280 m, is known as the Near Detector (ND280). It consists of 5 sub-detectors constructed within a 0.2 T magnetic field. It is designed to incorporate a large target mass with high granularity

readout while losing the smallest possible volume to instrumentation. This design has facilitated the use of a new novel photosensor; the Geiger-mode avalanche multi-pixel photo-diode (GAMPD), also commonly known as the Silicon Photomultiplier [1]. ND280 is primarily constructed of plastic scintillator making up a total of approximately 43,000 optical channels. Large scale instrumentation using this device has never been performed before, ND280 will be the first detector designed to use this new type of photosensor. This type of photosensor is used for its small physical size, high gain, excellent photon counting ability, magnetic field immunity, low power consumption and low cost.

In this thesis, the operating parameters and key features of this photosensor will be discussed in detail with emphasis on the measurement of absolute photon detection efficiency, a key parameter in understanding the signals produced inside the ND280 detector and an important input to MC detector simulations. In Chapter 2, the early history of the neutrino is discussed, starting with its introduction in 1930 to solve a fundamental problem in nuclear physics, the experimental discovery in 1956, and the experiments that followed, attempting to observe neutrinos produced by the Sun. The remainder of the chapter is dedicated to a discussion of the observation of neutrino oscillations in solar and atmospheric neutrinos, with reference to the experiments and measurements that were vital in developing our understanding thus far.

In Chapter 3 the Tokai to Kamioka experiment is discussed, in terms of the physics goals, the muon neutrino beamline and the technology employed to accurately parametrise the beam at Tokai and at Kamioka. The focus of this chapter is to discuss the ND280 detector and the use of a new novel photosensor which is the main subject of this thesis. Chapter 4 serves as an introduction to the photosensors used in ND280, by introducing semiconducting detectors and their basic operation. This provides the background material for Chapter 5 which discusses the photosensor used by T2K in more device specific detail.

Chapter 5 discusses a generic GAMPD, including the design and typical operating features including, gain, photon detection efficiency, and the effects of crosstalk, afterpulsing and dark count within the device. The chapter ends by discussing the basic experimental setup used throughout the initial testing of a sample of 3 devices, detailing experimental apparatus and typical data taking techniques. Chapter 6 follows by presenting each key operating parameter of the GAMPD and how it suitable measurements can be performed

during operation including how they are extracted from a sample dataset. These measurements include the gain, breakdown voltage, APD capacitance and dark count rate for each device under examination. The chapter closes with a discussion of the merits of each device tested and the reasons for the selection of the Multi-Pixel Photon Counter (MPPC) for use in T2K.

Chapter 7 presents the measurement of absolute photon detection efficiency (PDE) of the T2K production MPPC under two operating configurations. The purpose of this is to accurately determine the PDE of the MPPC operating in T2K conditions. This includes a detailed study into the expected operation of the experimental setup and the preparation required to make such measurements. Particular attention is paid to understanding the absolute calibration of the photon source when using an LED and when using wavelength shifting fibre. This is essential for measuring the absolute PDE and requires understanding the acceptance of the MPPC in relation to a calibration detector.

Chapter 2

Neutrinos

2.1 History

The neutrino is a fundamental particle first postulated by Pauli in 1930 [2] in order to solve an apparent non-conservation of energy and angular momentum observed in beta decay. Beta decay had been observed to proceed as in the following reaction,



where n is a neutron, p is a proton and e^{-} is an outgoing electron. It is expected that the electron is produced with the energy released in the decay, and thus produce a delta peak on a measured energy spectrum. However this is not what is observed, and in fact the outgoing electron's energy forms a continuum. Pauli's solution to this observed difference between theory and experiment was to introduce a particle with neutral charge and little or zero mass. This particle was later named by Fermi as the 'Neutrino'. It solved the observed beta decay problem as the total energy of a decay would be shared between the electron and the neutrino allowing for the observed continuum. Despite the neutrino solving the problem with beta decay it remained undetected until 1956. As it is neutral it does not observe the electromagnetic force, and only observes the weak force. This combination results in an extremely low interaction cross-section. With the production of nuclear weapons and the first nuclear reactors, scientists were given high intensity neutrino sources which could allow the observation of this illusive particle.

In nuclear fission reactors, approximately 6 neutrinos are produced per reaction at an en-

ergy scale of 1 MeV, the resulting high intensity of neutrinos produced by a reactor means despite the low interaction cross section, it would become possible to observe neutrinos at a reasonable rate using a large enough detector. Reines and Cowen developed a series of experiments [3] at the Savannah River reactor with the aim of observing inverse beta decay,

$$\bar{\nu}_e + p \rightarrow n + e^+ \quad (2.2)$$

The experiment used 400 l of cadmium chloride dissolved in water, and attempted to detect both products of the above interaction. The positron annihilates with an electron to produce back to back photons, which are detected. The free neutron travels through the detector and is slowed and captured on the cadmium producing photons with at a mean lifetime of 15 μ s. The discovery of the neutrino was announced in 1956.

In 1960 it was proposed that neutrinos existed in different flavour states, counterparts to the electron and muon that also carried lepton quantum charge that must be conserved between generations [4]. This was proposed to explain the reason that the decay of muons into electrons by emitting a photon had never been observed but was theoretically possible. The proposals could be tested by producing neutrinos using a high energy proton beam by producing pions and kaons which then decay to produce neutrinos. In 1962 the neutrino was confirmed in two independent flavours [5].

In 1997 an experiment to observe the ν_τ started taking data. The Direct Observation of the NU Tau experiment (DONUT) used a 800 GeV proton beam to create $D_s^- (D_s^+)$ mesons by colliding the beam with a 1 m tungsten target. These then decay into tau leptons and $\bar{\nu}_\tau/\nu_\tau$ through a cascade process. The experiment aimed to observe tau lepton production by the ν_τ beam using an emulsion and scintillating fibre based detector system. In 1999 the DONUT collaboration announced the observation of 34 ν_τ events [6]. The neutrino had thus been observed in all expected flavours.

2.2 The neutrino and the Standard Model

Leptons are fundamental particles existing in 3 generations of doublets, each 1/2 spin and differing by 1 unit of charge (Unit charge = electron charge). Each generation of lepton carries a generation specific quantum number which is conserved in all interactions. This

is laid out as follows,

$$\begin{array}{c}
 \text{Generation} \\
 \hline
 Q \quad \quad \quad 1 \quad \quad 2 \quad \quad 3 \\
 -1e \quad \left(\begin{array}{c} e \\ \nu_e \end{array} \right) \quad \left(\begin{array}{c} \mu \\ \nu_\mu \end{array} \right) \quad \left(\begin{array}{c} \tau \\ \nu_\tau \end{array} \right) \\
 0
 \end{array} \quad (2.3)$$

In each generation there is a massive lepton, increasing mass across each generation and a mass less neutrino (ν_x). The 2nd and 3rd generation of heavy leptons are unstable and decay to the 1st via the weak interaction mediated by the W boson. Unlike the heavy partners, each neutrino is stable [7], [8].

In the Standard Model there are 6 fermions, known as quarks which have a symmetrical structure to that of the leptons. There are 3 generations of doublets each with fractional charge compared to that of the electron charge. The generations are formed as follows,

$$\begin{array}{c}
 \text{Generation} \\
 \hline
 Q \quad \quad \quad 1 \quad \quad 2 \quad \quad 3 \\
 2/3e \quad \left(\begin{array}{c} u \\ d \end{array} \right) \quad \begin{array}{c} up \\ down \end{array} \quad \left(\begin{array}{c} c \\ s \end{array} \right) \quad \begin{array}{c} charm \\ strange \end{array} \quad \left(\begin{array}{c} t \\ b \end{array} \right) \quad \begin{array}{c} top \\ bottom \end{array} \\
 -1/3e
 \end{array} \quad (2.4)$$

Each quark has a mass which increases with each generation, the up quark being the lightest and the top the heaviest with only the first generation being stable. Each quark can decay via the weak interaction taking one unit step in charge down the generations. Quarks have another property in that each flavour through propagation, exists as a superposition of quark flavours. This property is known as quark mixing. This is due to propagation of quarks proceeding via quark mass eigenstates. As each quark has a different mass, the relative components of each eigenstate of the quark will move out of phase, it is thus possible for the quarks to transform flavour. This mixing is parametrised in the CKM matrix which relates each quark flavour to its component mass eigenstates [7]. This behaviour is not predicted in the lepton sector in the Standard Model, however several experiments conducted between the late 1960's and 2000 showed that in this aspect the Standard Model requires modification.

2.3 Solar neutrino observations and the solar neutrino problem

In 1964 John Bahcall published a model for the nuclear processes that occur within the core of the Sun. By modelling the energy output of the Sun and the thermonuclear processes required to sustain it, the model allowed a prediction of the neutrino flux expected at the earth [9]. An updated version of the predicted neutrino flux spectrum is shown in Figure 2.1. An outline of the proton-proton chain which occurs in the Sun is shown for reference in table 2.1. In the same year the Homestake experiment was proposed by Ray Davis which would attempt to measure the solar neutrino flux at the Earth using a radio-chemical detector.

pp I		
	$p + p$	\rightarrow ${}^2\text{H} + e^+ + \nu_e$
	${}^2\text{H} + p$	\rightarrow ${}^3\text{He} + \gamma$
85%	${}^3\text{He} + {}^3\text{He}$	\rightarrow ${}^4\text{He} + 2p$
pp II		
15%	${}^3\text{He} + {}^4\text{He}$	\rightarrow ${}^7\text{Be} + \gamma$
	${}^7\text{Be} + e^+$	\rightarrow ${}^7\text{Li} + \nu_e$
	${}^7\text{Li} + p$	\rightarrow $2{}^4\text{He}$
pp III		
0.002%	${}^7\text{Be} + p$	\rightarrow ${}^8\text{B} + \gamma$
	${}^8\text{B}$	\rightarrow ${}^8\text{Be}^* + e^+ + \nu_e$
	${}^8\text{Be}^*$	\rightarrow $2{}^4\text{He}$
pp IV / hep		
	${}^3\text{he} + p$	\rightarrow ${}^4\text{He} + e^+ + \nu_e$

Table 2.1: The proton-proton chain including the hep chain

The Homestake detector was of simple design comprising a tank holding ~ 378000 L of perchloroethylene (dry cleaning fluid). The active element of the detector is the chlorine

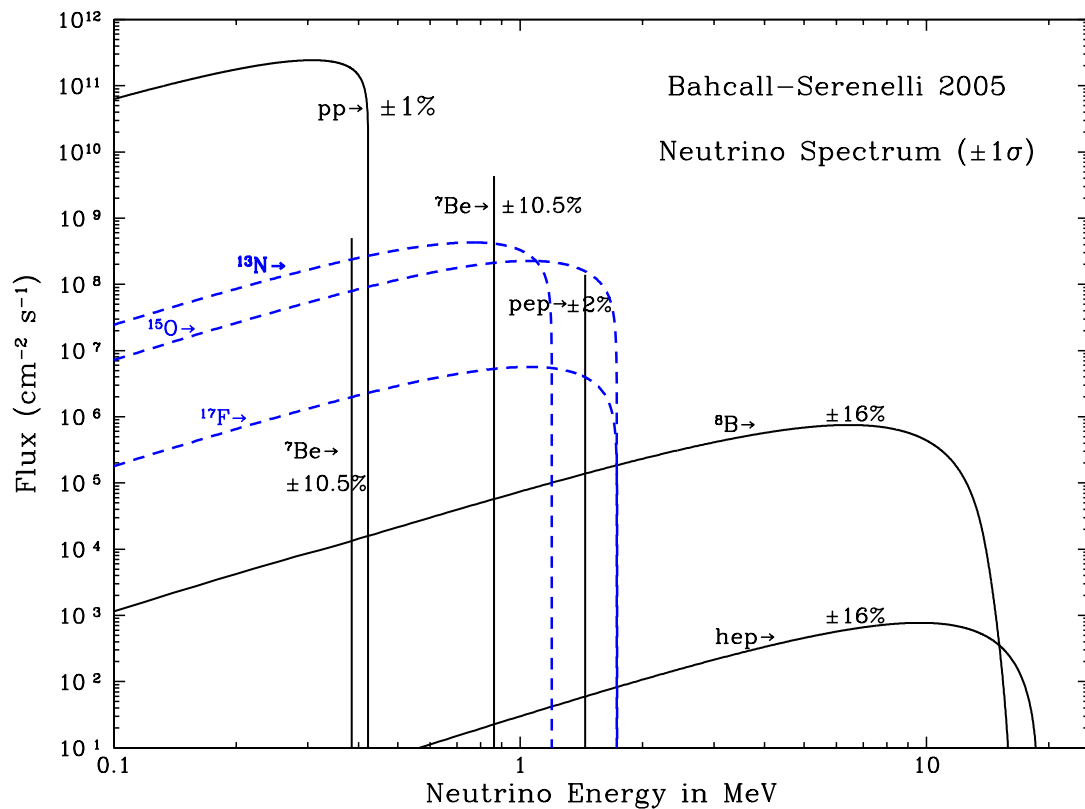


Figure 2.1: Solar Neutrino flux spectrum showing contributions from each process occurring in the sun. The solid lines show the pp chain and the dashed lines show the predicted CNO cycle contributions [10]

contained within the perchloroethylene. Neutrino interactions occur as follows,



The resultant argon atoms were then chemically separated by bubbling helium gas through the tank. ${}^{37}\text{Ar}$ is radioactive and decays via electron capture to produce chlorine and a Auger electron which is then detected. The energy threshold for the primary neutrino interaction with chlorine is 0.814 MeV. This makes Homestake sensitive to mainly ${}^8\text{B}$ neutrinos of the pp III process. Due to the low interaction rate of neutrinos on chlorine, typically less than 1 argon atom is generated per day of running, and thus the experiment would have to take data for many years. After running the experiment for approximately two months the first results displayed a large deficit in the neutrino flux at the Earth [11].

By 1975 after collecting more statistics the data still displayed the same trend observing only a small fraction of the expected neutrino flux from the Sun [12]. This deficit was observed throughout the running of the experiment until it ended in 1993. The final result of the experiment was an mean interaction rate of 2.5 SNU (1 SNU = 1 neutrino interaction per second for 10^{36} target atoms) out of a total expected 8 SNU [13]. This observation became known as the solar neutrino problem.

Several experiments followed the Homestake experiment; Kamiokande [14], a cylindrical water Čerenkov detector built for the purpose of searching for proton decay and two radio-chemical experiments, SAGE in Russia [15] and GALLEX in Italy [16] using Gallium as a target material. Kamiokande was built with the primary aim of searching for proton decay, however one of the major backgrounds proved to be that of neutrino-electron scattering.

$$\nu_x + e^- \rightarrow \nu_x + e^- \quad (2.6)$$

The outgoing electron would move through the water at high velocity, producing Čerenkov as detailed in Section 3.4. An important feature using a Čerenkov detector which is an advantage over radio-chemical techniques is that readout is real time and provides directional information, allowing the reduction of background by only accepting events originating from a specific source. The disadvantage however is that the neutrino energy threshold is much higher at 5 MeV, reducing the expected event rate per tonne of material.

SAGE and GALLEX inferred neutrino interactions from the production of germanium in the following reaction,



${}^{71}\text{Ge}$ is radioactive, and is detected by the capture of an electron and production of Auger electrons in a similar method to ${}^{37}\text{Ar}$ of the Homestake experiment. The advantage of using gallium as a target material is that the threshold of the above interaction is lower (0.2 MeV) than the interaction on chlorine (0.8 MeV) allowing it to probe more of the neutrino flux as shown in Figure 2.1

Despite three different experiments operating with two separate detection methods, the solar neutrino deficit was observed by all experiments, Kamiokande observed $\sim 48\%$ of the expected flux, Gallex $\sim 60\%$ of the expected flux, and Sage $\sim 50\%$ of the expected flux [17].

2.4 Oscillation Theory

In 1969, Pontecorvo postulated the observed deficit in the solar neutrino flux at the earth could be explained if the neutrino exhibited similar behaviour as observed in the quark sector [18]. If the neutrino is not massless as previously assumed, it would be produced and observed in a definite weak eigenstate but would propagate in mass eigenstates. If the neutrino mass is non-zero and each neutrino has different mass, propagation in this way would cause the mass states to move out of phase with each other.

In the two neutrino case, the flavour states of the ν_e and ν_μ are described as a superposition of mass eigenstates ν_1 and ν_2 , defined using a mixing angle θ ,

$$\nu_e = \nu_1 \cos \theta - \nu_2 \sin \theta \quad (2.8)$$

$$\nu_\mu = \nu_1 \sin \theta - \nu_2 \cos \theta \quad (2.9)$$

This can be described as a mixing matrix U,

$$\begin{pmatrix} \nu_e \\ \nu_\mu \end{pmatrix} = \overbrace{\begin{pmatrix} \cos \theta & + \sin \theta \\ - \sin \theta & + \cos \theta \end{pmatrix}}^{\text{U}} \begin{pmatrix} \nu_1 \\ \nu_2 \end{pmatrix} \quad (2.10)$$

by considering the propagation of a single flavour neutrino such as the electron neutrino, equation 2.8 becomes,

$$|\nu_e(t)\rangle = \cos \theta e^{-iE_1 t} + \sin \theta e^{-iE_2 t}, \quad (2.11)$$

$$E_i = \sqrt{p^2 + m_i^2}. \quad (2.12)$$

The probability of neutrino oscillation of an electron neutrino to a muon neutrino is defined as,

$$P(\nu_e \rightarrow \nu_\mu) = |\langle \nu_\mu | \nu_e(t) \rangle|^2 \quad (2.13)$$

$$= \sin^2(2\theta) \sin^2 \left(\frac{\Delta m^2 L}{4E} \right) \quad (2.14)$$

in natural units

$$= \sin^2(2\theta) \sin^2 \left(\frac{\Delta m^2 L(\text{km})}{E(\text{GeV})} \right) \quad (2.15)$$

where θ is the mixing angle and defines the amplitude of the oscillation and Δm^2 is the mass squared difference between the neutrinos ($m_1^2 - m_2^2$) defines the frequency scale of the oscillation. This has implications for the observed solar neutrino flux at the Earth as a neutrino created as an electron neutrino in the heart of the Sun would have a finite probability of being observed as a muon neutrino at the earth. If all three neutrino flavours are considered, the mixing matrix becomes more complex and is referred to as the Pontecorvo-Maki-Nakagawa-Sakata (PMNS) mixing matrix [18] [19],

$$\begin{pmatrix} \nu_e \\ \nu_\mu \\ \nu_\tau \end{pmatrix} = \begin{pmatrix} 1 & 0 & 0 \\ 0 & c_{23} & s_{23} \\ 0 & -s_{23} & c_{23} \end{pmatrix} \begin{pmatrix} c_{13} & 0 & s_{13}e^{i\delta} \\ 0 & 1 & 0 \\ -s_{13}e^{i\delta} & 0 & c_{13} \end{pmatrix} \begin{pmatrix} c_{12} & s_{12} & 0 \\ -s_{12} & c_{12} & 0 \\ 0 & 0 & 1 \end{pmatrix} \begin{pmatrix} \nu_1 \\ \nu_2 \\ \nu_3 \end{pmatrix}, \quad (2.16)$$

where $s_{ij} = \sin\theta_{ij}$ and $c_{ij} = \cos\theta_{ij}$, the δ that appears in the diagonals of the s_{13} is a charge parity violating phase which is yet to be confirmed.

In order to confirm the theory of neutrino oscillation, it is important to detect at least two neutrino flavours from a source, showing a disappearance of one flavour and appearance of another. Solar neutrinos had been observed to disappear, but if oscillation is the cause the expected muon and tau neutrino contributions must be observed. There was also a case of observing neutrinos produced by cosmic rays, as a neutrino flux deficit had also been observed in 1994 by the Kamiokande detector [20].

2.4.1 Confirmation of oscillation in atmospheric neutrinos

The universe provides us with a flux of high energy particles known as cosmic rays that collide with the Earth's upper atmosphere. Cosmic rays are primarily protons, with smaller fractions of helium nuclei, electrons and heavy ions. The primary interaction in the upper atmosphere (for example with a ^{14}N nucleus) produces neutrinos through the production and decay of pions and kaons as follows,

$$\pi^\pm \rightarrow \mu^\pm + \nu_\mu(\bar{\nu}_\mu) \quad (2.17)$$

$$K^\pm \rightarrow \mu^\pm + \nu_\mu(\bar{\nu}_\mu) + X \quad (2.18)$$

$$\mu^\pm \rightarrow e^\pm + \bar{\nu}_\mu(\nu_\mu) + \nu_e(\bar{\nu}_e) \quad (2.19)$$

From these processes it is expected that the ratio of the muon neutrino to electron neutrino originating from the atmosphere of the Earth should be $\sim 2 : 1$ and be independent of the

origin (angle in the sky). However, results from the Kamiokande detector found a deficit of multi-GeV muon neutrinos originating in the atmosphere on the opposite side of the Earth, while observing approximately the expected electron neutrino flux from the same origin. This was further investigated by the Super Kamiokande detector, a unscaled version of the first Kamiokande detector, using 50,000 t of pure water as a target mass [21]. Atmospheric neutrinos were also studied by the IMB detector [22], [23] a cubical shape detector, larger in dimension than the original Kamiokande detector using approximately 9,500 t of pure water. In 1998 the Super Kamiokande experiment announced the observation of the oscillation of muon into tau neutrinos as they pass through the Earth [24], Figure 2.2 shows the observed neutrino flux as a function of angle for both low energy and high energy neutrinos. This was compelling confirmation of neutrino oscillation, as the flux had been measured as a function of angle this gave an estimate of the baseline and including the reconstructed energy Δm_{23}^2 and θ_{23} could be studied. These are often referred to as $\Delta m_{Atmospheric}^2$ and $\theta_{Atmospheric}$. A summary of current measurements and limits is given in section 2.5.

2.4.2 Confirmation of oscillation of solar neutrinos by the Sudbury Neutrino Observatory

The Sudbury Neutrino Observatory (SNO) is a detector designed to be able to detect and determine all the neutrino flavour components originating from the Sun [25]. Although neutrinos from the Sun are low energy (at the MeV scale) and cannot undergo quasi-elastic scattering in order to produce a charged lepton for observation, SNO used a volume of heavy water in order to separate electron neutrinos from all other flavours. The SNO detector uses a 17.8 m diameter spherical frame to support 9438 8 inch photomultiplier tubes. Inside this frame is a 12.0 m diameter spherical acrylic vessel, filled with 1000 t of heavy water. The volume between the acrylic vessel and support frame is filled with water as shown in Figure 2.3.

SNO observed 3 separate types of neutrino interactions,

neutrino scattering,

$$\nu_x + e^- \rightarrow \nu_x + e^- \tag{2.20}$$

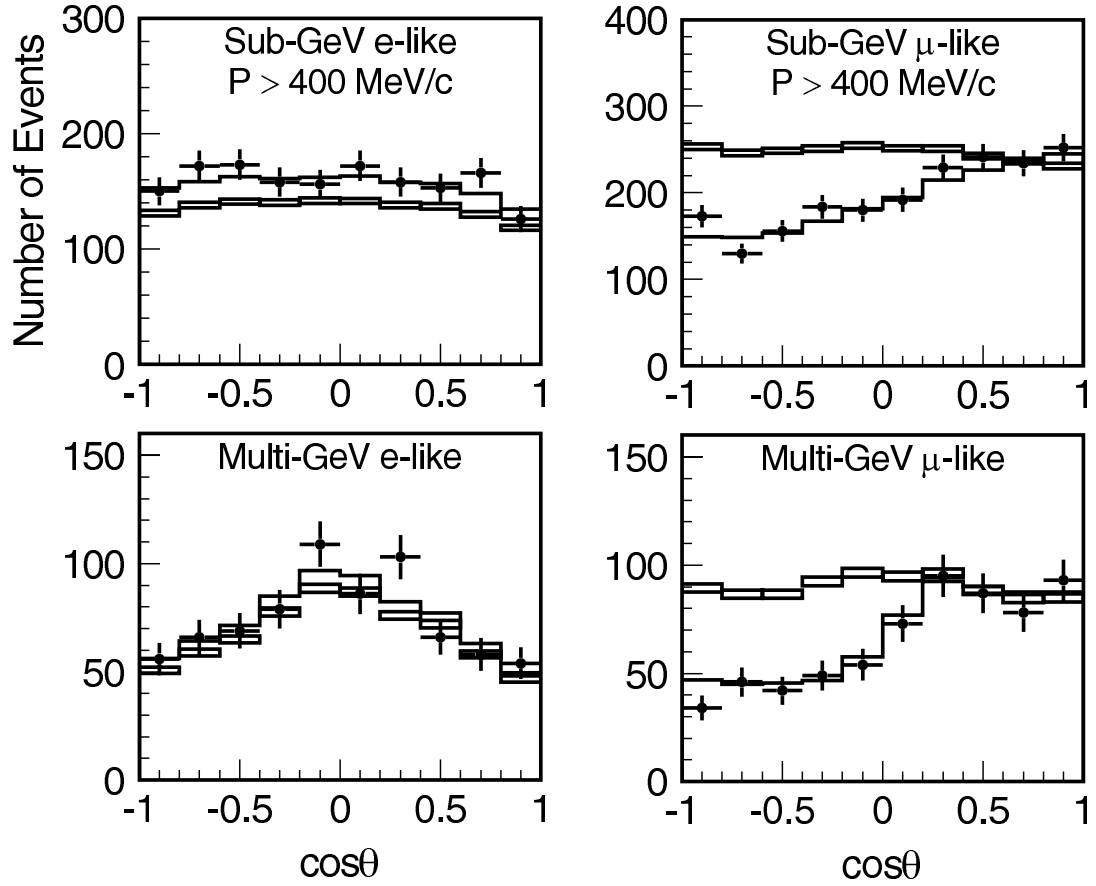


Figure 2.2: Observation of atmospheric neutrino flux oscillation by Super Kamiokande. In each plot the expected neutrino flux assuming no oscillation is shown by boxes, the expected flux assuming oscillation is given by the solid histogram, and data is given by the points. The data shows clear deficit in high energy muon neutrinos originating in the opposite side of the Earth's atmosphere, and little or no corresponding increase in the electron neutrino flux. [24]

charge current absorption,

$$\nu_e + d \rightarrow e^- + p + p \quad (2.21)$$

neutral current disintegration

$$\nu_x + d \rightarrow \nu_x + n + p \quad (2.22)$$

where ν_x is any flavour neutrino.

Each of the above is detected through the production of Čerenkov photons by the outgoing electron in neutrino scattering and absorption. In the case of neutral current interactions,

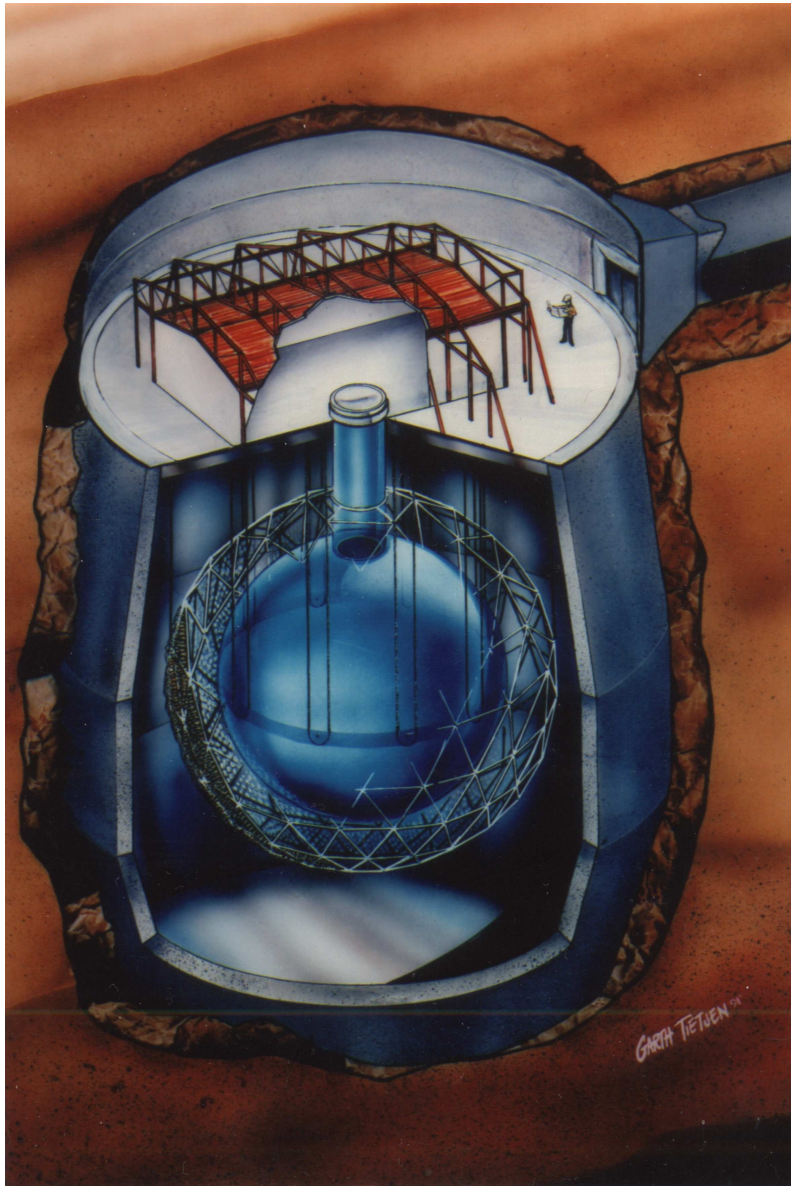


Figure 2.3: Artist's impression of the Sudbury Neutrino Observatory, showing the support frame and inner acrylic vessel

the event is characterised by the capture of the neutron on deuterium, which produces a tritium and a 6.25 MeV photon. Electron scattering is sensitive to all flavours, however is 6.5 times less sensitive to muon and tau neutrinos. In a later stage of the experiment chlorine salt was added to the heavy water in order to increase the neutron capture cross section by a factor of 3. The neutron capture on chlorine also releases multiple photons with a total energy of 8.6 MeV.

Separating these interactions allowed SNO to measure the exact electron neutrino component of the total flux of the Sun. In 2001 the SNO collaboration announced evidence of the direct measurement of the total neutrino flux from 8B neutrinos from the Sun [26], the measured electron scattering flux was consistent with that observed by Super Kamiokande and the neutral current event rate was found to be consistent with what is expected from the Standard Solar Model. The different flux measured in each channel hence shows that electron neutrinos are oscillating into other flavours.

The final flux measurement [27] made by SNO is,

$$\Phi = 5.50^{+0.33}_{-0.31}(\text{stat})^{+0.36}_{-0.34}(\text{syst}) \times 10^6 \text{cm}^{-2} \text{s}^{-1}, \quad (2.23)$$

with an expected flux from the standard solar model of

$$\Phi = 5.05^{+1.01}_{-0.81} \times 10^6 \text{cm}^{-2} \text{s}^{-1}. \quad (2.24)$$

Solar neutrino experiments are used in order to study Δm_{12}^2 and θ_{12} parameters, these are often referred to as Δm_{solar}^2 and θ_{solar} . A summary of current measurements and limits is given in Section 2.5.

2.4.3 Studying atmospheric neutrinos using neutrino beams

The value of Δm_{23}^2 and θ_{23} may also be studied using man-made muon neutrino beams. In order to do this, a collimated neutrino beam of a single flavour and energy is required. The beam must then be parametrised close to the source and then again after a set baseline distance. Both the K2K experiment in Japan [28] and the MINOS experiment in the US [29] use proton beams to generate neutrinos by colliding with a target to produce pions. The pions are focused using a magnet horn and then allowed to decay to produce a beam of muon neutrinos.

K2K used a 12 GeV proton beam to produce muon neutrinos with a mean energy of 1.4 GeV at in the KEK facility in Tsukuba Japan. Before leaving the experimental site the beam is passed through a system known as the ‘Front detector’ 300 m downstream, that consists of a 1 kt water Čerenkov detector, behind which a fine grain detector composed of scintillating fibre is positioned. Behind the fine grain detector is an arc of lead glass and a muon monitor used to identify beam components and measure the muon energy spectrum.

The beam then continues to the Super Kamiokande detector, where it is parametrised after oscillation [30]. K2K was able to measure oscillation parameters with a best fit value of Δm_{23}^2 as $2.8 \times 10^{-3} eV^2$ when $\sin^2 2\theta_{23} = 1$ [31].

MINOS uses a 120 GeV proton beam to produce muon neutrinos with a distribution of energy ranging from 2 - 25 GeV with a peak energy of 10 GeV and at the Fermilab facility in the US. The beam is first passed through a near detector at a distance of 290 m from the source. This detector is constructed from strips of scintillator read out using wavelength shifting fibres interleaved with steel plates. The beam is directed towards the Soudan mine, 730 km away, where a far detector parametrises the beam after oscillation. The far detector has a similar construction to the near detector, it is formed from 485 8 m diameter hexagonal layers of 2.54 cm thick magnetised Iron plates, interleaved with with 4 cm wide scintillator strips. In 2008 MINOS reported $\Delta m_{23}^2 = (2.43 \pm 0.13) \times 10^{-3} eV^2 (68\%CL)$ and $\sin^2 2\theta_{23} > 90$ [32].

2.4.4 Reactor neutrinos

Experiments have also looked at oscillation signatures from neutrinos produced by nuclear fission in reactors around the world. The primary goal of these experiments is to observe electron neutrino disappearance with the aim of measuring Δm_{13}^2 and θ_{13} . Experiments such as KamLAND [33] in Japan and CHOOZ in France [34] have set world limits on parameter, θ_{13} in particular as it is a sub dominant process which is thought to be very close to zero, a summary of all current data on θ_{13} can be found in [35]. The current best limit on the parameter is $\sin^2 \theta_{13} \approx 0.016 \pm 0.010$.

There are a number of planned experiments to continue measuring reactor neutrinos, such as Double-CHOOZ [36] which will use two identical detectors placed at 400 m and 1.05 km from the Chooz reactor in France. Each detector is composed of 2 cylindrical volumes. The innermost is the main target and is filled with liquid scintillator. Surrounding the inner volume is a non-scintillating buffer. The inner tank will be instrumented using photomultiplier tubes to collect scintillation light following neutrino interactions.

The Daya-Bay experiment [37] will use 6 reactor cores in its final phase to generate neutrinos at Daya Bay and Ling Ao in China. The cores will be observed using two pairs of

near detectors at approximately 400 m from the near the two reactor sites and a group of far detectors positioned at 1.4 km. All detectors will have identical designs and will primarily detect neutrino interactions in tanks of liquid scintillator surrounded by water Čerenkov modules. Each detector has the option of being moved along tunnels underground, allowing them to be operated in many configurations to study the parameter space.

2.5 Current parameters

Many experiments have been performed during the 1990's to the present day, all aiming to measure the key neutrino oscillation parameters to an increasing level of accuracy. A small number of these have been discussed for the purpose of motivating an experiment which is nearing first data taking in Japan, the Tokai to Kamioka (T2K) experiment.

Figure 2.4 shows the most recent solar neutrino oscillation results presented by the KamLAND experiment [38]. This plot shows both the global neutrino accepted region and the accepted region produce by the KamLand experiment. A combination of all datasets produces the worlds current best fit measurement as presented in Table 2.2

Figure 2.5 show the most recent atmospheric neutrino results from the MINOS long baseline experiment [32], It shows the progression of early MINOS data and the current measurement with those made at Super Kamiokande and K2K. $\sin^2 2\theta$ is currently thought to be maximally mixed and often quoted as a limit of >0.9

Figure 2.6 show an exclusion plot produced in 2003 by the CHOOZ experiment [39]. Due to $\sin^2 \theta_{13}$ being subdominant, it has not currently been precicely measured. However by combining the measurements made on $\sin^2 \theta_{13}$ from all experiments to date, it is suggested that $\sin^2 \theta_{13}$ is non zero but very small [40].

A total summary of the current best fit parameters with their limits are given in table 2.2

The T2K experiment aims improve the current measurement of Δm_{23}^2 and $\sin^2 \theta_{23}$ to a precision of $10^{-4}(\text{eV}/c^2)^2$ and 10^{-2} respectively and to place a limit on the value of $\sin^2 \theta_{13}$ one order of magnitude greater than current limits. The T2K experiment will be

	lower limit	best fit	upper limit
$\Delta m_{12}^2 (10^{-5} eV^2)$	7.38	7.59	7.80
$\Delta m_{23}^2 (10^{-3} eV^2)$	2.30	2.43	2.56
$\sin^2 \theta_{12}$	0.30	0.32	0.35
$\sin^2 \theta_{23}$	0.34	0.44	0.62
$\sin^2 \theta_{13}$	0.06	0.016	0.026

Table 2.2: Current oscillation parameters [38], [32], [40]

discussed in detail during the next chapter, focusing upon the technology employed to achieve these physics goals.

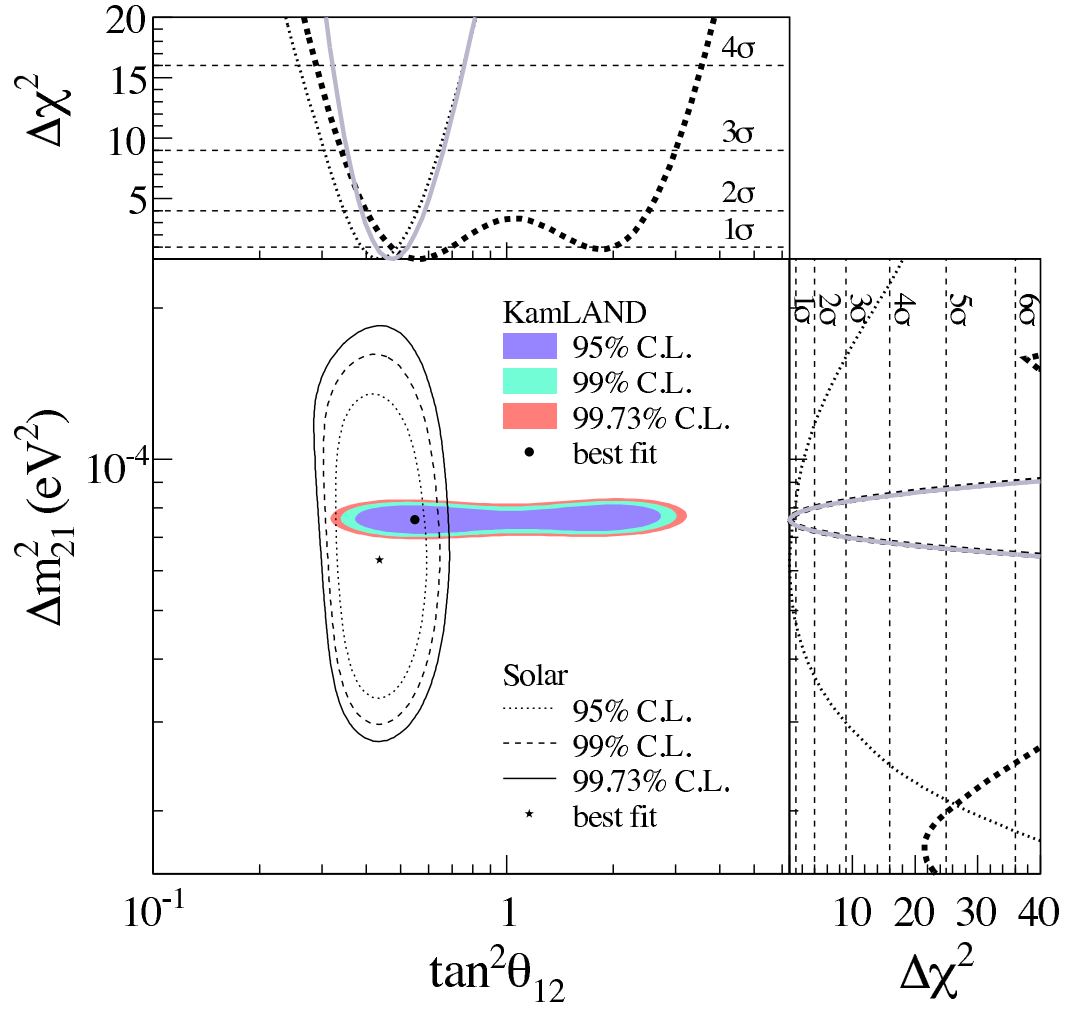


Figure 2.4: Solar neutrino oscillation parameter plot from the KamLAND experiment. The accepted parameter region as measured by the KamLAND experiment is shown in coloured confidence bounds. In black is shown the current accepted solar neutrino experiments accepted parameters [38]

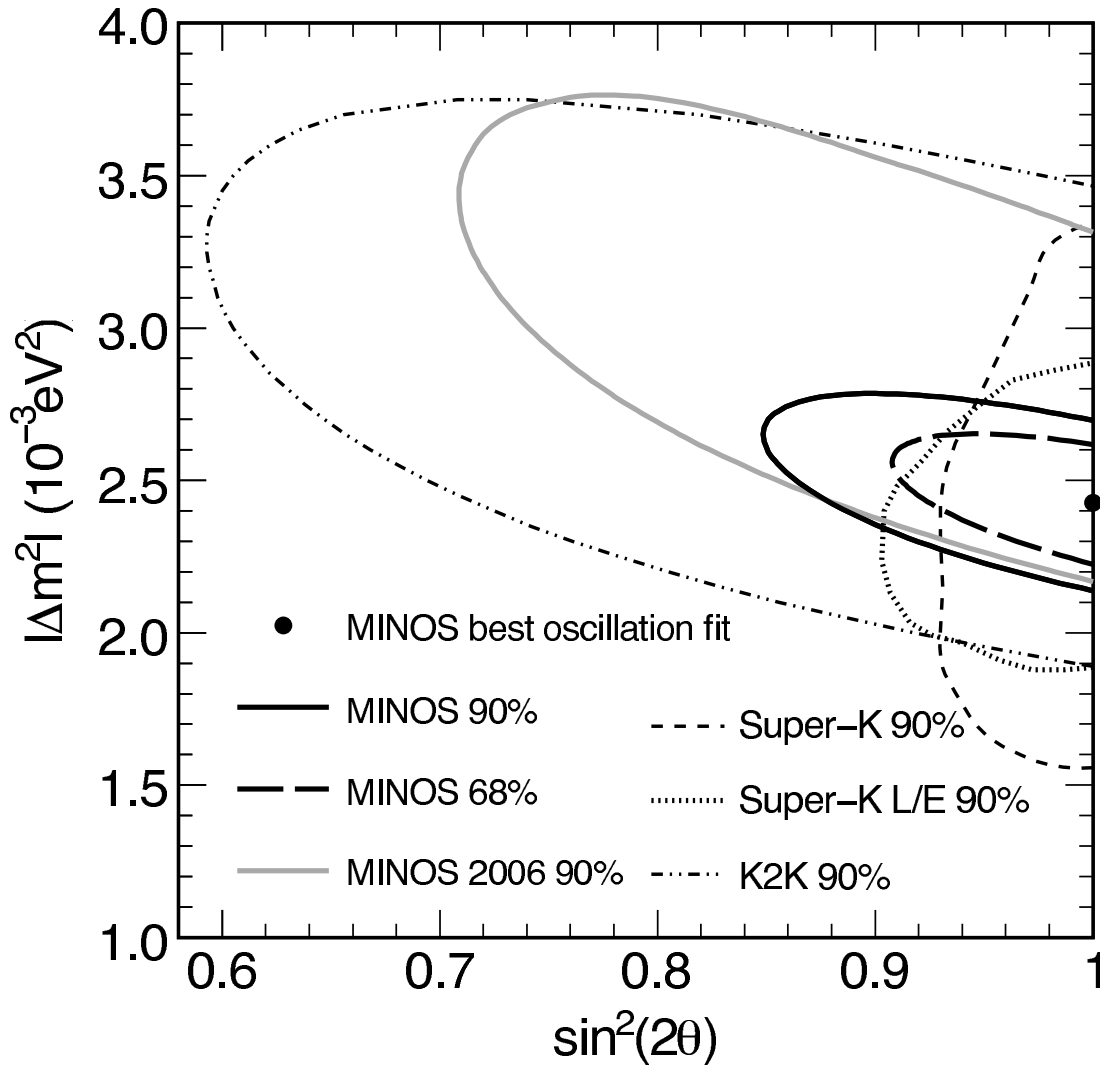


Figure 2.5: Atmospheric neutrino oscillation parameter plot from the MINOS experiment. Included on the plot is the latest results of measurements made at Super Kamiokande and of the K2K experiment. [32]

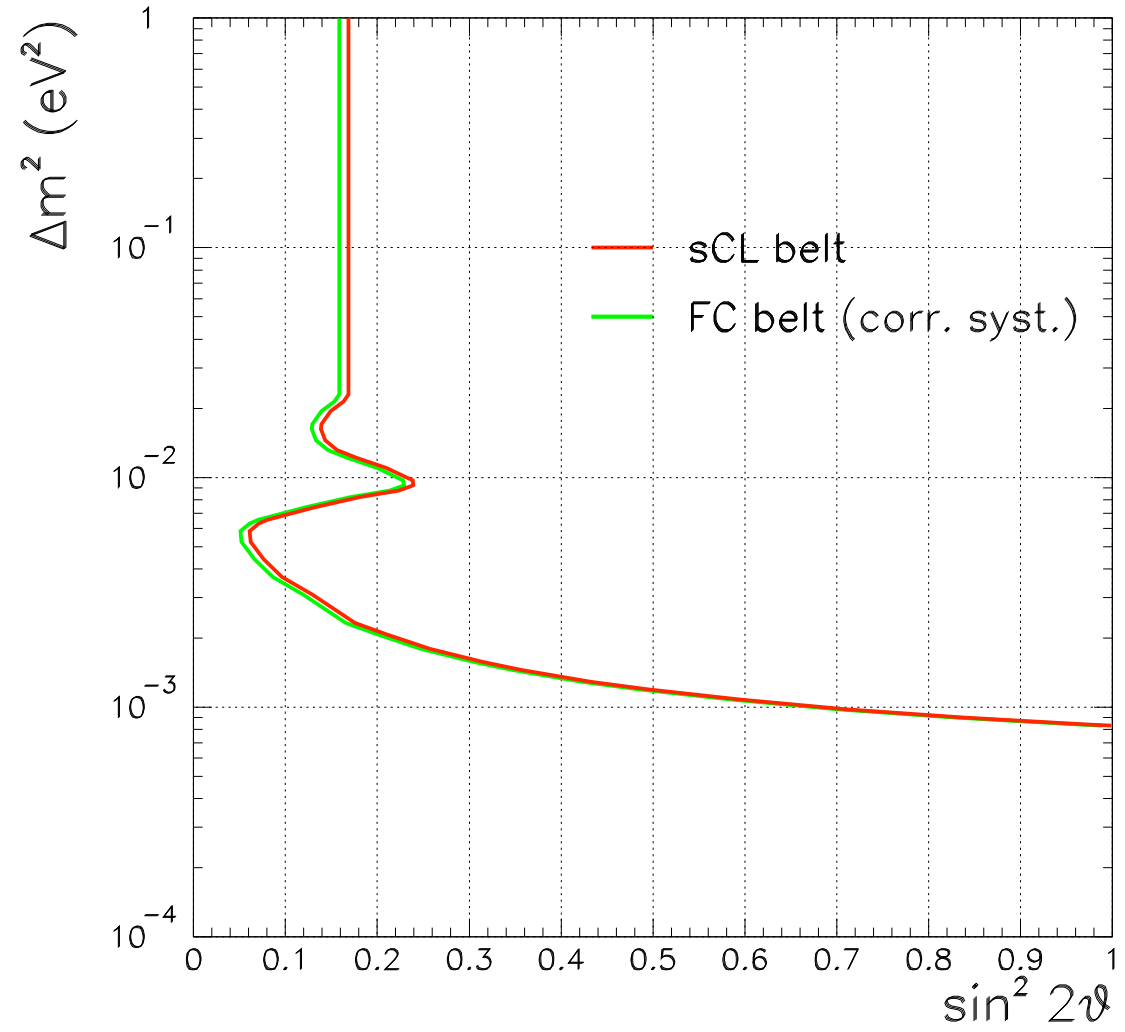


Figure 2.6: Exclusion plot for Δm^2_{13} and $\sin^2 2\theta_{13}$ from the CHOOZ experiment [39]

Chapter 3

The Tokai to Kamioka (T2K) experiment

The T2K experiment is the first of a second generation of long baseline neutrino beam experiments. It will use a high intensity proton beam, constructed at the Japan Proton Accelerator Research Complex (JPARC) in Tokai on the east coast of Japan to produce muon neutrinos. The experiment will have a baseline of 295 km determined by the distance between the beam source in Tokai and the Super Kamiokande detector, a water Čerenkov detector famous for observing neutrino oscillations in solar and cosmic neutrinos [24]. The mean muon neutrino energy produced by the JPARC facility for the T2K beamline will be 0.7 GeV. This configuration is chosen to place the Super Kamiokande detector at a muon neutrino survival ($\nu_\mu \rightarrow \nu_\mu$) minimum. The survival probability is shown as a function of the ratio L/E for current parameters in Figure 3.1 using Equation 2.15. This is for the purpose of T2K achieving the main physics goals which are,

- to determine Δm_{23}^2 and θ_{23} from muon neutrino disappearance in the beam signal;
- to measure θ_{13} by observing electron neutrino appearance signal.

These goals will require the precise understanding of the neutrino beam produced by the JPARC beamline and the determination of key backgrounds to the parametrisation performed at Super Kamiokande. In order to do this, T2K will use a purpose-built near detector system positioned at 280 m (ND280) downstream of the beam. ND280 is a mag-

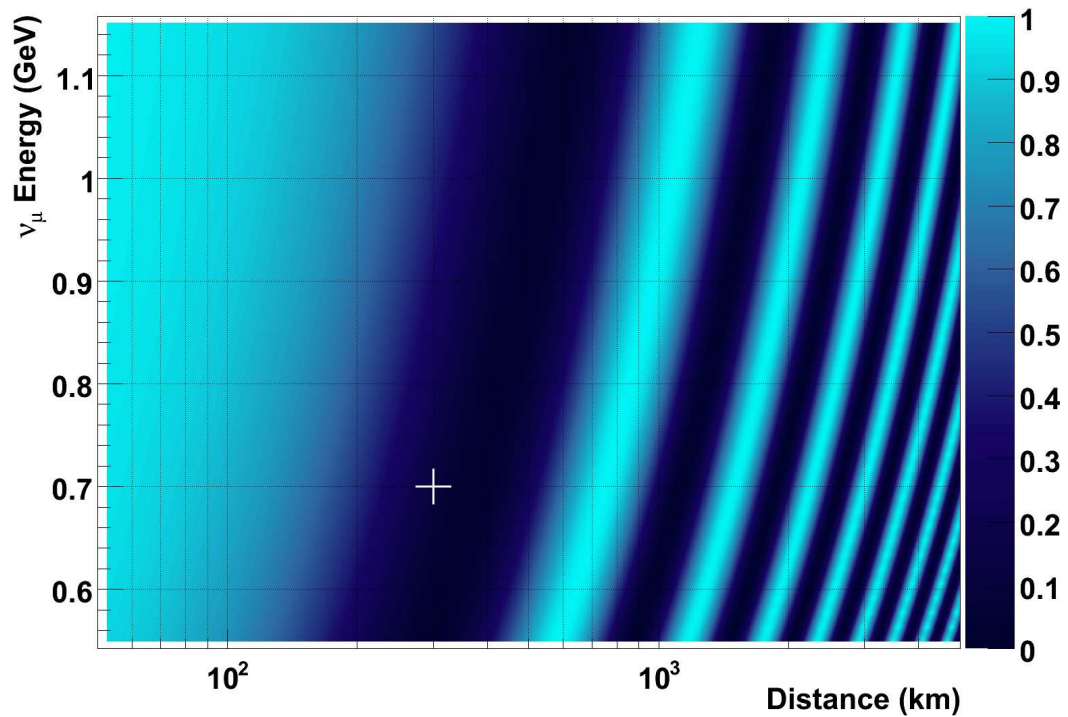


Figure 3.1: Muon neutrino survival probability as a function of baseline length and neutrino energy. The T2K beamline uses a 0.7 GeV muon neutrino beam, with a baseline of 295 km placing it at a survival probability minima.

netised high granularity detector in which the majority of the active volume is constructed using plastic scintillator bars. ND280 will use new photo sensor technology in the form of high-gain pixelated photon counting devices and will instrument over 40,000 optical channels within a magnetic field. It will contain regions of water target in order to study neutrino interaction cross sections on water to provide background extrapolation in Super Kamiokande. The detector will also allow the measurement of the intrinsic electron neutrino background in the beam.

3.1 Beamline

The T2K beam is generated at the JPARC facility at Tokai on the east coast of Japan built for the purpose of research in the field of material and life sciences, nuclear and particle physics. The accelerator consists of 3 stages. At the first stage ionised hydrogen

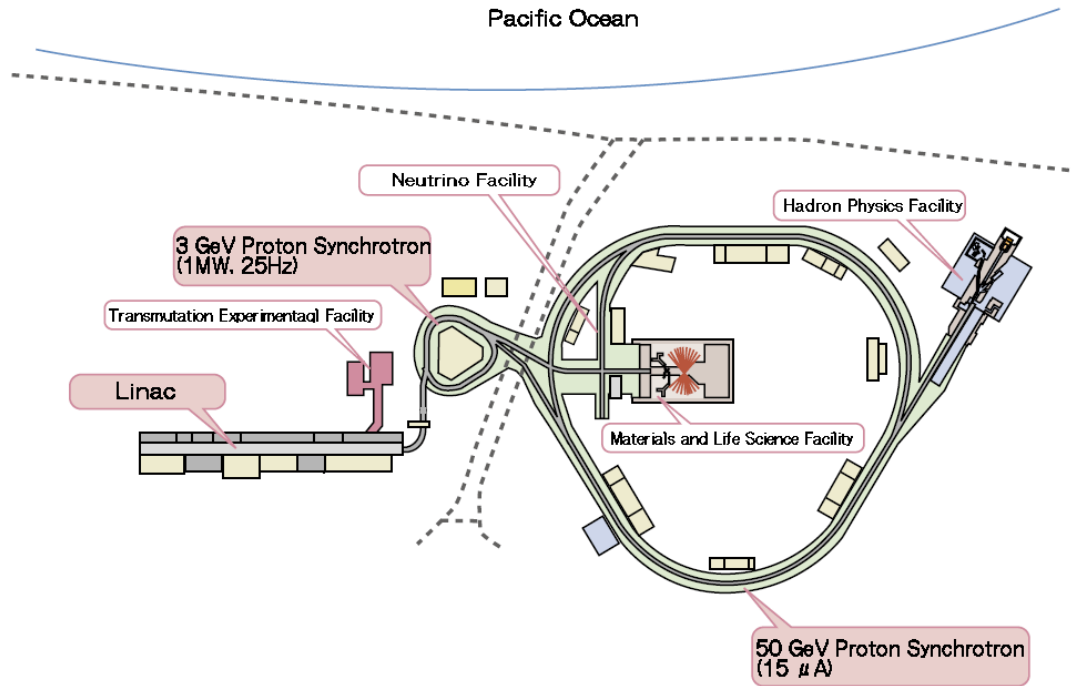


Figure 3.2: High intensity proton beam at the JPARC facility in Tokai, Japan. [41]

is injected into a 330 m linear accelerator (Linac) at a rate of 50 Hz. The protons leave the Linac with an energy of 400 MeV and are transported to the second stage. The second stage is a Rapid-cycling Synchrotron (RCS) with a circumference of 348 m and accelerates the protons to an energy of 3 MeV. The protons are held in two bunches and have a repetition rate of 25 Hz. The 3 MeV protons are then injected into the main Proton Synchrotron (PS) ring and are finally accelerated to a total energy of 50 GeV. The PS has a circumference of 1567 m and accelerates 8 bunches at a repetition rate of 0.3 Hz. The layout and overview of the whole accelerator is shown in Figure 3.2. The PS provides a proton beam for a hadron physics facility and for a neutrino facility, the latter creates an intense neutrino beam for T2K.

The neutrino facility is shown in Figure 3.3, and consists of an interior arc to the PS that points the beam westward into the target station and toward Super Kamiokande. The target station is a helium vessel housing a graphite target and 3 magnetic focussing horns. The target is a helium cooled cylindrical graphite rod encased in a titanium housing. It has a diameter of 3 cm and is 10 cm long and is positioned at a variable depth within the

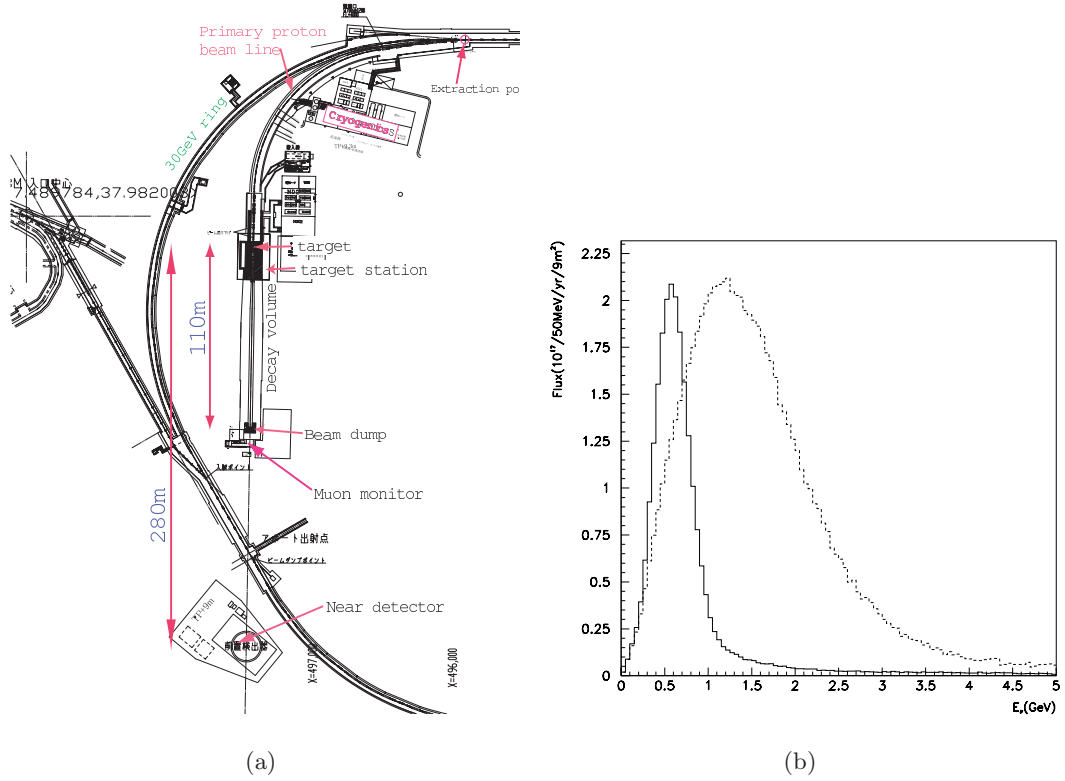


Figure 3.3: a) Neutrino beamline section of the PS. Bunches are extracted and directed toward the target station. Located 280m downstream of the target is the near detector station, b) The expected neutrino energy spectrum of the T2K beam, hashed histogram shows the on-axis energy spectrum and the solid shows the spectrum as observed 2.5° off-axis, modified from [1].

first focussing horn.

The interaction of the proton beam with the target will produce a multitude of particles, mainly charged pions. The charged pions are either focussed or deflected, depending on the polarity of the horns, and then pass into a 110 m long helium filled decay volume. This allows the focused pions to decay, to produce neutrinos, while minimising the decay of muons. Pions decay via,

$$\pi^\pm \rightarrow \mu^\pm \nu_\mu (\bar{\nu}_\mu), \quad (3.1)$$

resulting in the production of a high intensity $>99\%$ $\nu_\mu (\bar{\nu}_\mu)$ beam with a small ν_e contamination due to kaon and muon decay. At the end of the decay volume there is a beam dump composed of water cooled graphite blocks. Behind the beam dump there is a muon detector (MuMon) designed to detect any high energy muons that pass through the beam

dump and into the rock. The purpose is to monitor beam conditions, alignment with the target, and the efficiency of focussing horns allowing feedback and adjustments to be made.

Beyond the MuMon at a distance of 280 m from the target station is a pit containing two detectors, ND280 and an interactive neutrino GRID system (INGRID). These detectors act as beam monitors before oscillation has occurred. The expected energy spectrum of the neutrino beam is shown in Figure 3.3. The dashed line represents the energy spectrum as observed on-axis, along the path of the beam. It is shown that the on-axis beam peaks at 1.4 GeV and has a broad range of neutrino energies. If this beam is used for the T2K beam-line it would be very difficult to precisely extrapolate and compare the beam at the origin and after oscillation due to the uncertainty of the exact neutrino energy. In order to improve the understanding and reduce possible systematics on beam parametrisation, the T2K beam-line is positioned 2.5° off-axis. Shown as a solid histogram in Figure 3.3 is the off-axis beam energy spectrum. The off-axis reduces the total neutrino flux and lowers the mean energy, however vastly it improves its energy profile, producing a highly monochromatic beam with a mean energy of 0.7 GeV.

ND280 is positioned at 2.5° off-axis while INGRID is positioned on-axis. The off-axis position of ND280 matches that of the Super Kamiokande detector located at 295 km downstream. Each detector will be discussed in turn.

3.2 The INGRID detector

INGRID is designed as a neutrino beam monitor at 280 m capable of sampling the beam profile and determining its direction. The beam direction can vary depending on the proton beam focussing on the target, its depth in the horn and the performance and alignment of the focussing horns. As the intensity and neutrino energy is heavily dependant upon the off-axis angle (1mrad uncertainty on the centre produces a 2% uncertainty in the beam energy [42]), determining the beam centre is key to reducing systematics when extrapolating the beam to Super Kamiokande.

INGRID consists of 16 cube shaped modules, of which 14 are arranged in a central cross (7 horizontal and 7 vertical) with 2 positioned along the diagonals as shown in Figure 3.4.

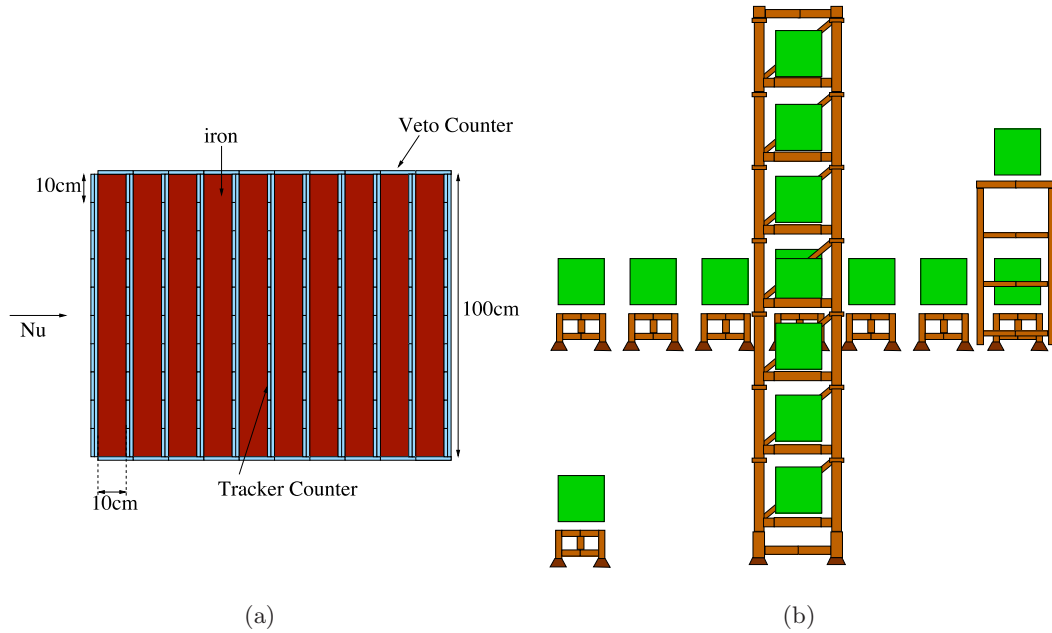


Figure 3.4: (a) design of a single INGRID module, constructed from plastic scintillator and iron, (b) Layout of the moduels to form the INGRID detector, modified from [1].

Each module consists of x-y crossed layers of scintillator bars of dimension $100 \times 5 \times 1.3$ cm read out using wavelength shifting fibre, interleaved with 10 cm thick iron plates. On the top and bottom of each module is a layer of scintillator acting as a cosmic muon veto.

3.3 The 280m near detector

As ND280 is used for beam characterisation, producing a high number of interactions with beam neutrinos is high priority. Thus design of the detector aims to provide high target mass while maximising the volume of active material for readout. It is composed of 5 subdetectors, 4 of which are positioned within a 0.2 T magnetic field. The magnetic field will be supplied by the UA1 magnet previously used in the NOMAD experiment, and recommissioned for T2K. The magnet Yoke is split into two halves, each half made up of 8 C-shaped sections, with the magnet coil positioned inside. The internal dimentions of the magnet are $3.5 \times 3.6 \times 7.0$ m inside which the 4 subdetectors are installed, this is known as the inner volume. Gaps inside the magnet return yoke are instrumented with plastic scintillator and form the Side Ranging Muon Detector (SMRD) which is the only subdetector installed outside the inner volume.

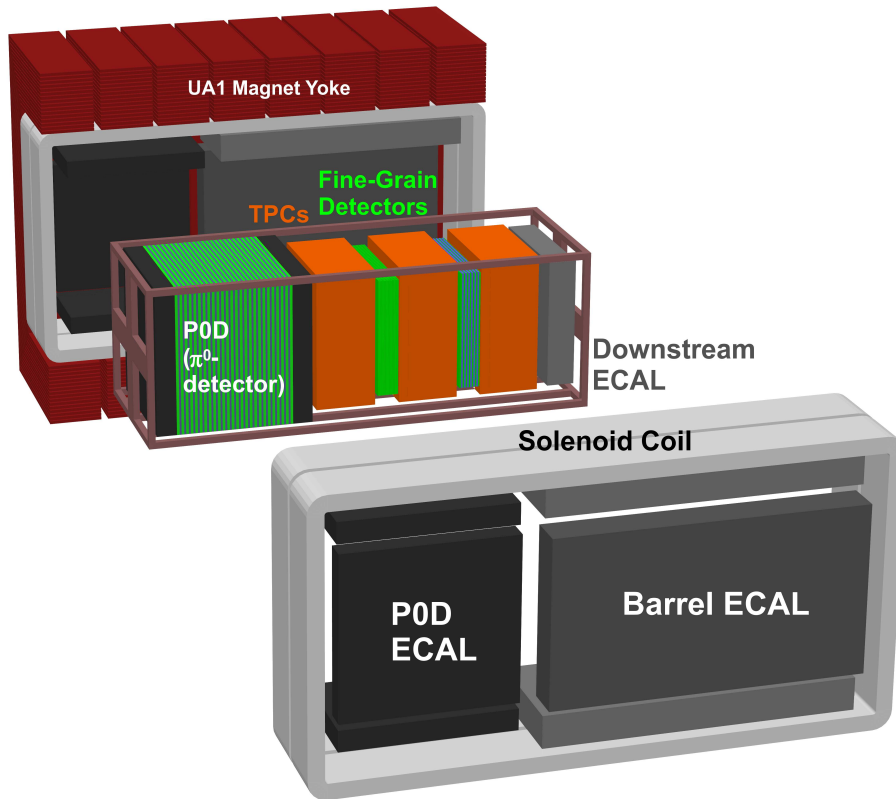


Figure 3.5: Exploded view of the ND280 detector showing each subdetector component, and the basket. The detector is orientated such that the beam moves from left to right along the axis of the basket.

Inside the magnet a 2.5 x 2.6 x 6.5 m aluminium frame (basket) is mounted and provides mechanical support for the π^0 detector (POD) and the tracker which consists of 3 time projection chambers (TPCs) and 2 fine grain detectors (FGDs). Positioned downstream of the tracker at the end of the basket there is a sampling lead scintillator calorimeter. The entire basket is surrounded by a lead sampling calorimeter mounted on the inside of the magnet coil.

A exploded cartoon of the full ND280 detector is shown in Figure 3.5, each of the subdetectors will be described in detail in the following sections.

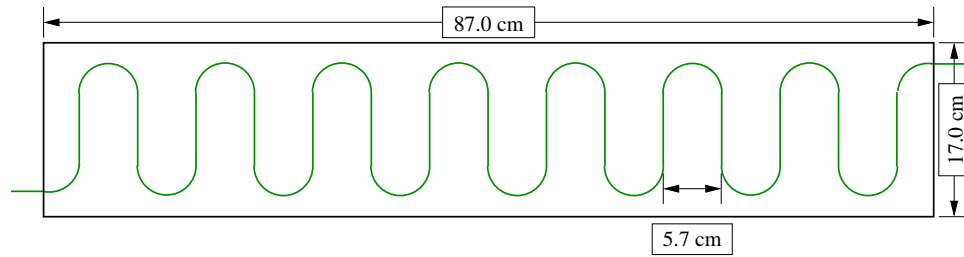


Figure 3.6: Design of the scintillator bars for the SMRD showing the S shaped path of the wavelength shifting fibre. Modified from [42]

3.3.1 Side muon ranging detector

The SMRD performs several tasks in ND280, the primary aim is to provide a measurement of momentum for muons leaving the central detectors at high angle by ranging them out through successive layers of the iron magnet yoke and scintillator. It is expected that up to 40% of muons produced in ND280 will leave the basket at high angles and would otherwise be undetected by the inner subdetectors [42], [43]. The SMRD will also be used to study backgrounds originating from the experimental pit, and to provide a cosmic ray trigger. In order to instrument the magnet, the airgaps in the yoke are instrumented with modules containing plastic scintillator, read out using wavelength shifting fibre.

The dimensions of the SMRD modules depends upon the location in the yoke. The scintillator bars used in the horizontal sections of the yoke (top and bottom) are 87 x 17 x 1 cm, and are arranged in modules of 4 bars. Vertical modules are 1 cm wider at 18 cm and are arranged in modules of 5 bars. The attenuation length within the plastic scintillator used for the SMRD is of the order of 5 cm and, as such, in order to read out a scintillator bar, an S shaped groove is etched into each bar and the fibre inset into it. The S pattern, is such that a total of 15 straight sections pass perpendicular to the axis of the bar with a separation of 5.7 cm. This design is shown in Figure 3.6.

The fibre inset in each bar is read out at both ends, in order to provide spatial resolution along the bar by examining the relative light output and arrival time. It is possible to achieve a spatial resolution of between 9.9 and 12.4 cm along the axis. Each bar has a 98% detection efficiency with a lower threshold of 5 photoelectrons applied to the readout. The top and bottom of each magnet C section will contain two modules per layer and the

sides, 4 modules per layer. The corners of each C section will not be instrumented as it would require the construction of a differently sized module for each of the 6 layers, both horizontally and vertically. In this configuration the SMRD will contain a total of 2304 optical channels.

3.3.2 Electromagnetic calorimeters

ND280 is equipped with 3 ECal subsystems, which enclose the basket detectors as shown in Figure 3.5. The 3 have separate designs, using different thicknesses of lead and readout regimes. Common to all ECal modules are the scintillating plastic bars, read out using wavelength shifting fibres, the bars have a 4 x 1 cm cross section, and are cut to the length required for each module. Each ECal module is described in detail in table 3.1 below.

System	#	Dimensions	Lead thickness	# layers	Rad Length	# Bars (x/y)
P0D						
top/bot	4	2.33 x 1.4 x 0.5 m	4 mm	6	3.6	35 / —
side	2	2.33 x 2.6 x 0.5 m	4 mm	6	3.6	58 / —
Barrel						
top/bot	4	4.2 x 1.5 x 0.5 m	1.75 mm	30	10.5	96 / 38
side	2	4.2 x 2.3 x 0.5 m	1.75 mm	30	10.5	96 / 58
Downstream						
	1	2.0 x 2.0 x 0.5 m	1.75 mm	34	11.0	50 / 50

Table 3.1: Physical parameters of each ECal module in ND280

The readout of the ECal modules depends upon the expected event multiplicity, attenuation length of the wavelength shifting fibre, and the physical size of the modules. The Downstream ECal is expected to observe a high number of events per bunch and so, the wavelength shifting fibres are readout on both sides of each bar. This provides extra information regarding the position of particles passing through the module. The Barrel ECal is part double, part single ended readout. The bars laid parallel to the long dimension of the modules are approximately 3.8 m in length and the attenuation length of the wavelength shifting fibre used to read out the bar is 3.5 m, thus in order to collect the maximum amount of light, both ends of long dimension are instrumented. The short dimension bars do not suffer as much loss via attenuation and, as such, are read out on one side only.

The purpose of the barrel and downstream calorimeters is to measure the energy of particles that exit the tracker region of the basket with a high resolution. This is of significant importance for detecting photons that leave the TPCs of the tracker and would not otherwise be detected. These modules therefore aid reconstruction of π^0 events occurring in the tracker region which would otherwise not be observed. Simulations of the Barrel and downstream ECals indicate the system will achieve an estimated energy resolution of $\sim 7.5\%/\sqrt{E(\text{GeV})}$ for energies up to 5 GeV [44].

The P0D Ecal module opts for single ended readout and parallel layers. It will use 4 mm layers and consist of just 6 layers. Due to the low number of layers and the thickness of the lead the energy resolution of this detector is poor. The main purpose of the P0D Ecal is to detect showers leaving the P0D and to distinguish between electrons and muons and provide approximate directional information.

In this configuration the whole ECal will include 22,396 optical channels.

3.3.3 π^0 detector

The P0D (π^0 detector) is located in the forward most region of the basket. Its purpose is to measure the cross section of π^0 neutral current interactions which are not very accurately determined at the T2K beam energy. π^0 production by the neutrino beam is an important measurement in determining backgrounds in Super Kamiokande as the π^0 primarily decays into 2 photons and can mimic electron neutrino like events adding systematic errors to the oscillation measurement. π^0 production proceeds via

$$\nu_\mu p \rightarrow \nu_\mu p \pi^0 \quad (3.2)$$

$$\nu_\mu n \rightarrow \nu_\mu n \pi^0 \quad (3.3)$$

$$\nu_\mu n \rightarrow \mu^- p \pi^0. \quad (3.4)$$

The P0D is constructed using triangular profile plastic scintillator bars arranged in xy crossed layers interleaved with an inactive absorber or target layer. Each bar has a 32.5 mm base dimension and are layed as shown in Figure 3.7 with 136 bars per x layer and 128 bars per y layer. Each scintillator bar is readout using a wavelength shifting fibre instrumented at one end. A single xy crossed layer and absorber is known as a P0Dule. The detector is

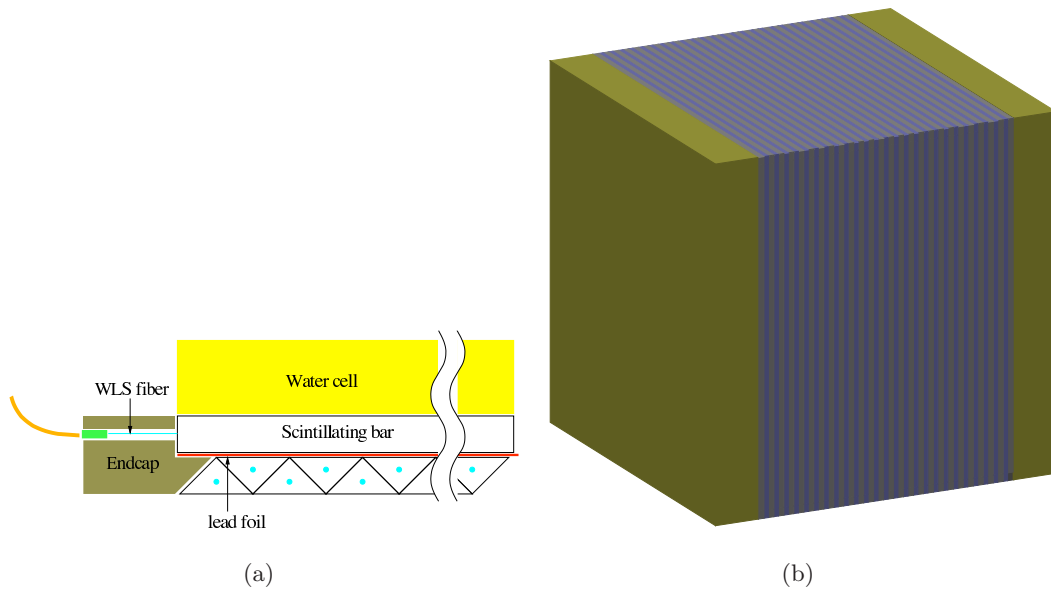


Figure 3.7: a) P0Dule layer showing the triangular profile of the scintillator bars used in the P0D, b) Layout of the P0D showing each Super-P0Dule. The central region of the detector contains a passive water target. [42].

split into 3 sections known as Super-P0Dules, each constructed of P0Dules with different composition. The forward and rear Super-P0Dules are constructed with a similar structure to the ECal detectors (Section 3.3.2); both are constructed using 7 P0Dule layers, with the forward using 4 mm thick lead absorber, and the rear 4.4 mm thick lead absorber. The middle Super-P0Dule is composed of 25 P0Dules using 1.6 mm brass absorber layers. Interleaved with each P0Dule is a 180 x 210 x 3 cm water bladder, which can be filled or unfilled depending on the detector run. Across tall P0Dules the detector will use 10560 optical channels. The total mass of the P0D is 15 t, with a total water target mass of 2 t. The layout of a P0Dule and the whole P0D detector is shown in Figure 3.7

The operation of the P0D with and without a water target allows the comparison of π^0 neutral current production on carbon, oxygen and hydrogen. The P0D will complement measurements of charge current π^0 production measurements made by the tracker to improve the accuracy in determining the ν_e contamination of the beam. The design goals for the P0D are to achieve a 30% reconstruction efficiency for π^0 and to give an electromagnetic energy resolution of $\sim 15\%/\sqrt{E(\text{GeV})}$.

3.3.4 Fine grain detectors

The tracker region of the basket contains two fine grain detectors (FGDs) constructed using $0.96 \times 0.96 \times 184.3$ cm extruded plastic scintillator bars, sandwiched between Time Projection Chambers (Section 3.3.5). Each bar is read out using a wavelength shifting fibre, instrumented at one end, and mirrored using an aluminium coating on the other. The dimensions of both FGDs is $330 \times 240 \times 36.5$ cm. Each FGD has a different internal structure, the forward most FGD (towards the π^0 detector) is constructed of 30 layers of 192 bars, in an x-y crossed structure. The rear FGD uses just 14 layers of scintillators, which form 7 xy crossed sandwiches with 2.5 cm thick layers of water contained in polycarbonate panels. Both FGDs provide a total target mass of 1 t and require a total of 8448 optical channels.

As the two FGDs contain the same target mass, although consisting different materials it allows the two detectors to determine the difference between neutrino event rates within the two target materials. By comparing the cross section on these two materials it will allow ND280 to predict the expected neutrino cross section more accurately in Super Kamiokande. The use of small scintillator bars by the FGD is to aid in the identification of low energy proton tracks which are a vital component in correctly identifying CC-QE events.

3.3.5 Time projection chambers

The tracker region of the basket contains 3 time projection chambers (TPCs) interleaved with the FGDs. Each module is $2.5 \times 2.5 \times 1$ m, and contains a inner volume filled with Ar (95%) CF_4 (3%) and C_4H_{10} (2%). It will use a 200 V/cm electric field, requiring a -25 kV potential to be applied in the chambers. The readout of ionisation tracks will be performed using MicroMegas modules [45] [46], which provide amplification without the need for thin high tension wires spread throughout the volume. Each Micromegas device contains an array of 48×36 6.8×9.7 mm pads formed on a PCB. Above the PCB is a micromesh woven from $59 \mu\text{m}$ pitch wires. Each TPC contains 24, 36×34 cm Micromegas modules. The use of MicroMegas modules will give the TPCs a spatial resolution of the order $\sim 600 \mu\text{m}$

The purpose of the TPCs are to provide high resolution momentum measurements of curved tracks. Given the 0.2 T magnetic field, some particles will have very low curvature, thus a highly segmented detector is required. The TPCs will allow the measurement of the off-axis neutrino energy spectrum by providing 3D reconstruction of tracks and accurate particle ID by separating electron and muon signals.

The TPCs are designed to have a momentum resolution of $\sigma_p/p \sim 10\%$ @ 1 GeV/c and give a 3σ separation in deposited energy of muons and electrons in the 0.3—1 GeV/c momentum range.

3.3.6 ND280 Scintillators

As described above, with the exception of the the TPC all subdetectors of ND280 instrumented with plastic scintillator read out using wavelength shifting fibre. Scintillator bars are produced with dimensions according to the specification of the destined sub-detector. The plastic scintillator is composed of polystyrene doped with 1% PPO (2,5-diphenyloxazole) and 0.03% POPOP (1,4-Bis-[2-(5-phenyloxazolyl)]-benzene). The bars are produce by melting pellets of polystyrene with pre-mixed PPO (primary) and POPOP (secondary) fluors, and forcing the melt through a die. A layer of polystyrene doped with TiO_2 is applied to the surface of the bar before the mixture leaves the die. The bar is then cooled using a water bath and then cut to a desired length. As the process of extrusion is continuous, the saw moves with the bar such that the plastic remains in continuous flow. The final outcome is cut lengths of plastic scintillator with a hole passing through the middle with a diameter of typically 2.0 ± 0.2 mm.

When a high energy particle passes through the scintillator, it loses energy by ionisation of the scintillator. This causes excitation of loosely bound π orbital electrons of the primary scintillator into a higher energy state. This process is shown in Figure 3.8 as blue lines. The excited electrons will decay nonradiatively back to the S^* state very rapidly (internal degradation), this is denoted by the dashed red lines. The S^* will decay to vibrational states of S_0 typically with a timescale of nanoseconds via the emission of photons (flouresence), this is denoted by the solid red line. As the photons are emitted with an energy less than that of the excited S^* , the photons can pass through the material without being reabsorbed. Excited triplet states undergo similar processes as the singlet

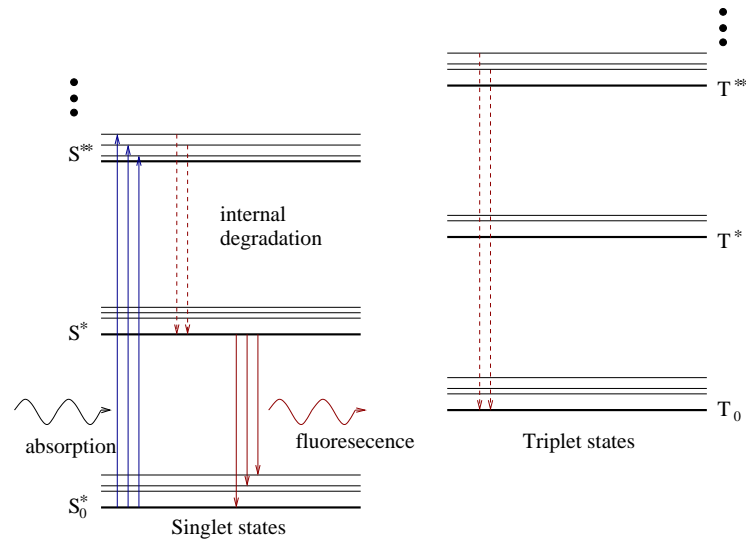


Figure 3.8: Energy level diagram showing the scintillation process in organic materials [47]

however, the emission of photons occurs from the interaction of the triplet states of two molecules to produce an excited S^* state which then undergoes radiative decay. This process is subdominant and produces delayed photons from the material [47].

In ND280 the primary scintillation light is produced with a peak wavelength of 365 nm. The secondary scintillators purpose is to absorb the photons produced by the primary and re-emit photons at a longer wavelength, shifting the emission peak of the scintillator to 420 nm. Scintillation photons are read out from the bar by a wavelength shifting fibre positioned in the central hole of the bar. Photons must escape the bulk plastic and into the air gap, and then be absorbed by the fibre.

3.3.7 Wavelength shifting fibres

The wavelength shifting fibre used throughout ND280 is a Kuraray Y11 (200) S-35 fibre. They are double clad fibres, made from a doped inner polystyrene core with a polymethyl methacrylate inner and fluorinated polymer outer cladding. The double cladding of the fibre aids total internal reflection allowing it to transmit photons produced inside at an angle less than 26.7° . The fibre has a diameter of 1 mm (t_c), with each cladding layer using 0.03 mm of this diameter (t_i , t_o). Figure 3.9 shows the schematic of the selected fibre, giving the refractive indices of each region of the fibre.

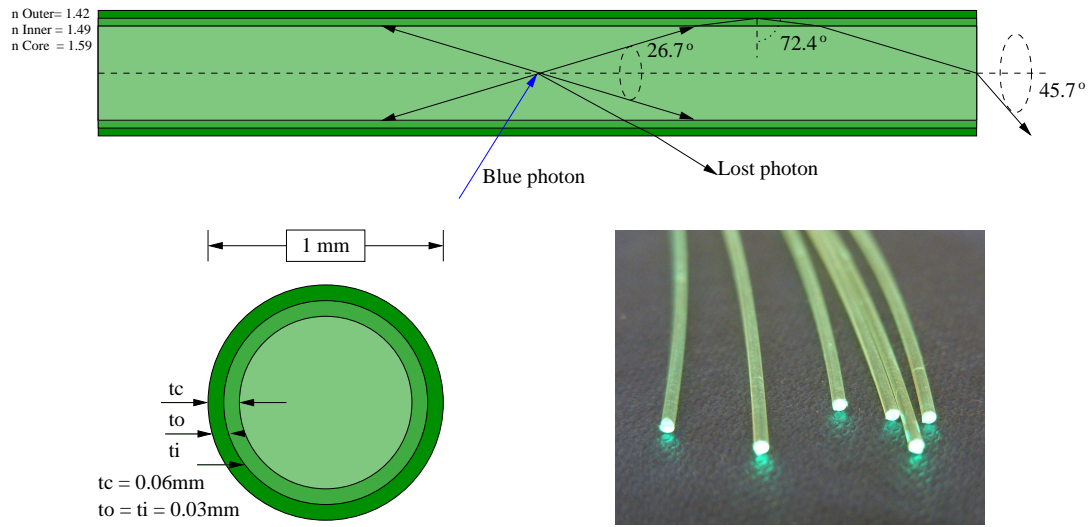


Figure 3.9: Schematic of Kuraray Y11 fibre selected for ND280, redrawn from [48].

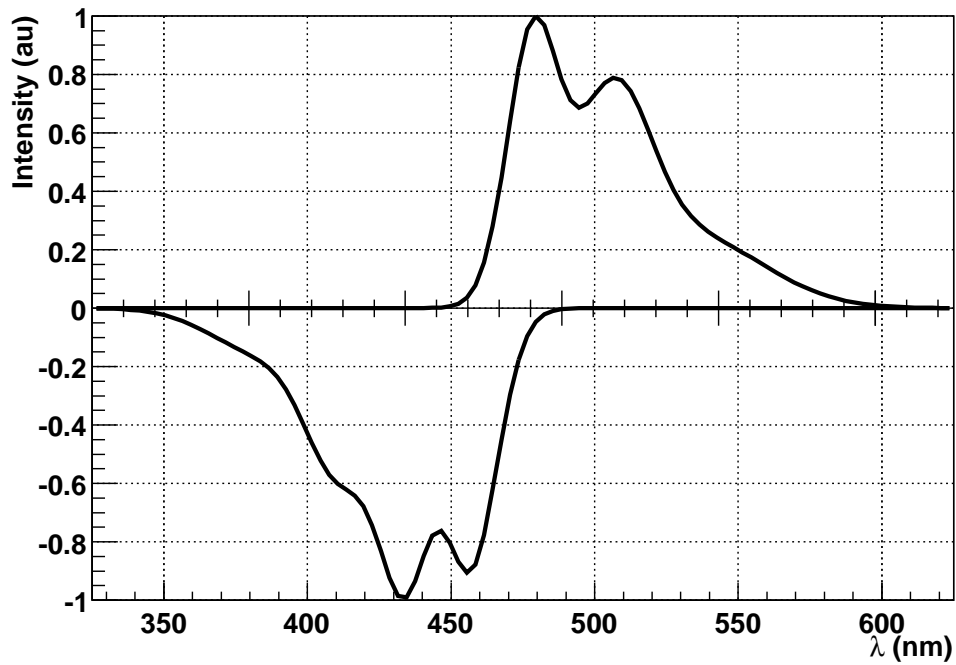


Figure 3.10: Absorption and emission spectrum of Kuraray Y11 fibre, redrawn from [48].

The fibre has an absorption peak at 430 nm, at which it absorbs photons and, due to the fluors introduced into the fibre, it re-emits photons at a longer wavelength peaking at 476 nm shown in Figure 3.10, with a decay time of 7 ns. The fibre has an attenuation length of 350 cm, along this length the emission spectrum shown shifts to longer wavelengths, peaking at 515 nm due to self absorption in the region of 450 to 490 nm. As photons can be absorbed at any point in the fibre, and re-emitted isotropically, photons will emerge from both sides of the fibre rather than only one. The efficiency at which any absorbed photon is re-emitted such that it will undergo total internal reflection and ultimately reach the end of the fibre (trapping efficiency) is approximately 5%. Read out of these photons is performed using a pixellated semiconductor photosensor, typically referred to as a silicon photomultiplier.

3.4 Super Kamiokande

At 295 km downstream from JPARC is the T2K far detector; Super Kamiokande. The purpose of this detector is to parametrise the beam after oscillation, by accurately measuring the ν_e and ν_μ components of the T2K beam. Prior to the operation of T2K the primary purpose of Super Kamiokande was to study solar and atmospheric neutrinos. The detector is an upgrade to its predecessor Kamiokande, it began operation in 1996.

The main structure of the Super Kamiokande detector is a 39.3 m diameter, 41.4 m high steel cylinder filled with approximately 50,000 t of pure water, constructed underground at a depth of 1 km (~ 2700 m water equivalent depth) in the Kamioka mine in Japan. It is separated into two detection volumes, such that the main inner volume is a 33.8 m diameter 36.2 m height cylinder at the centre of outer steel structure. The two detectors are separated by support structure holding 11,000 50 cm PMT pointed inwards for the inner detector and 1,800 20 cm PMTs pointed outwards that compose the outer detector. To provide an optical barrier between the inner and outer regions, black polyethylene sheets cover the walls of the inner detector, and highly reflective white Tyvek [49] sheets cover the walls of the outer detector. The total photon acceptance of the inner detector is 40.41%. In order to provide greater acceptance in the comparatively sparsely populated outer detector, each PMT is connected to a 60 x 60 cm wavelength shifting plate mounted at the widest point of the photocathode bulb [50], [21]. The design of Super Kamiokande

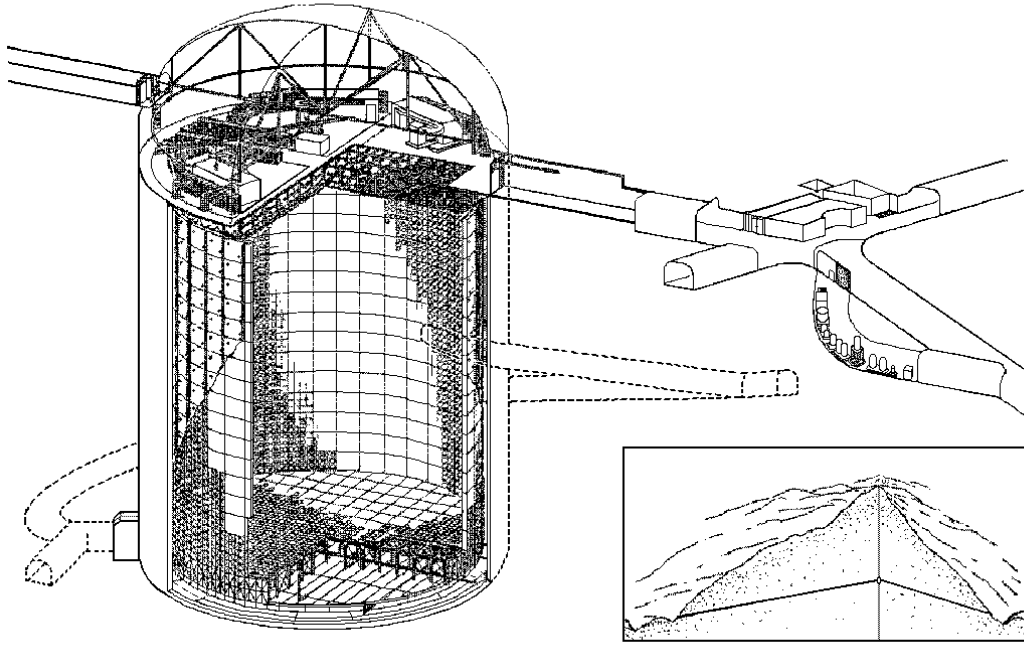


Figure 3.11: Schematic of the Super Kamiokande detector

is shown in Figure 3.11

The detector operates on the principle that charged particles moving at greater than the speed of light in water produce Čerenkov radiation emitted in a cone along the momentum vector of the particle. The opening angle of the cone depends upon the particles' velocity by,

$$\cos \theta = \frac{c}{vn(\lambda)} = \frac{1}{n\beta}, \quad (3.5)$$

where c is the speed of light in vacuum, v is the velocity of the particle and n is the refractive index of the medium. As the particle moves through the medium it loses energy in the form of Čerenkov radiation until its velocity falls below the speed of light in the medium (water), this produces characteristic rings of photons at the detector walls of Super Kamiokande. If a particle does not stop within the water volume of the detector, a filled circle of photons is observed. The distribution of Čerenkov photons produced in the detector is passed through pattern recognition software which identifies Čerenkov rings as 'electron like' or 'muon like' depending upon its sharpness. Figure 3.12 show event displays for typical 'electron like' or 'muon like' ring events in Super Kamiokande.

The difference in sharpness is due to how the two leptons traverse through water. A high

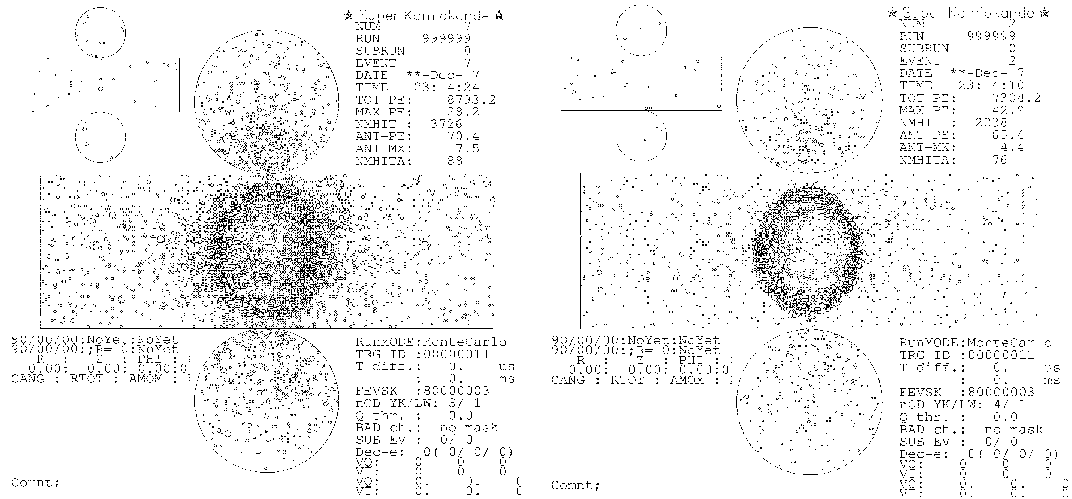


Figure 3.12: Left shows a typical ‘electron like’ ring event and right shows a ‘muon like’ ring event. Each square shows the total charge output of a hit PMT [51].

energy electron will initiate a collated electromagnetic shower, producing photons and multiple electrons. Each secondary particle will in turn produce Čerenkov radiation if its energy is above the Čerenkov threshold (see table 3.2). The final result of the shower is the production of multiple overlapping rings, which appear in Super Kamiokande as a single smeared ring. Muons do not suffer from such effects as they pass through the water and so emit a cone of light along a single track. The resultant ring is therefore observed to be significantly sharper than that of an electron. The identification efficiency achieved using pattern recognition separates the two types of rings with an accuracy of over 95% [52].

The energy of a particle can be reconstructed in Super Kamiokande as the total number of Čerenkov photons is proportional to the tracklength of the particle. The number of photons emitted per unit path length per unit wavelength is described by the Tamm-Frank formula [53] as,

$$\frac{d^2N}{dx d\lambda} = \frac{2\pi\alpha}{\lambda^2} \left(1 - \frac{1}{n^2\beta^2}\right), \tag{3.6}$$

where α is the fine structure constant, x is the path length of the charged particle, and λ is the wavelength of the emitted photon. This equates to approximately 340 photons/cm in water for Super Kamiokande. [54]. The energy threshold for particles producing Čerenkov radiation is summarised in Table 3.2.

In T2K, the time of arrival of the neutrino beam at Super Kamiokande will be known, and

Particle	Čerenkov energy threshold (MeV)
e^\pm	0.768
μ^\pm	158.7
π^\pm	209.7

Table 3.2: Čerenkov energy threshold for electrons, muons and pions in water [55]

due to the momentum of each neutrino, any interactions will be collimated along the beam axis, aiding identification of neutrino beam events. For each event, each photomultiplier tube will be readout along with the relative hit times of each. Timing information and the hit pattern can then be used to reconstruct the location of the interaction vertex. Beam neutrinos interact primarily by two methods in Super Kamiokande; mainly by charge current interactions resulting in the production of the lepton partner of the neutrino and a recoil nucleon as follows,

$$\bar{\nu}p \rightarrow l^+n, \quad (3.7)$$

$$\bar{\nu}n \rightarrow l^-p. \quad (3.8)$$

The second method is due neutrino electron scattering, which occurs for all neutrino flavours. For scattering events the interaction cross section of electron neutrinos is the most dominant of the three flavours.

3.4.1 Backgrounds

A small but not insignificant background to the identification of neutrino flavour at Super Kamiokande is neutral pion production by muon neutrinos as shown in Section 3.3.3

The primary decay channel of neutral pions is via the production of two photons. Due to the relativistic nature of the neutrino beam the two photons will be produced along the beam axis, resulting in two electromagnetic showers. At low energies the pion can be identified by the observed double Čerenkov rings, however at higher energies a single electron like ring is observed and is misidentified as an electron neutrino interaction. This produces systematic uncertainties on the muon neutrino disappearance measurement. This underlines the role played by the ND280 detector in the extrapolation of the beam content to Super Kamiokande and the determination of the expected pion production along the

beam.

Chapter 4

Photosensors

The first semiconducting devices were developed in the 1930's, and in the subsequent decades manufacturing techniques were developed and refined allowing the construction of more and more complex semiconducting detectors and devices. The first viable semiconducting nuclear detector was developed in 1943 [56]. It was constructed from a AgCl crystal and required cooling in liquid nitrogen, but was able to produce observable electrical signals from incident radiation. Advances in construction techniques resulted in the production of the transistor in the late 1940's and has since progressed into millions of different electronic devices used by everyone during daily life. Nuclear and high energy physics have greatly benefitted with the development of semiconducting ionisation detectors, that provide high resolution energy and position measurement of charged particles. Today, semiconductor detectors are common place in High Energy physics, and are often used as high resolution vertex detectors and photosensors.

In this section the basic principles of a semiconducting photosensor will be discussed as background for a more detailed discussion of a new novel type of photosensor. This type of photosensor has been in development since the late 1990's, with the first prototype devices becoming available early in the current decade. There are many acronyms for this type of device depending on the manufacturer and often personal preference of the user. Throughout this thesis the term Geiger-mode Avalanche Multi-Pixel Photo-Diode (GAMPD) will be used as it more accurately describes structure and properties of the device. Common acronyms include Silicon Photo-Multiplier (SiPM), Multi-Pixel Photon

Counter (MPPC), Metal-Resistive Silicon Avalanche Photo-Diode (MRS-APD).

4.1 Semiconducting materials

The electrons of an atom occupy discrete energy states or levels, and for all atoms but Nobel gases, the outermost levels have free states into which an electron can be accepted. When in close proximity to other atoms, such as a crystal, the upper energy levels of neighbouring atoms overlap allowing the formation of bonds by sharing or exchanging outer electrons. Such electrons are known as valence electrons. Under these conditions the energy levels form a band structure consisting of two distinct energy regions; a lower energy region known as the valence band and a higher region known as a conduction band. Electrons of the valence band are tightly bound to the parent atom, however, conduction band electrons are only loosely bound and thus are able to move within the body of the material.

From this basic description of the outermost energy levels of the atoms of a material, it is now possible to describe the band structure of metals and insulators. A metal is a material in which the valence and conduction bands overlap allow outer electrons free movement throughout the material. An insulator is a material in which there is a large energy gap between the valence and conduction bands and such electrons remain tightly bound to their parent atom. Semiconducting materials are an intermediate between these two distinct configurations. The energy gap is small (approximately 1 eV), resulting in electrons being promoted to the conduction band by thermal excitation. This allows a small current to flow through the material when an electric field is applied [47], [57].

4.2 Charge carriers and doping

The charge carriers of a semiconductor are also different to that of a metallic material. In a metallic material the charge carriers are the electrons present in the conduction band. In contrast a semiconductor has two charge carriers, electrons and ‘holes’. When an electron is promoted to the conduction band, it leaves behind an empty state or hole. This state has a positive charge relative to the electron. The movement of the hole state is achieved

by a neighbouring valence electron filling the state, leaving a hole state in its original location. As the hole occupies an energy state within the valence band, this process occurs spontaneously allowing the positively charged hole to move through the crystal and act as a charge carrier.

The properties of a semiconductor can be modified by the introduction of impurity atoms. Silicon has 4 outer electrons and forms covalent bonds with four neighbours in order to fill free valence states. If an impurity atom is added to the crystal lattice with 5 valence electrons, the surrounding silicon atoms form bonds with the 4 valence electrons leaving 1 unbound electron. An impurity atom that adds extra electrons to the crystal is known as a donor. The electron energy levels of the donor atom are different to that of the surrounding silicon and introduce 'donor states'. The energy level of a donor state is typically close to the conduction band of the semiconductor and thus the donated electron is very loosely bound to the parent atom. A doped semiconductor with an excess of electrons is called an n-type semiconductor.

A semiconductor doped with an impurity with 3 valence electrons forms covalent bonds as described with the exception that the impurity introduces a local electron deficiency within the crystal. Similar to a donor, the impurity has energy levels close to the valence band. An impurity that introduces an empty electron state to the crystal is called an acceptor. As such the material will have fewer free electrons than a pure crystal, the majority charge carrier being the empty hole states introduced by impurity atoms. A doped semiconductor with an excess of holes is called p-type semiconductor.

Typical semiconducting materials are group IV elements such as silicon and germanium. With dopants from groups either side on the periodic table; acceptors from group III such as boron and gallium, and donors from group V such as phosphorus and arsenic.

4.3 The p-n junction

When an n and p type semiconductor are joined, the interface between the two differently doped regions forms the building block of a basic semiconductor device. The two regions have very different electron and hole concentrations, this results in the diffusion of electrons into the p region and likewise holes into the n region. The carriers that diffuse are captured

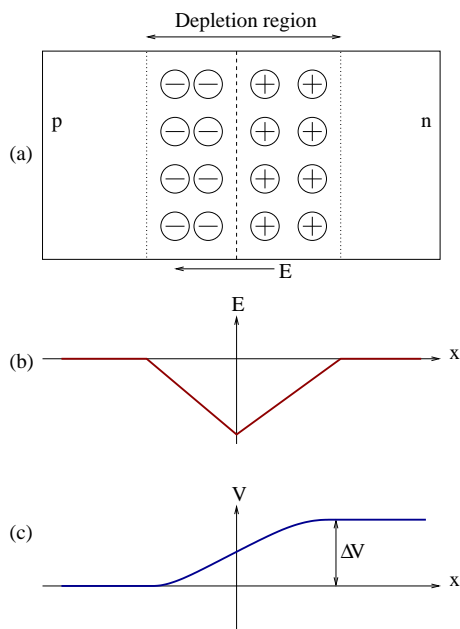


Figure 4.1: (a) Schematic of a p-n junction showing the ions of the depletion region, (b) Electric field strength across the depletion region, (c) Potential difference across the depletion region caused by the charged ions.

by the available electrons or holes and produce a region surrounding the interface that contains no charge carriers, this is known as the depletion region. The depletion region will be positively charged on the n side and negatively charged on the p side producing an electric field across the interface. Due to the electric field across the depletion region, a potential barrier across the interface is also formed ensuring zero current flow across the junction. The final state of this initial diffusion, and a plot of electric field strength and potential across the junction is shown in figure 4.1. The energy band structure of a typical p-n junction is shown in figure 4.2. The figure shows the direction in which the charge carriers generated in the depletion or doped regions are swept through by the electric field.

4.4 Applying bias to the junction

If a positive electric field is applied to the p side of a p-n junction, the applied field opposes the initial electric field direction as introduced previously. This will result in the reduction of the potential barrier across the junction and with it the width of the depletion region. The effect of this is an increase in carrier diffusion across the junction, thus cause a rapid

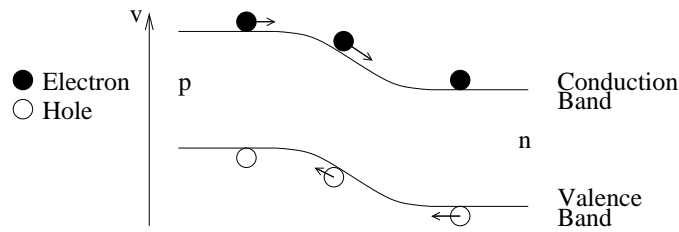


Figure 4.2: Energy band structure across a p-n junction showing electron and hole drift directions.

increase of current flow. Such biasing regimes are known as forward bias.

Alternately, if a positive electric field is applied to the n side of the p-n junction, the applied field is in the same direction as the initial electric field. This will in turn increase the electric field across the junction, which increases the potential barrier, widening the depletion region. This biasing regime is known as reverse bias. Under reverse bias a small current will flow through the diode. This current is the result of the generation of carriers near to p-n junction which are swept through the depletion region, thus as reverse bias is applied the current flow increases quickly and saturates at a low level. Under reverse bias however, application of a sufficiently high electric field to the junction will cause it to break down and a large current to flow. The behaviour of the p-n junction was first modelled by and developed between 1949 and 1958 [58].

4.4.1 Breakdown

Breakdown of the junction occurs in two modes, avalanche breakdown and Zener breakdown. Only avalanche breakdown will be discussed here as it is of more importance when describing an avalanche photo-diode. Avalanche breakdown occurs when the electric field across the p-n junction is large enough to accelerate a carrier through the depletion region with giving it sufficient energy to cause impact ionisation in the lattice. The electron and hole pair produced in this manner are in turn accelerated and repeat this process. Under this regime the current flow increases rapidly. The value of breakdown voltage is dependant upon the energy gap of the semiconductor, the doping levels of the semiconductor and the temperature.

The features of a typical Current - Voltage plot for a p-n junction are shown in figure 4.3.

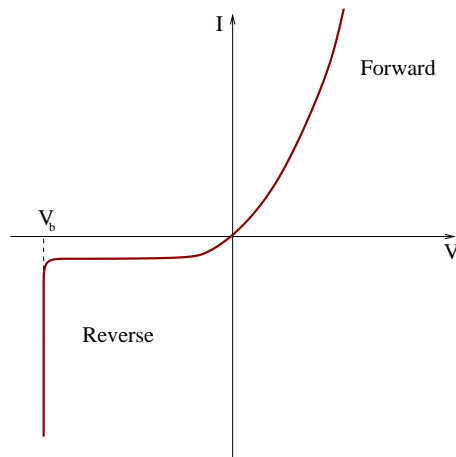


Figure 4.3: Current as a function of bias applied across a p-n junction. V_b is the breakdown voltage of the device

A mathematical treatment of the p-n junction is important to understand how it responds to the application of external bias and can be found in references [57], [59].

4.4.2 Temperature dependence

The value of the breakdown voltage increases with temperature, the rate of increase depending heavily on the doping concentration of the semiconductor. Increasing temperature results in an increase of lattice vibrations which, in turn, causes a decrease in the mean free path of carriers throughout the lattice. Thus, if the mean free path decreases, a carrier must pass through a larger electric field in order to have the energy to produce an electron-hole pair via impact ionisation. In order to produce a higher electric field across the junction, the voltage applied must therefore increase in order to result in breakdown [60].

4.5 Detecting light

The absorption of photons by a semiconductor is identical to absorption of photons in a gas. An electron will absorb a photon of a specific energy allowing it to be promoted to a higher energy level. In a semiconductor only the band-gap between the valance and the conduction band is applicable. Thus the semiconductor will absorb photon wavelengths

with energies greater than the band-gap and produce an electron-hole pair. For silicon the band-gap is 1.1 eV corresponding to a wavelength of 1130 nm. In practise there is an upper limit on the photon wavelength, caused by the photo-absorption coefficient of the semiconductor that is strongly dependant on wavelength. In order to produce current the photon must be absorbed near the depletion region such that a carrier can be swept through the depletion region and read out. Thus the depth of the junction and the orientation in which it is illuminated plays an important role in wavelength sensitivity. This behaviour of a reverse bias p-n junction was first modelled in 1957 [61].

Figure 4.4 shows the fraction of absorbed photons as a function of depth. It follows that to manufacture a blue sensitive photo-detector or photo-diode the p-n junction must be close to the surface of the device. While the opposite is true for red sensitive photo-diodes. The structure used for red and blue sensitive Avalanche Photo-Diodes (APD) is shown in Figure 4.5. In the ‘p on n’ structure photons absorbed close to the p-n junction in the absorption region produce an electron-hole pair, by considering the band diagram in Figure 4.2, electrons will drift toward the depletion (avalanche) region. In ‘n on p’ structure, the absorption region is deeper inside the silicon. In this structure the holes of the photon produced electron-hole pair are drifted towards the avalanche region. These differences affect the response and timing resolution of the photo-diode since the ionisation rate of electrons is higher than holes, therefore an ‘p on n’ device responds more quickly and has higher timing resolution [57].

4.6 Geiger-mode amplification and quenching

The gain of a photo-diode is strongly dependent on the applied reverse bias. At low bias a photo-diode has a typical gain of order 10. At high reverse bias the number of carriers are amplified by impact ionisation in an avalanche as discussed in section 4.4. In this process, electrons are the primary cause of impact ionisation and typically allows the generation of 100-1000 times more carriers. If the dominating source of gain is produced by avalanche multiplication, the device is known as an Avalanche Photo-Diode (APD). It is possible to design a device that operates above the breakdown voltage of the p-n junction. Biasing the device in such a way causes Geiger or limited Geiger mode operation. In this regime the electric field across the depletion region is high enough that both electron and holes

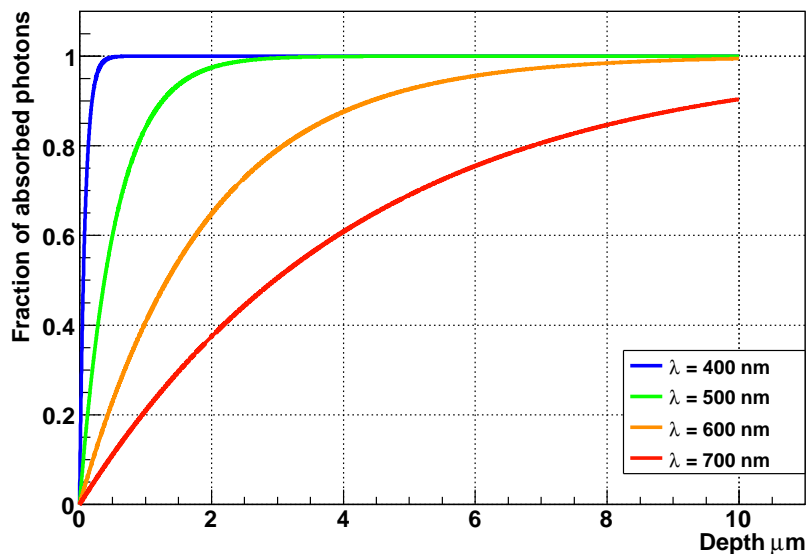


Figure 4.4: Fraction of photons absorbed as a function of depth in silicon ($1 - e^{-\alpha x}$). Absorption coefficient α obtained from [62] for the shown wavelengths.

cause impact ionisation. It follows that both electrons and holes will cause secondary impact ionisation of the lattice, exponentially increasing the number of charge carriers. The p-n junction quickly saturates with carriers causing a very large current to flow. Due to current heating of the junction, breakdown of the junction in this manner can damage or destroy the device, thus it is typical to operate a Geiger-mode APD in series with a resistor in order to quench the avalanche by dropping the bias voltage below breakdown

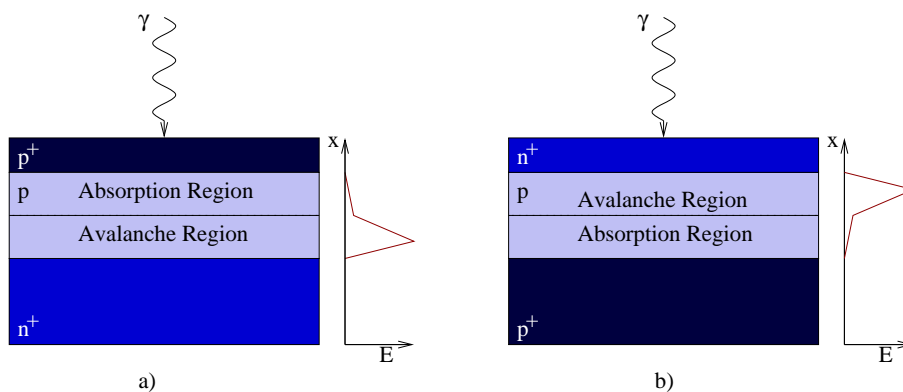


Figure 4.5: Typical doping structure of avalanche photo-diodes showing absorption and avalanche regions. a) 'p on n' structure. b) 'n on p' structure

when a discharge occurs. When a APD undergoes Geiger discharge, the charge output from the device is as follows,

$$Q = C(V_b - V_{bd}) \quad (4.1)$$

where C is the capacitance of the p-n junction, V_b is the applied bias voltage and V_{bd} is the breakdown voltage. The form of this equation indicates that the gain of an APD in Geiger-mode holds no information regarding the trigger method. An APD undergoing a Geiger discharge produces the same charge regardless of whether 1 photon or more photons are detected. In this case increasing the gain allows the production of large signal pulses that do not require complex readout electronics, instead a simple amplifier may be used to adequately provide detectable pulses.

Chapter 5

Geiger-mode avalanche multi-pixel photo-diodes

Based on the information presented in the previous chapter it is now possible to describe the GAMPD photosensor.

5.1 Schematic design

The GAMPD is an array of identical APDs (micro-cell or pixel) constructed on a common substrate, connected by a common readout chain. Two methods of applying reverse bias to the GAMPD are displayed in Figure 5.1. In order to achieve Geiger mode operation, the voltage applied to the chain is above the breakdown voltage of the component pixel. An equivalent circuit of the GAMPD is also given, in which each pixel is connected in series with a quenching resistor. Despite the use of common readout, the use of a quenching resistor for each pixel means that each pixel is independent from neighbouring pixels and can undergo discharge and reset without adversely effecting the whole device. The basic topological design of each pixel is similar to that shown in Figure 4.5, however includes an extra structure in order to isolate each pixel, provide efficient carrier collection and provide bias to each pixel. Example designs are presented in other studies of GAMPD properties, [63] [64] and a manufacturer's catalogue [65]. Each design shows similarities, but differ in how each pixel is separated. The most common method of separating pixels is

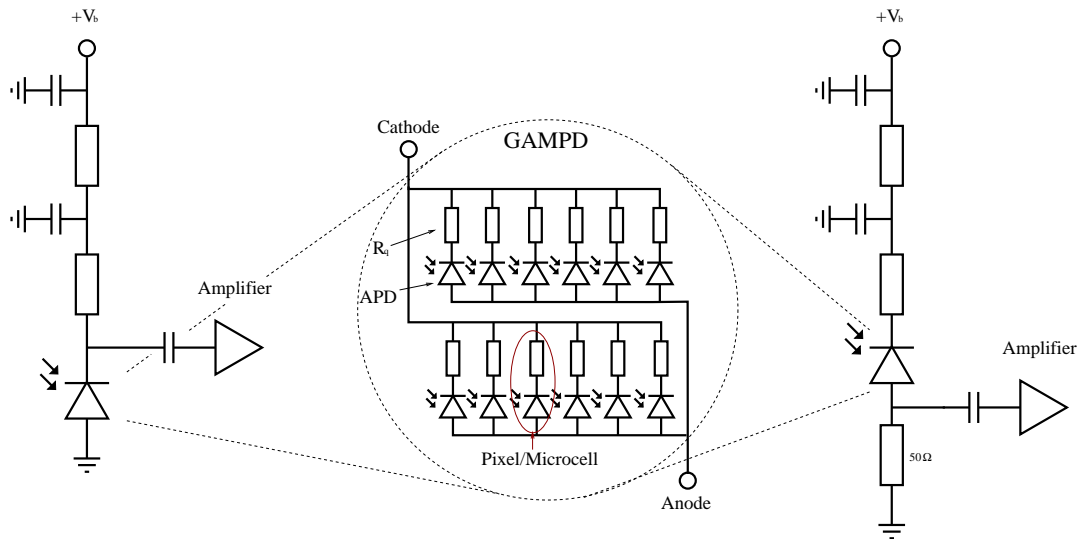


Figure 5.1: Typical bias chains used with a GAMPD and an equivalent circuit showing the placement of quenching resistors (R_q) connected to each APD. For both chains a positive voltage is applied.

to use a guard ring of highly doped material or a physical trench etched into the substrate. On the surface of the pixel a thin passive layer of lightly doped high resistivity material is often deposited in order to give the manufacturer accurate control over the absolute value of the breakdown voltage. The shape of each pixel and the arrangement on the substrate is highly customisable and varies between manufacturer. It is possible to make the pixels any desired shape, although in order to achieve closer packing approximately square pixels are the most common solution. This is also true for the whole array, most manufacturers deciding to produce devices with square or rectangular arrays. The final design of a GAMPD is a carefully selected combination of several key parameters in order to achieve high gain, dynamic range and photo-detection efficiency (PDE) while maintaining low dark count rate, crosstalk and afterpulsing. Each listed physical property of a GAMPD will be discussed in terms of key parameters.

5.2 Gain

The gain of a GAMPD is determined by the capacitance of the component APD. The total capacitance of an APD is defined by the width of the depletion region and area of

the p-n junction. A mathematical treatment of the capacitance of a p-n junction [57] is given by:

$$\begin{aligned} C(F/cm^2) &= \frac{\epsilon_s}{W} \\ &= \frac{\epsilon_s}{\sqrt{2}L_D} (\beta V_{bi} \pm \beta V - 2)^{-1/2}, \end{aligned} \quad (5.1)$$

where ϵ_s is the permittivity, W is the width of the depletion region, V_{bi} is the initial potential under zero bias and V is the bias voltage applied to the junction. L_D is the Debye length given by:

$$L_D = \sqrt{\frac{\epsilon_s}{qN_B\beta}}, \quad (5.2)$$

where N_B is the doping concentration, q the electron charge and β given by,

$$\beta = \frac{q}{kT}. \quad (5.3)$$

The appearance of \pm in equation 5.1 is for the case of reverse and forward bias of the junction respectively. Thus under reverse bias the capacitance of the junction will decrease as the depletion region becomes wider. However due to the $1/\sqrt{V}$ relationship, at the breakdown voltage of the junction, the capacitance of the junction will be approximately constant. It follows that for an APD using the same p-n junction structure the total capacitance is set by the physical area of the APD.

The capacitance and the gain of the APD operating in Geiger mode are related by the following,

$$\begin{aligned} Q &= C(V_b - V_{bd}) \\ G &= \frac{C}{q}(V_b - V_{bd}) \end{aligned} \quad (5.4)$$

Where C is the capacitance of the APD, V_b is the applied bias, and V_{bd} is the breakdown voltage. The quantity $V_b - V_{bd}$ is a parameter known as ‘over-voltage’. The above equations assume the gain is linear with over-voltage, as the pixel capacitance is not expected to change with over-voltage. Another feature of this equation is that gain is defined to be exactly zero at the breakdown voltage. While this statement is overly simplified and does not take into account the occurrence of avalanche amplification below breakdown, the gain below breakdown is typically between two and three orders of magnitude lower than that above. Thus equation 5.4 gives a close approximation of the true breakdown voltage.

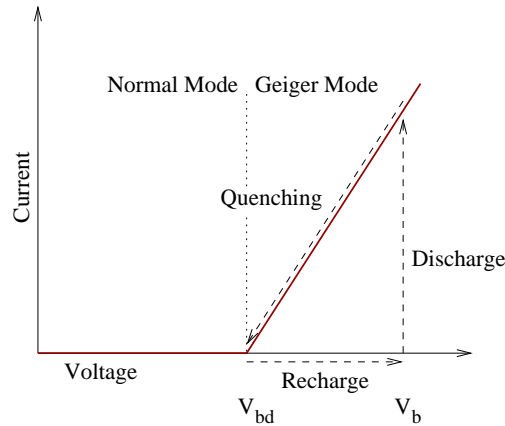


Figure 5.2: Discharge and quenching cycle of a typical APD operated in Geiger mode in series with a quenching resistor

The total charge output of a GAMPD is given in quantised units of pixel triggers or photoelectrons. Each pixel of a GAMPD is assumed to be identical and so the charge output is given by;

$$Q_{total} = \sum_{i=1}^{N_{trigger}} Q_i \quad (5.5)$$

The operating bias of a GAMPD depends on the value of the breakdown voltage and desired gain. However, it is not possible to produce infinite gain. As shown in Figure 5.1, each APD is connected in series with a quenching resistor. When the APD undergoes Geiger discharge, there is a rapid flow of current through the quenching resistor. The discharge of the APD continues until the current flow through the quenching resistor causes a significant drop in voltage reducing the voltage across the APD below the breakdown voltage. Once quenched the APD recharges with a characteristic time of $\tau = R_q C$. This process is shown in Figure 5.2.

5.2.1 Temperature dependence of gain

The most important temperature dependant parameter affecting the gain is the breakdown voltage shown in equation 5.4. The temperature dependence of this parameter is discussed qualitatively in section 4.4.2. The affect of this dependence is that at a fixed bias voltage, an increase in the temperature will increase the breakdown voltage and thus reduce the over-bias and in turn the gain. By controlling the over-bias it is possible to operate the

GAMPD at the same gain through a large range of temperatures.

5.3 Photon detection efficiency

For many photo-detectors the conversion factor between input photons the number detected is known as the quantum efficiency (QE). In a classic vacuum photo-multiplier tube (PMT) the quantum efficiency depends on the efficiency of the photo-cathode to produce electrons via the photo-electric effect that can then undergo avalanche amplification through acceleration by a high electric field and impact ionisation. Typically the peak QE of a PMT is of the order of 10-20% although recent developments have yielded PMTs with a peak QE of 38% [66]. In contrast, semiconductor detectors have been designed and manufactured with a peak QE of 80% [67].

A different parameter known as photon detection efficiency (PDE), must be considered for GAMPDs. While it is possible to produce a single APD with a QE of 80% the GAMPD is composed of hundreds of APDs, with external structure such as bias delivery and quenching resistors and thus it is not 100% sensitive to photons. Thus the PDE of a GAMPD is defined by the following expression,

$$PDE(\lambda, V) = QE(\lambda) \times \sigma(V) \times GE, \quad (5.6)$$

where σ is the avalanche probability and GE is the geometrical efficiency of the array. QE here is a conventional conversion factor between number of photons incident on an APD and the number of electrons produced by photo-ionisation in silicon.

5.3.1 Avalanche probability

In order to trigger an avalanche a charge carrier must be generated near to the depletion region of the APD. However, not all carriers generated in this region result in an avalanche. In order to result in a Geiger-mode avalanche the carrier must produce an electron hole pair via impact ionisation, these secondary carriers must then go on to repeat the process to produce tertiary carriers and so on. Avalanche probability has been modelled theoretically

by Oldham *et al.* [68], and it is found that avalanche probability depends upon the structure of the APD, the type of carrier initiating the avalanche and the applied over-voltage. The avalanche probability is higher for electron-induced avalanches than holes, following the differences in ionisation rate for electrons and holes as discussed previously (Section 4.5). The observed avalanche probability for a test APD [68] for hole-induced avalanches is between 0% and 20% and for electron induced avalanches between 0% and 60% for an applied over-voltage between 0 to 2V. Thus the avalanche probability may vary for the APDs of a GAMPD depending on the design and majority carrier used to initiate avalanches.

5.3.2 Geometrical efficiency

The geometrical efficiency is the the fraction of photo-sensitive to non-photo-sensitive area of the array, and plays an extremely important role in setting the maximum PDE of a GAMPD design. As stated previously, in order to separate the APDs of a GAMPD trenches or guard rings are used. These structures are a vital part in understanding the origin and control of an undesirable effect known as crosstalk between pixels. In terms of geometrical efficiency these regions are ‘dead’ space with the sole purpose of isolating one pixel completely from its neighbour. The dimensions of an optical trench or guard ring for most purposes are fixed for a particular APD design, and in general are not scaled with the total dimensions of the APD. This has a very large impact on the geometrical efficiency of a GAMPD when forming designs using a fixed total area and miniaturising the APDs to produce GAMPDs with different total number of pixels.

For example using the pixel pitch and the width of the surrounding trench as illustrated in Figure 5.3, it is possible to predict the geometrical efficiency (GE) by use of simple area considerations as follows:

$$GE \sim \frac{\text{active area}}{\text{total area}} \sim \frac{(p - 2t)^2}{p^2} \quad (5.7)$$

where p is the pixel pitch and t is the trench width. If a $1 \times 1 \text{ mm}^2$ GAMPD with 400 square pixels is considered, the pixel pitch will be equal to $50\mu\text{m}$. If each pixel is surrounded by a trench making a border of $5\mu\text{m}$, the GE calculated by equation 5.7 is 64%. If the same pixel design is miniaturised to a pitch of $25\mu\text{m}$ but the width of the

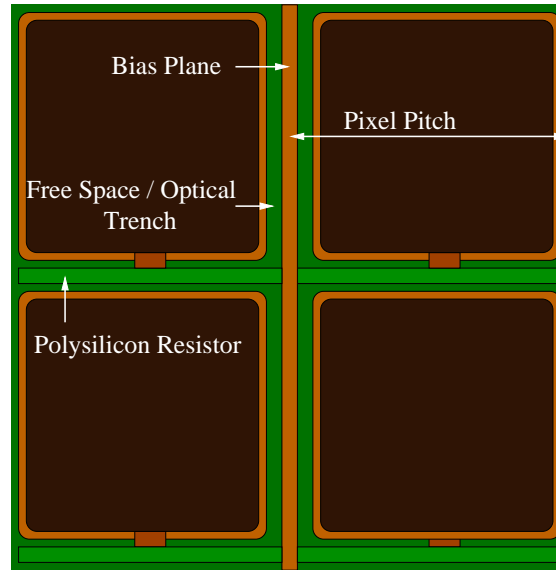


Figure 5.3: The general surface layout of a GAMPD showing 4 pixels with bias chain, quenching resistors and free space for trench or guard rings.

border is fixed, the $1 \times 1 \text{ mm}^2$ will be made of a 40×40 array of pixels. The predicted geometric efficiency of this configuration would be 36%. This example is demonstrated in Figure 5.4.

The general trend for a series of GAMPD manufactured with the same area but different number of pixels is that as the number of pixels is increased, the GE decreases, this in turn decreases the PDE of the device. The width used as a trench or free space is the limiting factor in this case, and the design of the trench to separate the component APDs can take a number of forms and will be discussed in section 5.5

5.4 Dynamic range

Due to the finite number of constituent pixels operating in Geiger-mode, the charge output of a GAMPD becomes non-linear as photon illumination increases. The non linearity is a direct consequence of Geiger-mode operation, as multiple photons absorbed by a single pixel will cause a trigger producing charge equal to that if a single photon was absorbed. This means as the photon density arriving at the GAMPD increases the charge output will be lower than what is expected just by considering the PDE.

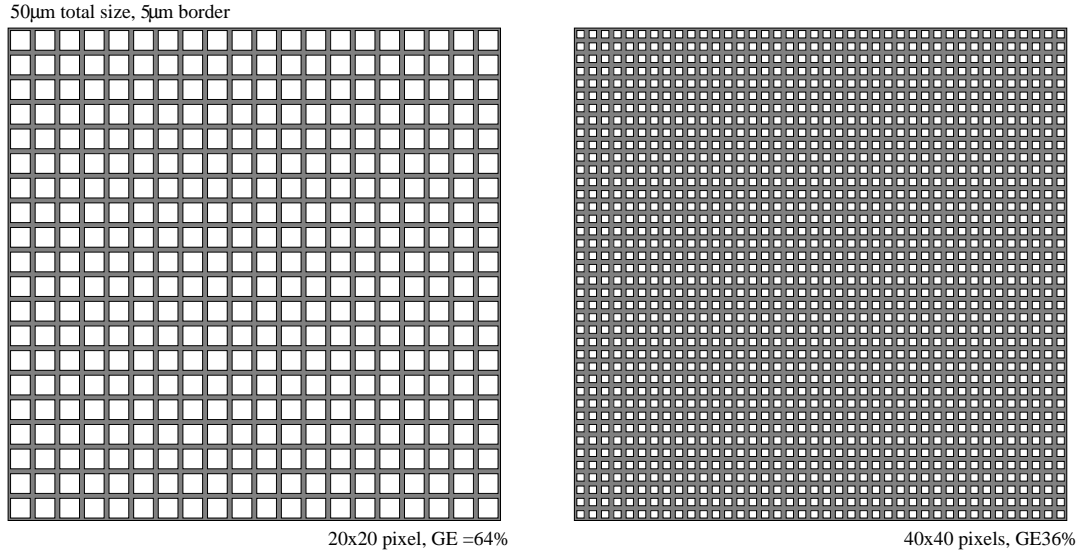


Figure 5.4: Effect of decreasing the pixel size on geometrical efficiency

In order to model the response of a GAMPD to increasing photon illumination one should consider the probability of a single photon causing an pixel trigger when a number of pixels of the GAMPD have already been triggered by incident photons. This accounts for increasing the occupancy of the array and increasing insensitivity to photons. By applying a Poisson distribution to the number of incident photons the mean number of APD triggers can be obtained from:

$$N_{trigger} = N_{pixels} \left(1 - \exp \left(\frac{-\sigma N_{\gamma}}{N_{pixels}} \right) \right) \tag{5.8}$$

where σ is the PDE of the GAMPD, N_{γ} is the number of photons incident on the active area, N_{APD} is the number of APDs contained in the active area. At low N_{γ} the response of the device is linear, however as N_{γ} increases the output flattens and reaches a maximum of N_{APD} [69]. This relationship is shown in Figure 5.5 for 4 different PDE values and for the case of 100 and 200 pixels.

5.5 Crosstalk

The pixels of a GAMPD are separated using trenches. The the reason for such structures is to reduce crosstalk between pixels. Crosstalk manifests as a pixel undergoing Geiger discharge and initiating a discharge near instantaneously in a neighbouring pixel, were

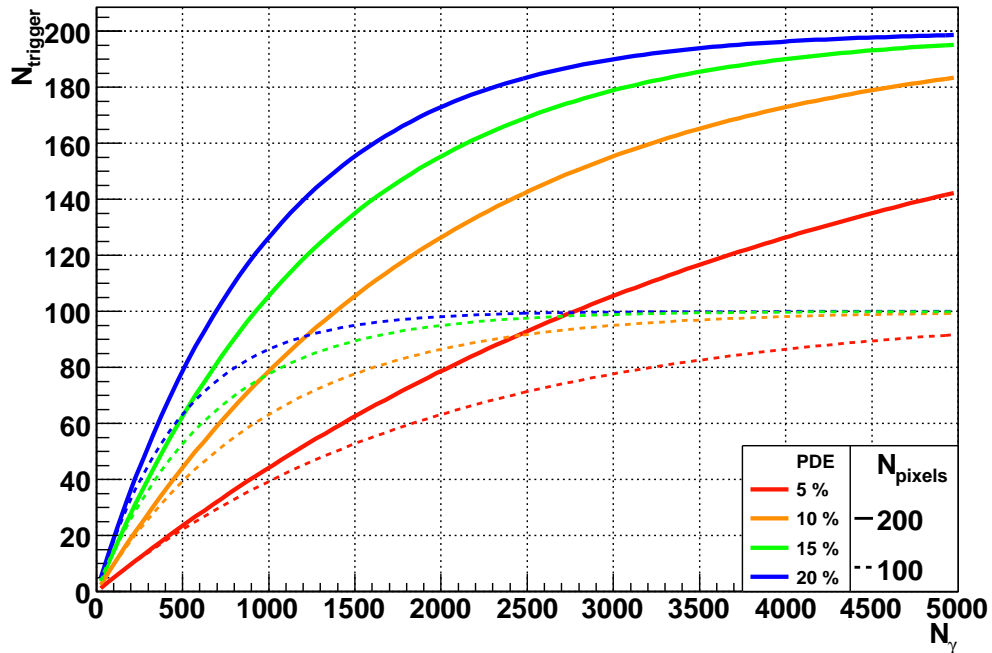


Figure 5.5: Typical linearity curves for GAMPDs with 100 (dashed line) and 200 (solid line) pixels, demonstrating how the linearity is effected by both the PDE and the total number of pixels. Devices with low PDE and constructed from high numbers of pixels are predicted to produce the most linear response to increasing light intensity.

the initial discharge is caused by either absorption of a photon or thermal excitation (Section 5.7). Crosstalk is mediated by photons produced inside the APD via electron-hole recombination during an avalanche [70]. The rate of photon production is found to be approximately 3 photons per 10^5 carriers. The photon emission is described by a Boltzmann distribution of wavelengths with a temperature of 4000 K [71]. As shown previously in Figure 4.4, photon absorption by silicon is strongly wavelength dependant. Thus photons produced at short wavelengths will be reabsorbed within a short distance (of the order 10^{-6} m), however photons produced at an energy close to the band-gap energy will travel much longer distances. The band-gap energy of silicon is 1.1 eV, resulting in a photon of wavelength 1130 nm. The absorption coefficient at 1130 nm in silicon is 133 m^{-1} and a 1/e absorption length of 7.5mm. A typical GAMPD is of the order of 1-2 mm maximum dimension, thus it is possible that a photon produced travelling in the plane of the device during a Geiger discharge can pass through the silicon into a

neighbouring APD and cause optical crosstalk. The purpose of a trench around a pixel is to remove this direct path between pixels.

5.5.1 Optical trench

An optical trench is a region surrounding a pixel that has been etched away to form a physical groove or trench in the surface of the silicon. Any photons arriving at the trench are then subject to total internal reflection if arriving at the critical angle, transmission or absorption. It is also possible to coat the inside of the trench with a reflective material to further promote reflection. Two pixels separated by an optical trench are shown in Figure 5.6. Also shown are example photon paths through the silicon resulting from a photon induced avalanche, however this example is also valid for thermally produced avalanches (Dark triggers). The trench between pixels reduces direct crosstalk between pixels by reflecting incident photons. Photons emitted toward the substrate surface however will not interact with the trench, but can still result in photon-induced crosstalk.

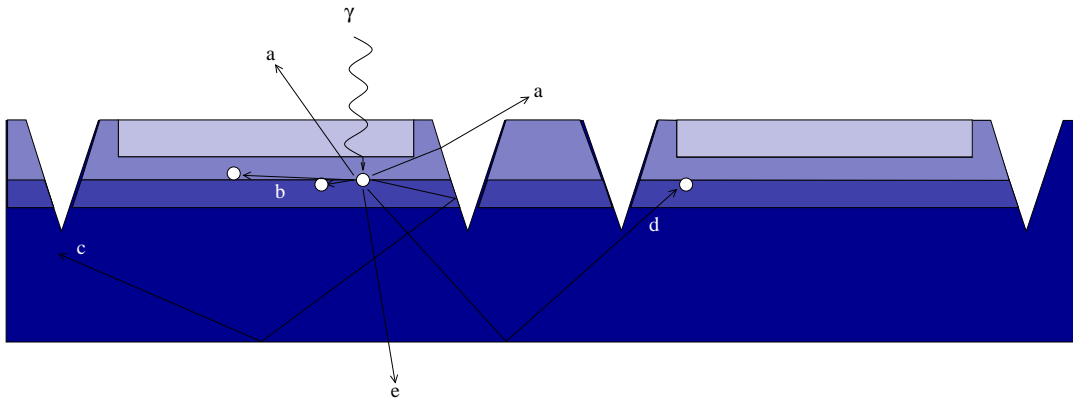


Figure 5.6: Example of optical trenches separating neighbouring pixels. Paths are shown for photons produced inside the pixel.

- a) Photon loss from front surface.
- b) Short wavelength re-absorption within the pixel
- c) Photon undergoing total internal reflection at the trench and substrate surface.
- d) Photon undergoing total internal reflection at the substrate surface and being reabsorbed by a neighbouring pixel
- e) Photon loss from the back surface

5.6 Trapping and afterpulses

During an avalanche, carriers can be trapped in energy levels within the semiconductor band-gap. These levels are often caused by local imperfections and impurities in the crystal lattice. The lifetime of trapped carriers is typically in the nanosecond range. Due to the trapping and subsequent decay of traps in the depletion region, these carriers have a probability of producing delayed avalanches known as afterpulses. How afterpulses effect a GAMPD depends upon the recovery time of the component pixels. The recovery time of the pixel can be estimated by the RC constant of the component APD and quenching resistor. If the RC time of the pixel is longer than the mean lifetime of a trap then the carriers will be released at a time when the pixel is discharging or at an early stage of recovery and has little gain. However if the RC time is much shorter than the mean lifetime of a trap, then carriers released from traps resulting in an avalanche will cause detectable delay pulses. S. Cova developed a technique detailed in [72] in order to measure the afterpulsing rate of an APD, reporting lifetimes ranging from nano to microseconds.

5.7 Thermal noise

As stated in Section 4.1 due to the small band-gap of a semiconductor, an electron can be promoted from the valence to the conduction band via thermal excitation. If this occurs near or within the depletion region of the APD there is a probability of causing an avalanche. The rate at which the pixels of a GAMPD fire due to random thermal fluctuations is thus dependant upon the volume of the depletion region and the probability of a generated charge carrier resulting in a Geiger discharge. Output pulses caused by this mechanism are known as dark pulses or dark count. The fundamental parameters controlling these effects externally are bias voltage and temperature. Increasing the bias voltage applied to the GAMPD causes an increased electric field across the pixels. At a typical GAMPD operating bias, the depletion region is saturated and will not increase in volume by a significant amount, however the increased electric field across the depletion region will allow charge carriers to gain more energy as they drift toward or through the depletion region. This increases the probability a charge carrier will obtain enough energy to cause impact ionisation and in turn initiate an avalanche.

Increasing temperature has a two fold effect on the GAMPD, at higher temperature the thermal excitation rate of the pixels will naturally increase, and the breakdown voltage will increase. Thus the dark count rate will rapidly increase with temperature at a fixed gain.

Dark count rate is thus highly problematic for a GAMPD due to the large number of pixels. The dark count rate for a GAMPD can vary greatly and, currently the control of dark count rate has proven to be problematic. Devices manufactured with identical structures show a large range of dark count rates, rates upward of 1 MHz are common (See Figure 6.9 for typical values).

5.8 Experimental operation and features

Due to Geiger-mode operation, the output of an pixel has two conditions, ‘triggered’ or ‘off’ where the default condition is off. The triggering of a pixel occurs via photon absorption or through thermal activation, and produces one unit of charge. However due to the use of multiple pixels and a common bias chain and substrate, if two pixels are triggered then two units of charge are combined. The result of this is that the charge output of the device is quantised into units of charge, or pixel triggers. This is often referred to as pixel fires or single photo-electron pulses. Using simple readout electronics such as a preamplifier and an oscilloscope it is thus possible to observe this quantisation as voltage pulses with integer steps in height. This behaviour is a powerful feature of a GAMPD allowing accurate photon counting of low intensity light pulses. An example of a GAMPD responding to a low intensity light emitting diode (LED) pulse is shown in Figure 5.7.

5.9 Experimental apparatus

In this section the experimental apparatus used to obtain key GAMPD parameters is discussed. The apparatus described represents the minimum requirement to perform basic measurements. The experimental setup is split into control and data acquisition. Typically the control components are those that deliver bias, control the temperature and project photons onto the GAMPD if required. Such components are either physical experimental

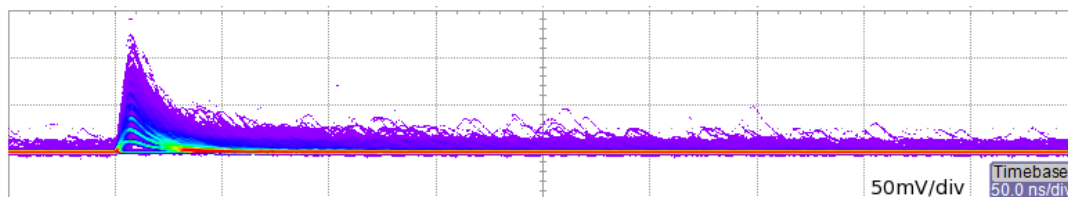


Figure 5.7: Typical persistence plot of a GAMPD. The arrival of the LED pulse at the GAMPD is shown by the large triangular pulse at a time of approximately 50ns. The response of the GAMPD is quantised and is easy for an observer to distinguish the numbers of APDs triggered

apparatus or electrical components. Data acquisition in this case refers to the full read-out chain of the GAMPD. In order to perform a typical experiment on the GAMPD an experimental setup is required that meets a strict set of requirements in order to control all GAMPD parameters throughout and readout the response as accurately as possible.

The basic design of the experimental setup is shown in Figure 5.8. Each component of this chart will be discussed in detail in order to provide an understanding of important features, and the reasons for its choice.

5.9.1 Data acquisition

Amplifiers

In order to readout the GAMPD two options are presented; readout by a load resistor or using an amplifier Figure 5.9 a) and b). In both cases the observed voltage follows a $V_{out} = IR$ relationship using the labels shown. In the case of load resistor, readout of the GAMPD is presented with the following limitations. The current output of a typical GAMPD is of the order of 10-100 nA thus in order to produce a voltage pulse of detectable amplitude a large load resistance is required. The use of a high load resistor results in higher levels of noise on the output reducing the signal to noise ratio, and gives the system a high time constant $\tau = RC$. The high time constant is problematic as the described system will have a recovery time of the order μs . It follows that the GAMPD output pulses due to dark count will be subject to signal pile-up, and effects such as afterpulsing are impossible to study. In the case of a operational amplifier, a large feedback resistance

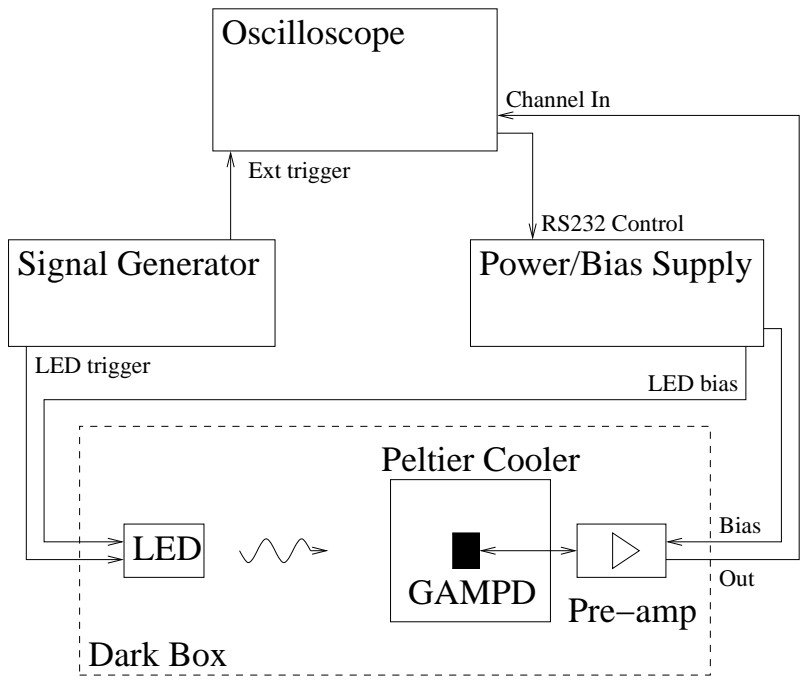


Figure 5.8: Chart of a typical experimental setup including electrical connections and communication between each component

can be used to give produce detectable voltage pulses at the output without imposing long recovery times on the system. In this system the recovery of the GAMPD is mainly dependant upon the capacitance of the component APDs and quenching resistors.

During the course of this thesis two amplifier designs have been used, the first based around a National Semiconductors LMH6624 [73] (Figure 5.10) and later an Texas Instruments OPA847 [74] (Figure 5.11). Each is selected for low-noise, wide-bandwidth and high gain

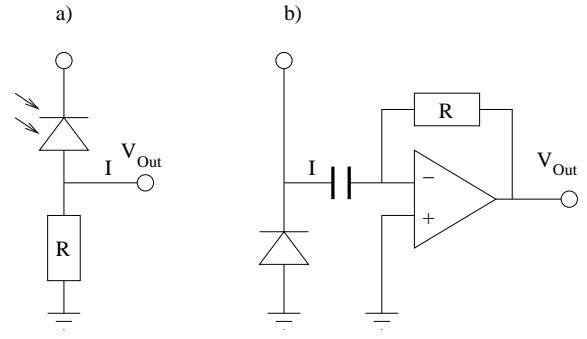


Figure 5.9: Simple readout options for a generic photosensor, (a) Load resistor readout and (b) Trans-impedance operational amplifier readout.

operational properties. Each design is based upon examples set out by the component datasheets.

When required, an extra stage of amplification is added between the pre-amplifier and the read-out system to provide extra gain. Typically this is required when working with low gain GAMPDs in order to increase the separation between multiple pixel triggers. When extra amplification is required an Ortec 474 [75] is used, providing a wide range of gain factors between 2 and 250X.

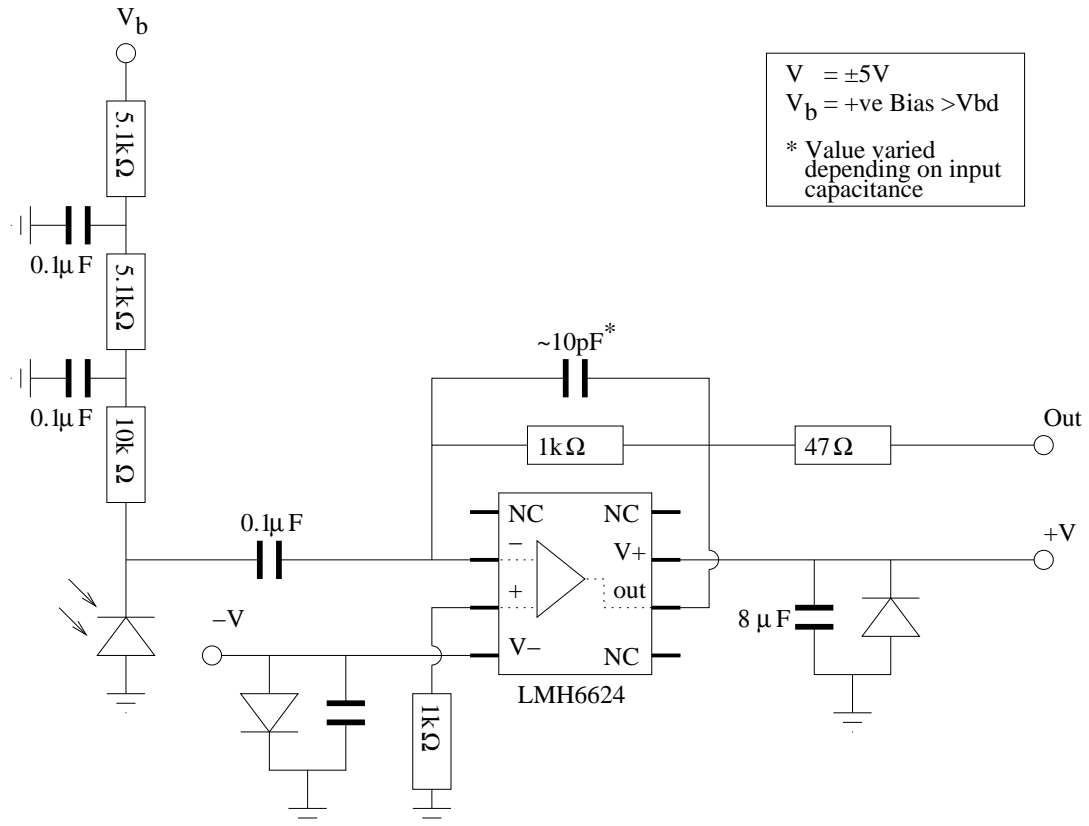


Figure 5.10: Trans-impedance pre-amplifier based on an LMH6624

Analogue digital converter

The majority of experiments performed on the GAMPD require the measurement of charge from the GAMPD, thus a charge integrating analogue digital converter (ADC) is required. Commonly an ADC is an independent electronic module with ADC inputs and a integration gate input. Thus the user must supply a logic pulse of the desired integration length

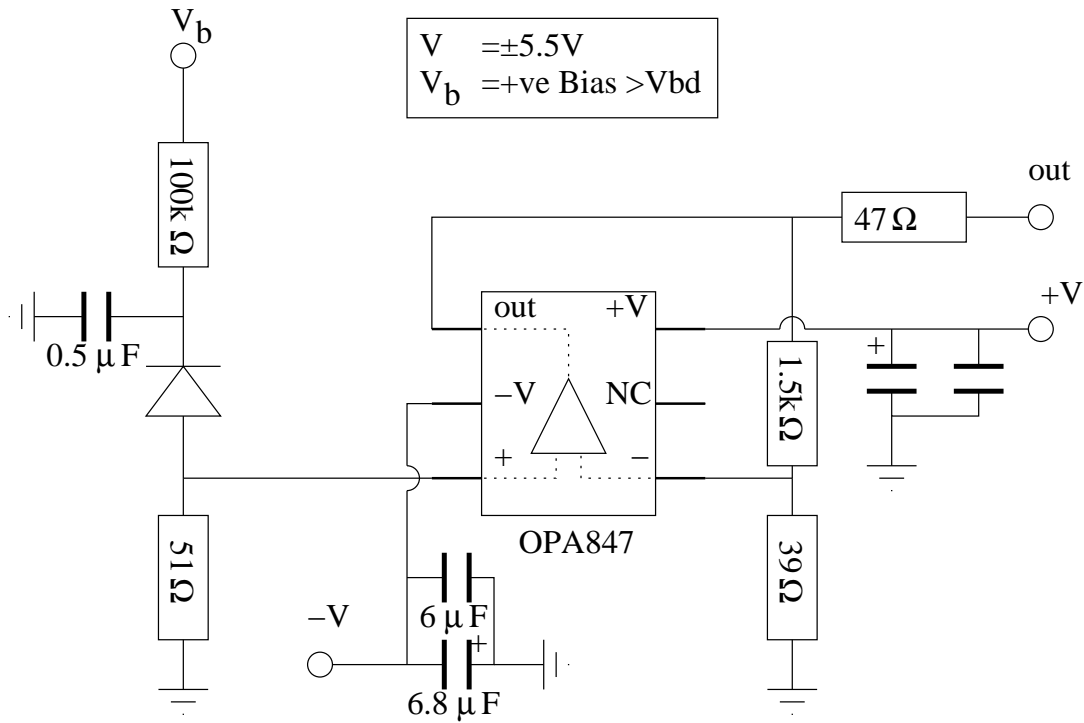


Figure 5.11: Non-inverting pre-amplifier based on an OPA847

to the ADC. If the experiment requires synchronisation of the integration gate with an event such as an LED flash, this logic pulse must be synchronised with the flash. Readout of the ADC is commonly performed using a personal computer. In order to negate the requirement of 3 separate pieces of lab equipment a LeCroy 6100 waverunner oscilloscope is selected as the final readout module [76].

The oscilloscope provides waveform digitisation at 10 Giga-samples/s with 8.5 bit vertical accuracy, running a user interface over Microsoft Windows 2000. Synchronisation of the oscilloscope with an event is performed in a similar fashion as described for the separated ADC module except a simple trigger pulse is used to trigger the oscilloscope. Fine tuning of the integration gate is performed completely within the user interface.

5.9.2 Control

Power/bias supply

In order to operate the GAMPD bias must be applied to the anode or cathode. This bias must be stable to within 5mV and not drift over the course of an experiment. The bias voltage required depends upon the breakdown voltage of a GAMPD and is typically between 25-70 V depending on design. Thus a bias supply must be capable of delivering bias up to and beyond this range. A Hameg Instruments HM7044 [77] is selected for this purpose as it meets all the above requirements. It has 4 channels each capable of delivering 32 V at 3 A, meaning it can supply a bias of up to 128 V if chained together. This power supply also features remote control via RS232, which is important for experimental automation.

LED - Sheffield pulser

The GAMPD is a photo-sensitive device hence it is common to use a photon source to trigger the pixels in order to study their properties and parameters. This source must provide a flash of photons within a period of time similar to the recovery of the pixels. The source must also be stable, in that the absolute number of photons emitted per flash does not vary significantly during an experiment.

These requirements are met by an LED pulser system developed at the University of Sheffield for use in the ANTARES experiment to calibrate PMTs [78]. The pulser is based on a circuit developed by Kapustinsky [79] to produce a fast rise time, short duration pulse from commercially available LEDs for the purpose of testing scintillation detectors. The pulser is contained on a 27x13 mm printed circuit board and requires the application of a bias voltage between -5 and -24 V, with a 200ns negative going square wave of amplitude >2.5 V superimposed in order to trigger a flash. The flash of the LED occurs on the positive going edge of the square wave. The external connection, for operation is shown in Figure 5.12 and a full list of parameters are given in Table 5.1.

Parameter	Value
λ	470 nm
Rise Time	<2 ns
Pulse width	<4.5 ns
Photons per flash	$\sim 10^8$
Operating Voltage	-24 V
Operating Frequency	<20 kHz

Table 5.1: Pulse and operational specifications of the Sheffield LED pulser.

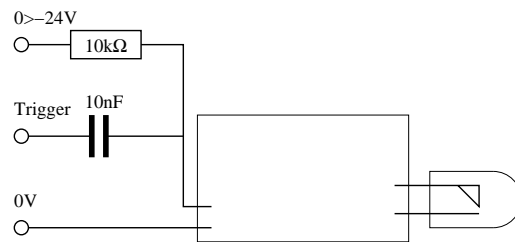


Figure 5.12: External circuit required to operate the Sheffield LED Pulser

Temperature control

As discussed previously in section 4.4.2 the breakdown voltage of the GAMPD depends strongly on temperature. Thus in order to perform an experiment on the GAMPD to study any parameter the temperature must be controlled. The temperature must be known and controlled to within <0.5 °C. This can be achieved using a number of methods such as a temperature controlled room, via use of air-conditioning or a controlled chamber inside which the experiment is constructed. An air-conditioned laboratory and temperature controlled chamber were unavailable during the construction of the experimental setup at Sheffield. Thus a localised temperature control system has been devised using a Peltier heat pump.

The temperature control consists of three components; the Peltier heat pump, a LM35 temperature probe and a feedback logic system. The heat transfer through the Peltier depends upon the applied voltage across the terminals of the Peltier. The feedback logic operates by altering the voltage applied to the Peltier in order to equalise the temperature on the cold side of the Peltier measured by the LM35 and the temperature set by the

user [80].

Controlling and measuring the temperature of a GAMPD is challenging as the device is often physically small and the active area must not be obscured by any external connector or mechanical stabilisation. The design of the temperature control and mechanical stabilisation has thus been altered and improved to meet changing requirements throughout this thesis. Each will be discussed in the during the following sections. A common feature throughout is the use of a heatsink on the ‘hot’ side of the Peliter to dissipate the heat.

Measurement automation

All apparatus as described can be operated manually by the user, however components such as the oscilloscope and power supply can be connected and perform several measurements without the need for user interaction. As described previously, the oscilloscope user interface operates over a Windows 2000 O/S, and it is this feature that is key in automating the experimental setup. The user interface is controllable remotely via TCP/IP or GPIB and the PC allows connection with components and devices to be made via Ethernet, USB and RS232. This functionality is key to automation of the presented experimental setup. The PC allows the user to run software such as LabVIEW [81] and use tools supplied by LeCroy to interface with the oscilloscope via TCP/IP and the bias supply via RS232. These tools can be combined to form a control system that sets and cycles the bias voltage while using the oscilloscope to perform measurements and save desired information to disk.

A flow chart of a LabVIEW control application developed by the author, used throughout this thesis is shown in Figure 5.13. The user must setup the oscilloscope to perform a desired measurement manually before the application is run. The application uses the RS232 protocol to communicate with the HM7044 to set the GAMPD bias, while using the oscilloscope trigger mode to control the time in which measurements are performed. A function is performed on each measurement in order to produce a histogram of the measurements. After the desired measurement time is complete a channel or function is readout by LabVIEW and saved to disk. The process is then restarted for a different bias voltage.

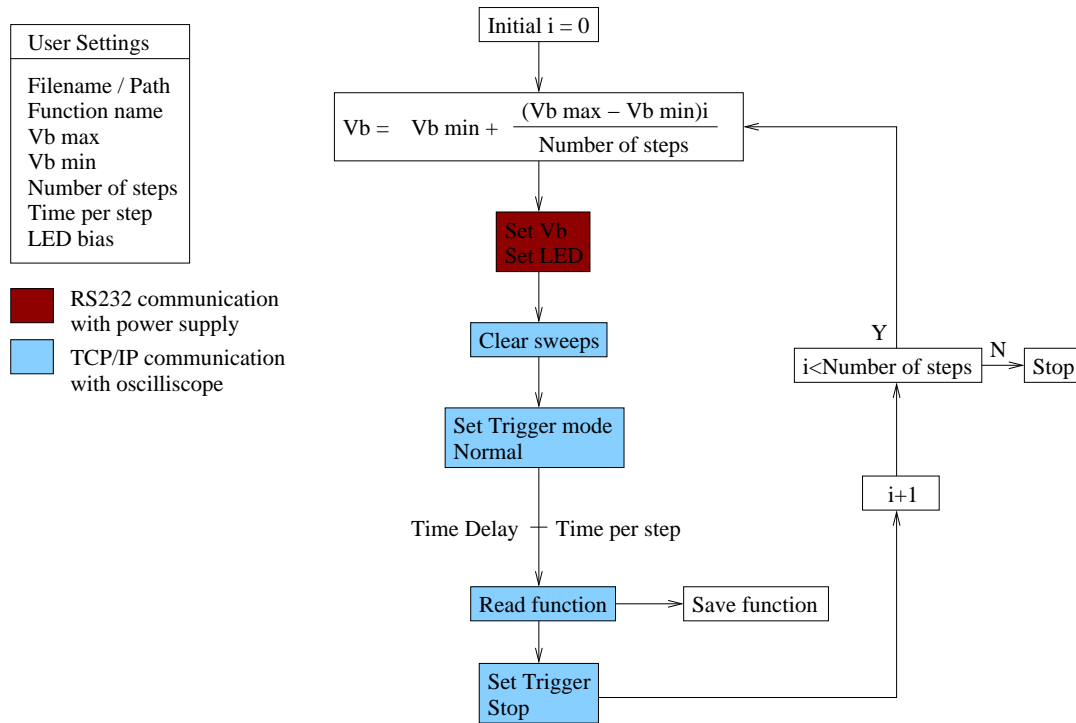


Figure 5.13: Flow chart of major steps made by the LabVIEW automation front end

5.9.3 Experimental environment

In order to study a GAMPD it must be operated in a low light environment. The aim of the experimental setup is the mounting of a GAMPD inside a light tight environment such that only photons produced in a controlled manner are incident upon the device. This requires the LED, temperature control system and pre-amplifier to be situated inside the low light environment.

The experimental setup used throughout this thesis is housed inside a 590x400x330 mm wooden box. It is separated into two parts, a lid and base. All joints and surfaces of the box are made light tight with the application of black sealant and black flock. The base of the box has raised internal edges, externally lined with sponge in order to promote a light tight seal between the lid and base. To provide support and aid alignment of experimental apparatus, a 480mm long mini optical rail is positioned in the centre of the base. In order to allow electrical connection with the outside, a curved black tube is passed through the base. The tube is curved through 90° to bring it horizontal with the base, then curved through 180° and routed to the opposite edge of the base. This formation requires any light to make multiple internal reflections in order to enter the box. Any light that thus does

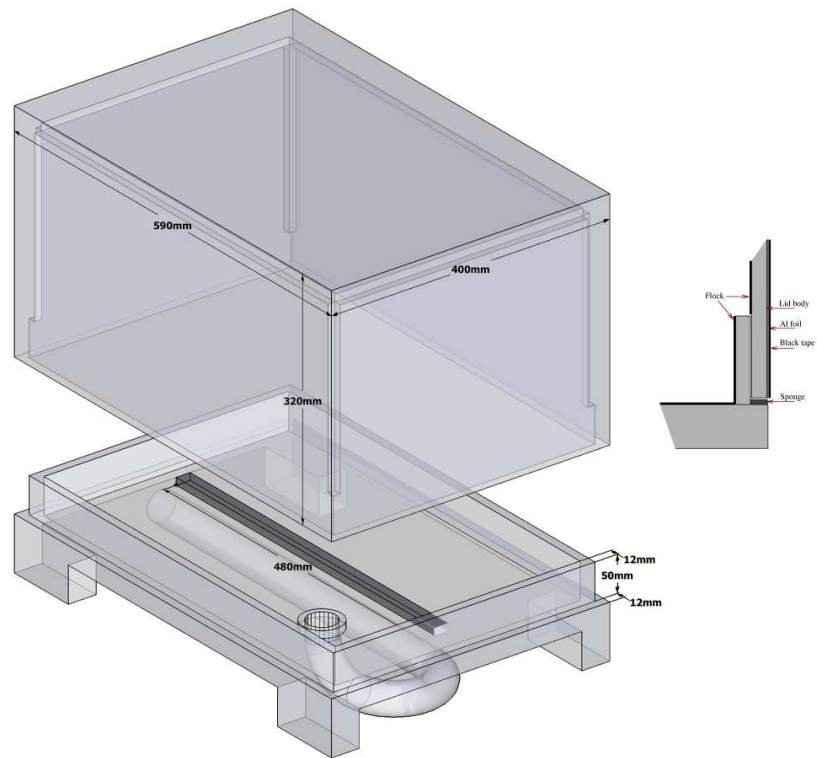


Figure 5.14: Design of the dark-box constructed for GAMPD testing.

enter the box will be projected upwards requiring further reflection in order to illuminate any internal components. The design of the dark-box is shown for reference in Figure 5.14.

5.9.4 Data processing and output

Waveform processing

The LeCroy 6100 oscilloscope is capable of digitising 4 input channels and making 8 simultaneous measurements. Unless stated otherwise the oscilloscope is used to integrate the waveform area in order to extract the charge output of the readout chain. The integration window used depends upon the pulse profile of the GAMPD under examination, amplifier noise and levels of electro-magnetic interference present on channel. The minimum integration window used is set to encompass the whole GAMPD signal pulse (if synchronised with the arrival of an LED flash). However a longer integration window is typically used in order to include effects such as afterpulsing and to mimic the integration window that

will be used in the ECal DAQ. If the integration window is not wide enough, charge is lost from the measurement, reducing the single pixel trigger resolution.

The oscilloscope generates histograms of measurements in real time, updating with each new trigger. A histogram of subsequent pulse area integrations is known as a charge spectrum. It is expected from the description of a GAMPD in section 5.2, that the charge output will depend upon the number of APDs triggered, thus the charge spectrum is expected to feature equally separated peaks.

Charge Calibration

The charge spectra produced by the oscilloscope are in units of Volt seconds. In order to convert this into units of charge the system must be calibrated using a fake GAMPD. The fake GAMPD is small value capacitor (typically ~ 10 pF) which is used to inject a known amount of charge into the pre-amplifier. The fake GAMPD and the resulting output is shown in Figure 5.15. The capacitor differentiates the input square wave, the output thus depends upon the rate of change of the input and two pulses are generated on the edges of the square wave. By changing the amplitude of the square wave, the charge injected can be controlled and is calculated using a $Q = CV$ relationship. In order to convert integrated pulse area from Volt seconds to Coulombs for a given output chain, a short procedure is performed as follows,

1. Capacitance of the fake GAMPD is measured;
2. Amplitude of the input square wave is measured;
3. Resultant pulse is integrated for a set window;
4. The amplitude of the input is increased and the process is restarted at point 2.

This procedure is performed through a range of injected charges similar to that expected by GAMPD. An upper range can be assumed to be 5 APC triggers at a high GAMPD gain. The amplitude of the input pulse that will produce an equivalent charge can thus be calculated as follows;

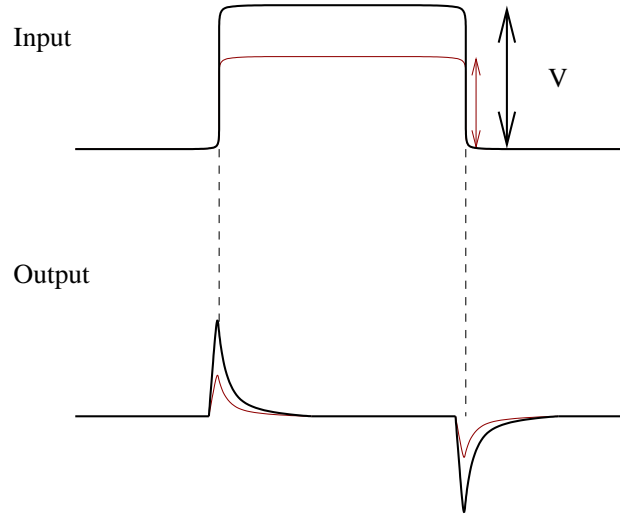
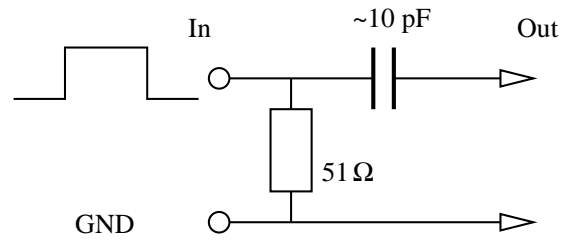


Figure 5.15: Fake GAMPD used to inject a known amount of charge onto a pre-amplifier using a square wave pulse with controlled amplitude.

$$\text{Assume maximum gain} = 1 \times 10^6 \quad (5.9)$$

$$\text{Capacitor used} = 10 \text{ pF} \quad (5.10)$$

$$\text{Charge } Q \text{ of 5 APD triggers} = 5 \times 10^6 \times (1.6 \times 10^{-19})(C) \quad (5.11)$$

$$\text{Input Voltage Required} = Q/C \quad (5.12)$$

$$= 5 \times 10^6 \times (1.6 \times 10^{-19}) / 10 \times 10^{-12} \quad (5.13)$$

$$= 80 \text{ mV} \quad (5.14)$$

A plot of charge vs pulse area is then formed and a straight line fitted through the data points. The gradient of this line thus provides a calibration value. An example data set for 3 gain settings is shown in Figure 5.16. The calibration value is only valid for the

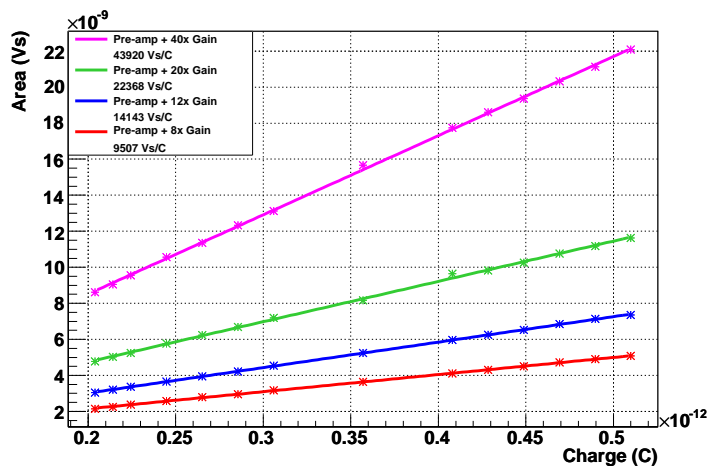


Figure 5.16: Charge calibration example showing linearity of input pulse area against injected charge. This means for the region shown all stages of the readout chain have linear behaviour

output chain the calibration is performed on. If new equipment is added to the chain to provide extra amplification the full chain must be charge re-calibrated.

Output

Information from the oscilloscope may be output in many forms including ASCII, Excel, MatLab and binary. Typically histograms are output and saved to hard disk in space delimited ASCII format for analysis. The filename string used for each histogram is used to record parameters about the experimental setup and the device under test. An example of this is shown below,

```

Serial      Vop      Date      Type
TA3001sn_7096nV_20080917YMD_PED

      _optn_220dC_ 200ns_2639340cl_2639340evt
              Temp  Gate Calibration Ntriggers
    
```

5.9.5 Data taking and types

For a single GAMPD it is possible to take two distinct charge spectra; LED and Pedestal (PED). However a full data set will consist of a bias or temperature scan, these terms are

explained below

LED spectrum Charge spectrum taken from a GAMPD operated at a fixed bias and temperature under low intensity LED illumination. The oscilloscope is synchronised with the arrival of an LED pulse, and the trace integrated over each flash. Typically an LED charge spectrum will show several equally separated peaks. The mean of this distribution depends upon the intensity of the LED pulse. A typical LED spectrum is shown in Figure 5.17(a)

Due to the presence of multiple pixel trigger peaks (photo-electron peaks), LED spectra do not require large statistics in order to successfully extract information. LED spectra can be generated on a timescale of the order of minutes.

Pedestal spectrum Charge spectra taken from a GAMPD operated at fixed bias and temperature isolated from all sources of photons. The oscilloscope is triggered using a pulse generator and the trace is integrated on each trigger. Due to the random nature of dark count triggers it is expected that the majority of traces contain no charge, and thus the spectrum will feature a large ‘pedestal’ peak, with a lower distribution of dark count triggers. A typical PED spectrum is shown in Figure 5.17(b).

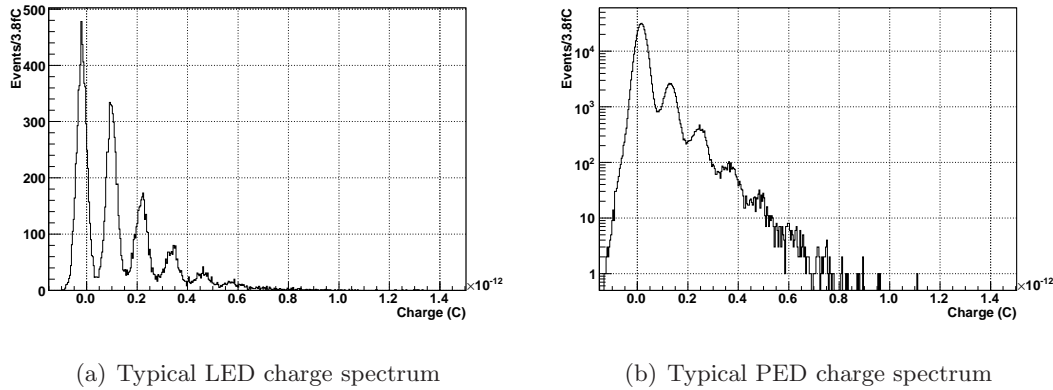
Due to the low probability of integrating traces with APD triggers caused by thermal excitation, a pedestal spectrum must include large statistics in order to clearly observe the one or more photo-electron peaks. This requires the data taking time to be longer than a typical LED charge spectrum by up to $3\times$ depending upon DAQ speed.

Bias scan The production of charge spectra for a range of bias voltages.

Temperature scan Performing bias scans through a range of GAMPD temperatures.

5.10 GAMPDs Studied

In this section a basic profile for each tested device is given with a typical operating voltage and an upper gain limit. Each device is listed in the order samples were received.



(a) Typical LED charge spectrum

(b) Typical PED charge spectrum

Figure 5.17: Charge spectra for a GAMPD operating at a gain of 7×10^5 at a fixed temperature of 22.0°C

5.10.1 Metal Resistive Silicon APD

Metal Resistive Silicon Avalanche Photo-Diodes (MRS APDs) were first produced by Centre of Perspective Technology and Apparatus - Moscow (CPTA), and were the first device tested during this study. The substrate is glued to the top of a TO-18 transistor can, and coated with epoxy. Two prototype models were available to study, the 0509 series and 1710. Both series use square $40 \mu\text{m}$ pitch pixels arranged in a circular array approximately 1 mm in diameter and composed of 556 pixels. The pixel layout and design is shown with a magnified image of a single pixel in Figure 5.18. This design has been further developed by Photonique SA, with the purpose of optimising and public marketing [82].

The MRS APDs typically operate at a bias voltage of 50 V through a range of approximately 3 V and produce a photoelectron gain up to 6×10^5 at 25°C . A small connector designed to hold the TO-18 packaging inline with a fibre was supplied with the devices. It is a tapered plastic cylinder providing a push fitting with the packaging.

In order to stabilise the temperature of the device the packaging is glued to a aluminium plate thermally coupled to the cold side of the heat pump.

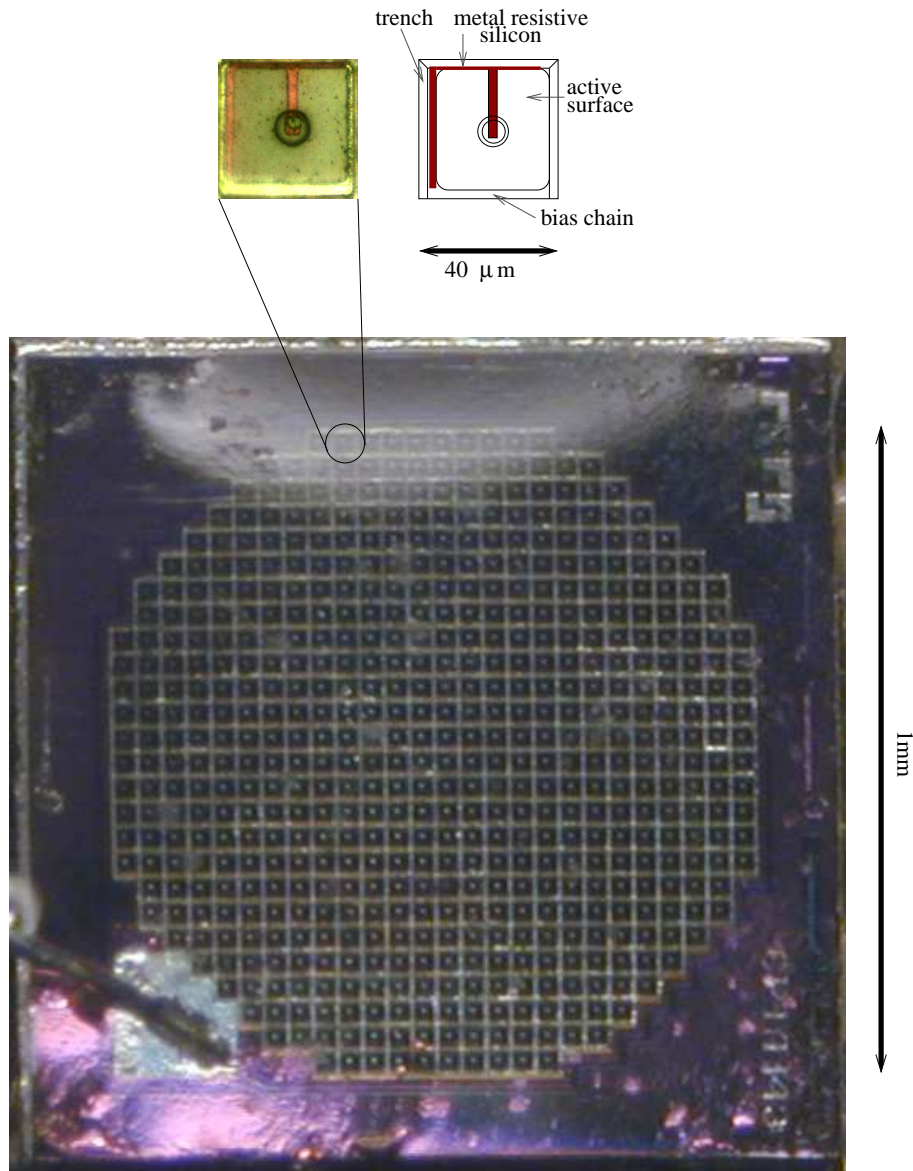


Figure 5.18: Pixel design and total surface layout of the MRS-APD produced by CPTA. It contains a total of 556 pixels in a roughly circular configuration. A labelled diagram identifying each component of a single pixel is shown for reference.

5.10.2 Multi-Pixel Photon Counter

Multi-Pixel Photon Counters (MPPCs) were developed by Hamamatsu Photonics (HPK) [65], the first prototypes being studied in Japanese institutes in 2005 [83]. In 2006 more prototypes became available, all 1 x 1 mm, with three different pixel pitches, 25, 50 and 100 μm . This produces devices with 1600, 400 and 100 pixels respectively.

Recently devices have been produced with larger areas and in arrays of MPPCs as Hamamatsu further developed the technology for use with scintillators. This development has produced a 1.3 x 1.3 mm MPPC based on the 50 μm pitch pixel. This design is optimised to provide an oversize active area to allow better coupling with a wavelength shifting fibre. The pixel design and device layout for both the 1 x 1 mm device is shown in Figure 5.19. The difference between the two designs is that the 1.3 x 1.3 mm device is a 26 x 26 array, with a 3 x 3 array cut out of one corner in order to receive a bonding wire.

MPPCs typically operate at a bias voltage of 70 V through a over-voltage range of approximately 2 V and produce a photoelectron gain up to 1.3×10^6 .

The first devices studied during this thesis are all 1 x 1mm, 20 x 20 array of pixels (400 total) MPPCs in ceramic packaging. The serial numbers of these devices are prefixed S10362-11-[pixel pitch]C, C denoting ceramic packaging. Devices with 1.3 x 1.3 mm active area composed of 667 pixels where tested at a later time, when final production devices became available. A custom connector was designed around the ceramic packaging to couple the MPPC with a fibre. The connector is described in section 6.4.3.

5.10.3 SPMMini

The SPMMini is a device developed by SensL [84]. SensL have developed several GAMPD and thus are available in a number configurations of pixel pitch, array size and shape. The device obtained and studied is composed of a square array of 1 x 1 mm array of 32 x 36 pixels (1152 total) and is shown in Figure 5.20. The pitch of each pixel is 31 μm .

The SiPM mini typically operate at a bias voltage of 30 V through a range of approximately 5 V and produce a photoelectron gain up to 2.5×10^6 .

5.10.4 GAMPD sample list

Provided is a list of GAMPDs that underwent initial testing before a device was selected for use with the T2K experiment. Included in this list is all information provided by the respective manufacturer

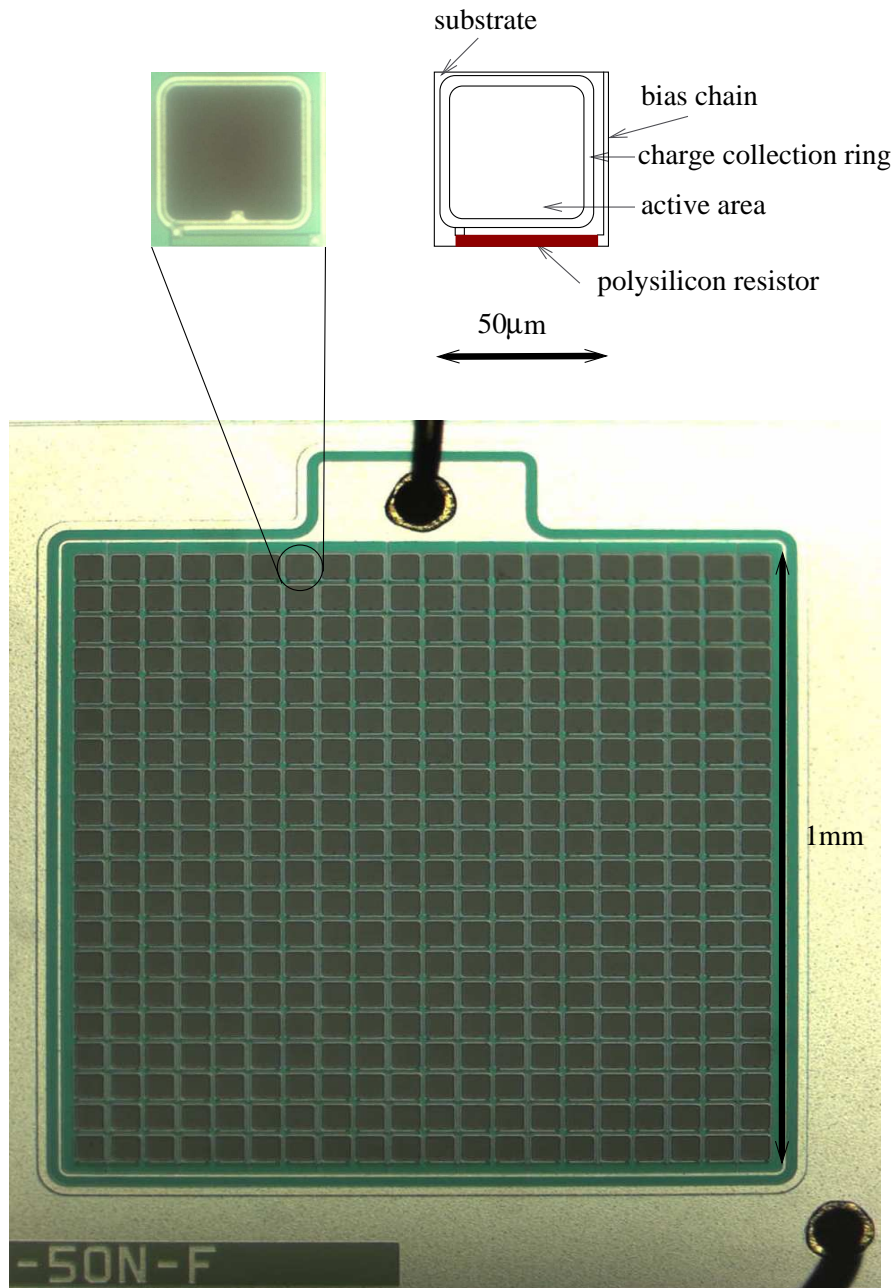


Figure 5.19: Pixel design and total surface layout of the MPPC produced by Hamamatsu.

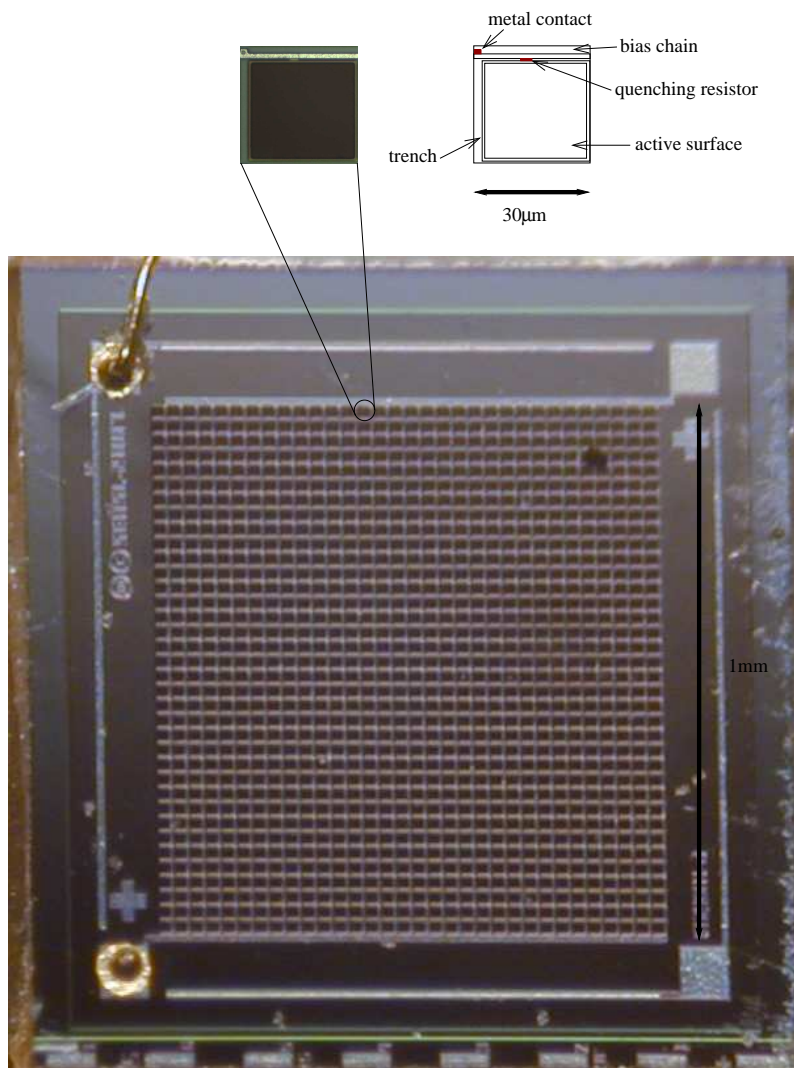


Figure 5.20: Pixel design and total surface layout of the sample SPMMini produced by SensL

Device		V_{op} at 25.0°C	Gain at V_{op}	Dark rate (kHz)	
				at 0.5pe	at 1.5pe
HPK	S10362-11-50C #69	70.59	0.751×10^6	270	10.0
	S10362-11-50C #70	70.11	0.748×10^6	396	14.0
	S10362-11-50C #71	69.77	0.751×10^6	461	24.2
SensL	SPMMini	30.0	1.00×10^6	<1000	NA
CPTA	1710-015	48.0	0.50×10^6	NA	NA
CPTA	0509-023	39.1	0.50×10^6	NA	NA

Chapter 6

GAMPD Parameter extraction

Throughout this section the ROOT analysis framework [85] has been used to extract information from charge spectra and to manipulate data. This section contains detailed descriptions of the approaches taken when analysing charge spectra and data sets.

6.1 Gain

Gain extraction is the first step taken for all analyses. It focusses on determining the exact location and the separation between successive APD trigger peaks. As a charge spectrum can contain multiple peaks (Figure 5.17), the mean separation between peaks is required to give an accurate measurement of the charge output of a single APD.

In order to calculate gain, the following process is performed, example spectra are shown in Figure 6.1(a) – 6.1(d)

1. Charge spectrum is smoothed using an routine based on the 353QH algorithm [86]. This is to enhance spectra that have poor statistics and to help reduce misidentification of charge peaks by step 2.
2. Use TSpectrum peak finder to locate a desired number of peaks. For a PED spectrum, the number of peaks is set at two due to low statistics.
3. Resulting peak locations are sorted in charge order and the mean separation is

calculated.

4. Peak position and mean separation are used as inputs for the mean and sigma of Gaussian functions. The Gaussian functions are fitted using TMinuit least squares minimisation to the unsmoothed charge spectrum using the mean separation as a fit range.
5. The sigma of the resulting fits are used to set final fit ranges and Gaussian fits are re-applied. This step is to ensure the fit is applied to the same range either side of the mean.
6. The mean separation between each charge peak is calculated using the mean of each fit weighted by the uncertainty, (Section 6.1.1)
7. The electron gain is found by dividing the mean APD charge output by the charge of the electron (1.602×10^{-19} C)

6.1.1 Calculation of the gain with uncertainties

Using the output of TMinuit during step 6 above, the sigma of each Gaussian is used to estimate the uncertainty on the mean and is calculated as follows,

$$\sigma_m = \frac{\sigma_g}{\sqrt{N_g}} \quad (6.1)$$

where σ_m is the uncertainty on the mean σ_g is the sigma of the Gaussian fit, and N_g is the integrated number of events under charge spectrum with limits set to $\text{mean} \pm \sigma_g$.

The separation between all adjacent peaks is then calculated. Since the process is a subtraction of two numbers the uncertainty is calculated by adding the uncertainties in quadrature. Each peak separation measurement is then combined using the least squares method. The motivation for using this method is that the peak separation is the same measurement regardless of whether it is between 0 and 1 or or more APD triggers. The calculation of the mean and corresponding uncertainty is calculated as follows,

$$\check{\lambda} = \frac{\sum_{i=1}^N y_i / \sigma_i^2}{\sum_{j=1}^N 1 / \sigma_j^2} \quad (6.2)$$

$$\Delta \check{\lambda} = \sqrt{\frac{1}{\sum_{i=1}^N 1 / \sigma_i^2}} \quad (6.3)$$

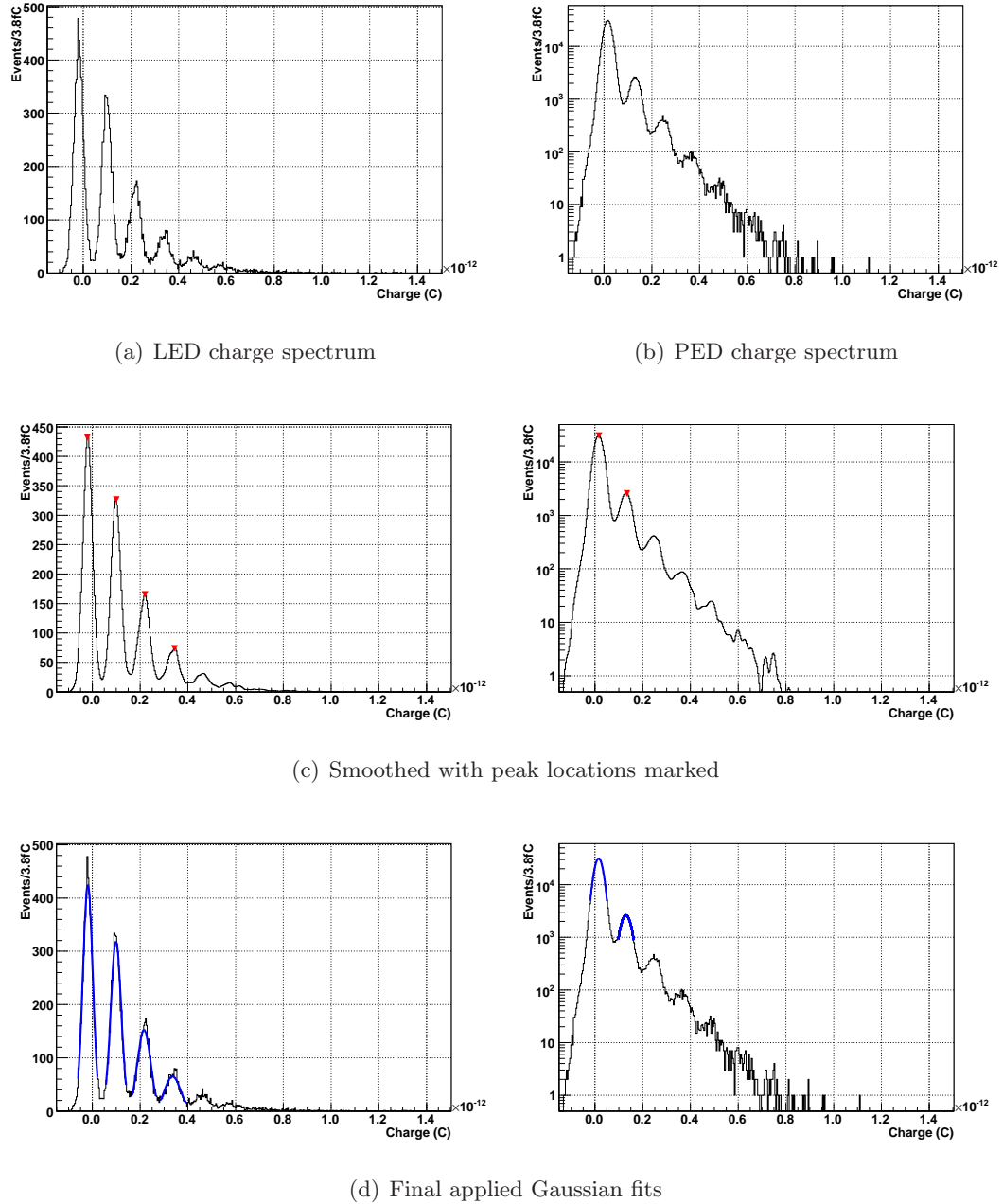


Figure 6.1: Example of peak finding and fitting procedure for LED and PED charge spectrum.

Additionally, the uncertainty in the charge calibration is included in quadrature as follows

$$\left(\frac{\Delta G_f}{G}\right)^2 = \left(\frac{\Delta G}{G}\right)^2 + \left(\frac{\Delta C}{C}\right)^2 \quad (6.4)$$

where ΔG_f is the final measurement uncertainty on the gain G and C is the Calibration value.

6.1.2 Example calculation

This example uses the spectrum as shown in Figure 6.1(a), including 0.8% uncertainty on the charge calibration in the final step producing Gain_f .

Peak finder estimation (C)		Least squares fit estimation (C)	
Peak 0	-0.21×10^{-13}	-0.189	$\pm 0.003 \times 10^{-13}$
$\Delta 0-1$	1.21×10^{-13}	1.172	$\pm 0.005 \times 10^{-13}$
Peak 1	1.00×10^{-13}	0.983	$\pm 0.004 \times 10^{-13}$
$\Delta 1-2$	1.21×10^{-13}	1.205	$\pm 0.007 \times 10^{-13}$
Peak 2	2.20×10^{-13}	2.188	$\pm 0.005 \times 10^{-13}$
$\Delta 2-3$	1.25×10^{-13}	1.192	$\pm 0.010 \times 10^{-13}$
Peak 3	3.45×10^{-13}	3.380	$\pm 0.009 \times 10^{-13}$
Mean Separation	1.22×10^{-13}	1.185	$\pm 0.003 \times 10^{-13}$
Gain	0.76×10^6	0.739	$\pm 0.002 \times 10^6$
Gain_f		0.739	$\pm 0.006 \times 10^6$

This shows that the systematic uncertainty on the charge calibration is a more dominant contribution to the total uncertainty of a typical gain measurement. This example also displays that the TSpectrum peak finder output can only be used as a simple gain estimation.

6.1.3 Experimental study

A bias scan was performed for each available device. The maximum and minimum bias is set to the voltage at which the single photoelectron peak is observable in a pedestal spectrum. At low bias the single photoelectron peak moves into the pedestal and cannot be observed. At high bias, a combination of dark count, crosstalk and afterpulsing reduces the single photoelectron resolution, causing the peaks to widen. Under high bias operation the position of each photoelectron peak in a spectrum becomes difficult to distinguish. Each charge spectrum is taken over a period of 2 minutes at a temperature of 22.0°C. The aim of the initial experiment is to establish over what range of voltage each GAMPD is

able to operate and to compare basic performance for each available device.

Analysis of the resulting charge spectra is performed as described above, and the gain extracted for each device.

Results and discussion

Figure 6.2 shows the resulting gain scans of the initial experimental study. It shows the low gain cut off of the HPK and SensL devices at approximately 5×10^5 . This cut off is a combination of integration of readout noise and the pulse width of a pixel trigger. The HPK and SensL pixel triggers are typically 90% contained within 100ns, thus a 200ns integration window is used in order to include crosstalk and afterpulses and to increase the probability of integrating a dark noise. The CPTA devices tested produce pulses with much smaller widths and are 90% contained within 50ns and thus a smaller integration window is required. Reducing the integration window improves the peak resolution and thus a gain lower than 5×10^5 is observable. The use of a smaller integration window and an LED light source for CPTA device 1710-015 is caused by a manufacturing problem with the device resulting in long recovery tails on the device output. This has been observed previously [87], the most likely cause being due to variation in quenching resistances between devices and or pixels [88]. The long recovery tail produced by this device resulted in poor single photoelectron peak resolution in pedestal spectrum and thus an LED is required to illuminate the device and produce a signal at a fixed time inside the integration window in order to gain good enough peak resolution for analysis.

All devices are observed to be linear gain with bias voltage over the range studied as expected from equation 5.4

6.1.4 APD triggers binning

Converting the x -axis of a charge spectrum into APD triggers provides a visual aid in determining the quality of the spectrum and the success of the gain extraction. After the above analysis is performed the location of the pedestal, the APD trigger peaks and the mean separation are known.

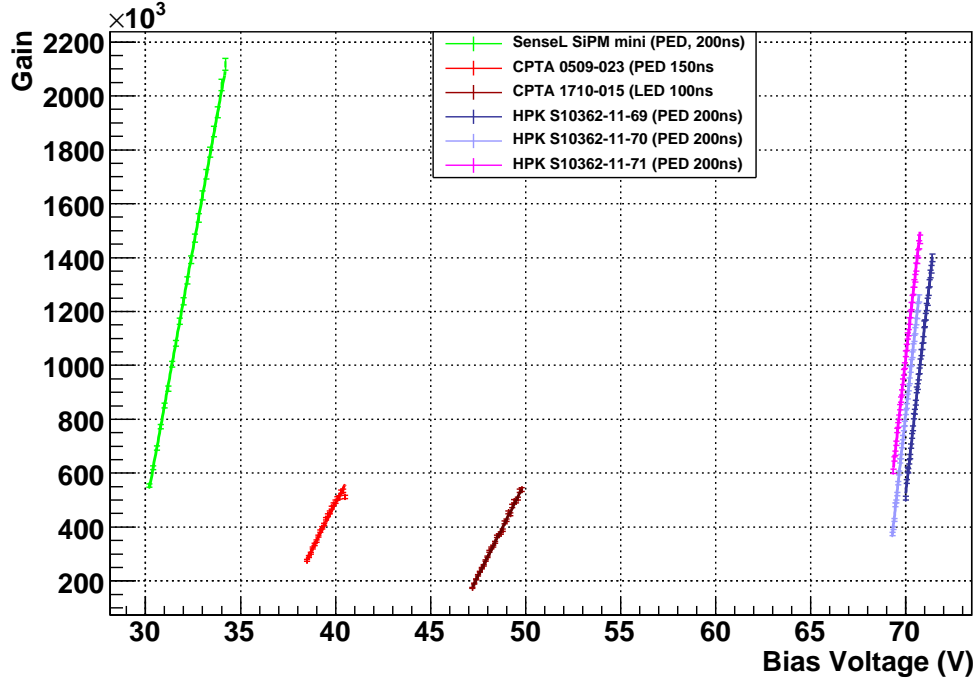


Figure 6.2: Gain scan for 6 test devices during initial GAMPD studies. Each device is listed in the legend with the run type and the integration window for reference.

In order to convert to APD trigger binning, the following equation applied to each x -axis bin,

$$N_{APD} = \frac{x_{bin-PED}}{Q_{APD}} \quad (6.5)$$

where, N_{APD} is the number of APDs triggered, PED is the location of the pedestal and Q_{APD} is the mean separation between APD triggers. The process will place the centre of each peak on a charge spectrum at the centre of an APD trigger bin.

The diagnostic property of this process arises from the variation of each peak around each APD trigger. If the alignment between APD trigger peaks and the x -axis is poor it indicates that a problem has occurred either during data taking, or in the first step of analysis.

The most typical causes of such misalignment is a poorly fitted APD trigger in the spectrum or charge truncation during data taking. Charge truncation is when charge is lost or not integrated. This is caused by using a integration gate that is too short, or by saturation of the oscilloscope ADC.

6.2 Breakdown voltage and APD capacitance

In order to extract the breakdown voltage (V_{bd}) and the APD capacitance a bias scan must be taken. One charge spectrum is produced per applied bias voltage (V_b) and gain calculation is performed as detailed above.

6.2.1 Breakdown voltage

From Equation 5.4 the gain is zero when $V_b = V_{bd}$, thus V_{bd} is found by plotting V_b against the gain and deducing the voltage at which gain is zero. This is performed by TMinuit applying a first order polynomial fit.

6.2.2 APD capacitance

By rearranging Equation 5.4 to make the APD capacitance the subject the following is obtained:

$$C = \frac{Ge}{V_b - V_{bd}} \quad (6.6)$$

it is shown that from a plot of gain against $V_b - V_{bd}$ (over-voltage) the capacitance and the gradient of the distribution found by applying a first order polynomial fit. The gradient is multiplied by the electron charge to give the capacitance in Farads.

6.2.3 Experimental study

The data presented in section 6.1.3 is used with the analysis discussed above to calculate the breakdown voltage of each device. The breakdown is used to produce a gain against over-voltage plot. The APD capacitance of each device is then calculated using the resulting plot.

Results and discussion

The resultant over-voltage plot is shown in Figure 6.3. It shows more clearly the full range of voltages required to operate each GAMPD through its respective range of operating

Device		V_b at 22.0°C	Capacitance (fF)
HPK	S10362-11-50C #69	69.148 ± 0.005	99.9 ± 0.7
	S10362-11-50C #70	68.700 ± 0.005	101.7 ± 0.6
	S10362-11-50C #71	68.334 ± 0.005	99.8 ± 0.7
SensL	SPMMini	28.883 ± 0.003	62.3 ± 0.4
CPTA	1710-015	45.594 ± 0.003	22.4 ± 0.1
CPTA	0509-023	36.702 ± 0.009	22.2 ± 0.3

Table 6.1: Breakdown voltage and capacitance of 6 sample devices during initial testing at 22.0°C

gain. Table 6.1 gives the breakdown voltage and the APD capacitance of each tested device with statistical uncertainties only. The extracted APD capacitance of each device provide an insight into the typical operating range gain of each device, since the major factor limiting the gain is capacitance. It is shown that the HPK and SensL devices are constructed with higher capacitance APDs and thus in general operate at a higher gain than the CPTA devices. The plot also displays how despite the variation in breakdown voltage for the HPK and CPTA samples, an identical pixel structure is used for each. Although a low number of devices are examined (3 in the case of HPK and 2 in the case of CPTA) APD capacitance is observed to be well controlled in the production process

In the case of the HPK device samples, each device has a successive device number and are from the same production batch. This is supported by fact that the values of the extracted breakdown voltages lie $<1V$ from each other. This is caused by doping fluctuations in the surface of the device that sets the absolute breakdown voltage.

In the case of the CPTA samples, the devices are from different development stages and thus the large difference in breakdown voltage should not be taken as a reference to the reproducibility and manufacturing of the devices.

6.3 Dark count rate

Dark count rate is calculated using PED spectrum only, using a counting method. The method calculates the rate of events occurring at a chosen charge threshold. The operating

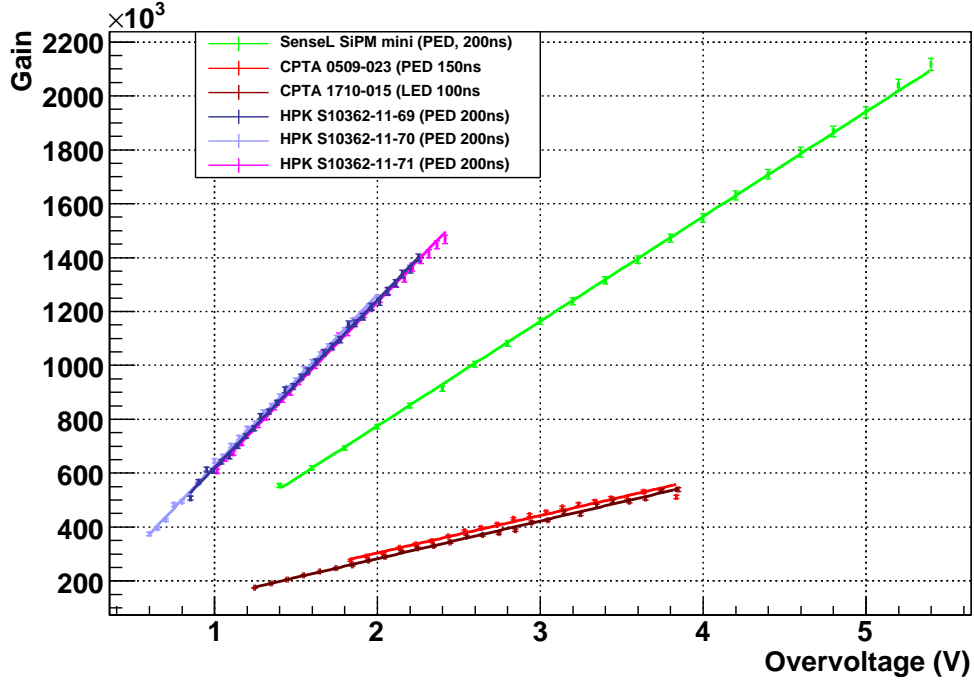
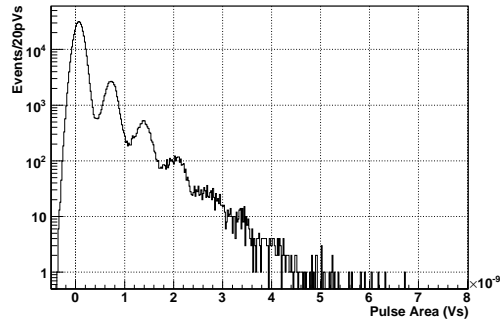


Figure 6.3: Gain against over-voltage plot for 6 test devices.

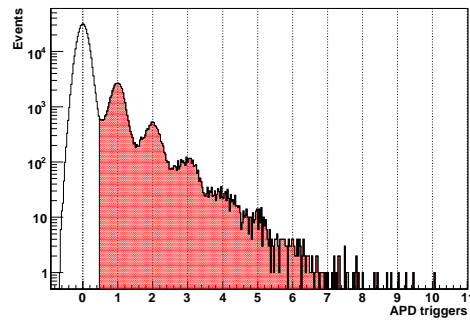
gain of the GAMPD is first calculated as detailed above. This provides an accurate location of the pedestal and the neighbouring single APD trigger peak. The x -axis of the PED spectrum is then converted into number of APD triggers. Using the length of the integration gate (τ) the dark count rate (R) can be calculated by considering the fraction of events above a set threshold in a PED spectrum as follows,

$$R_x(\text{Hz}) = \frac{N_x}{\tau(s)N_T} \quad (6.7)$$

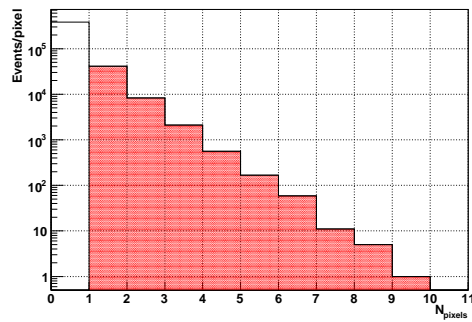
where N_x is the number of events greater than threshold x , τ is the integration gate and N_T is the total number of events in the spectrum. The threshold can take any value although commonly 0.5 and 1.5 APD triggers is chosen to compare GAMPDs. Figure 6.4 gives a sample of typical plots produced and used to extract the dark count rate using the above equation. Figure 6.4(d) shows how the dark count rate varies as a function of threshold, giving an exponential decay of the dark count rate at increasing threshold. Such a plot is important when considering triggering and coincidences while using GAMPDs.



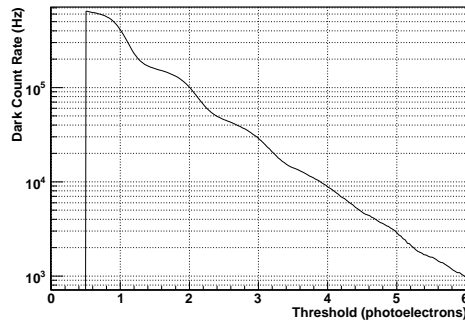
(a) PED pulse area spectrum



(b) PED pulse area spectrum in Integer bins with counts above 0.5pe threshold shown



(c) PED spectrum in Integer bins



(d) Dark rate threshold scan

Figure 6.4: Example of dark count rate extraction using a pedestal spectrum (a), (b) shows the pedestal spectrum rebinned in terms of photoelectrons and (c) in integer photoelectron bin, (d) shows the result of a threshold scan using equation 6.7

6.3.1 Pedestal spectrum simulation

If the pixels of a GAMPD are assumed to be completely independent of each other, a pedestal spectrum will predominantly contain pedestal events where no charge was integrated by the DAQ, with a comparatively smaller distribution of events containing one or more pixel fires to thermal triggering. In such a device, the only events in this spectrum would be due to random coincidence between one or more thermal pixel fires and the integration window. Due to the use of a narrow integration gate, of typically 200ns, the probability of two or more pixels firing due to thermal excitation within 200ns is very low and such the events of the distribution will be heavily weighted between bins containing zero and one pixel fire.

It is possible to simulate the expected pixel fire distribution of a GAMPD based on the above assumption that each pixel is independent in order to establish if the model can reproduce the observations of real data, and conclude if the model is correct. In this simulation a pedestal spectrum is taken for a test GAMPD and the dark count rate extracted using the analysis described above. The dark count rate at 0.5 pe threshold $R_{0.5}$ (from Equation 6.7) is then used to estimate the probability of firing a single pixel P_d of the GAMPD in each integration window as follows,

$$P_d = \frac{R_{0.5}(Hz)\tau(s)}{N_{pixels}} \quad (6.8)$$

The simulation is written using the ROOT framework and C. For each event of the simulation, a random number is generated for each pixel, if it is less than or equal to P_d the pixel is fired due to thermal excitation and is counted. This process is repeated for the same number of events as in the real pedestal spectrum.

The resultant distribution is shown superimposed on top the sample pedestal spectrum in figure 6.5. It is clear to see that the simulated distribution does not match data. There is an excess of events in the single pixel fire bin and a deficit in all subsequent bins. Such differences between the above assumptions and data is expected if the true behavior of a typical GAMPD are considered. The simulation is thus modified in order to introduce other known sources of noise which weight the mean of the distribution to high numbers of pixel fires.

Thermal pixel fires

For this simulation the shape of the array is important as knowledge of the physical location of the pixels with respect to each other is vital for producing an accurate simulation of crosstalk, for example, a pixel firing on the edge of an array has less influence on the total crosstalk in the device than one firing in the array centre. In order to initialise the simulation, the state of each pixel of the array is determined by the process described in Section 6.3.1. However the window considered is changed to 40 ns in order to include a more complex afterpulse model as discussed below. In the array, pixels that fire due to thermal excitation numbered as 1.

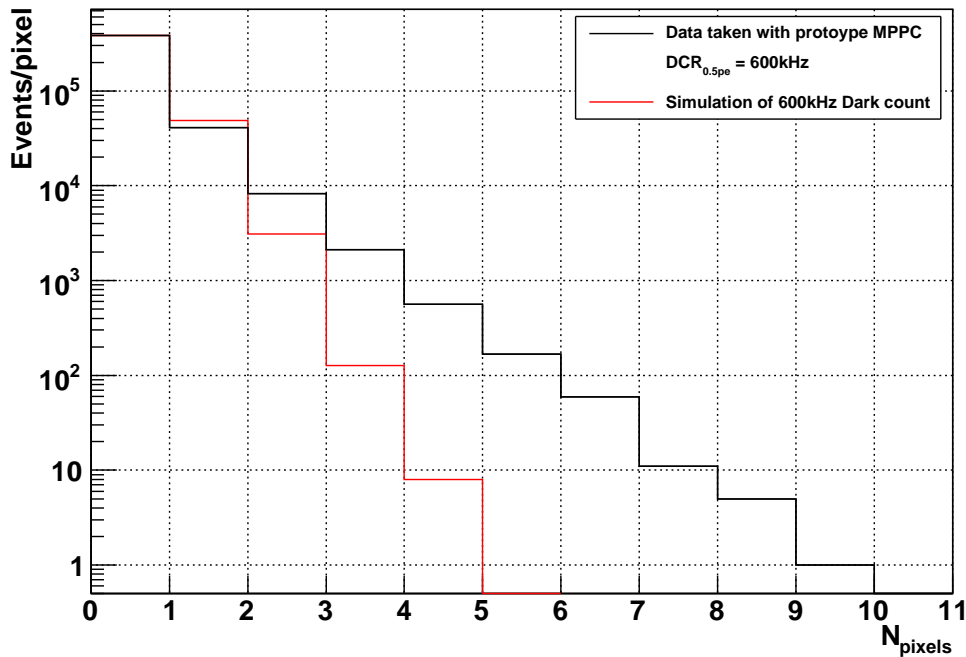


Figure 6.5: Pedestal data taken with a prototype MPPC with a dark count rate of 600 kHz. Red shows the distribution of number of pixel fires when assuming events only occur due to dark count.

Crosstalk

Each pixel that fires in a GAMPD may cause optical crosstalk with neighbouring pixels causing them in turn to fire. This is true for pixel fires of any origin in the array. In the simulation the range of crosstalk is limited to nearest neighbours and next nearest neighbours in a circle around the fired pixel. Nearest neighbours have a higher probability (P_{ct}) of being fired and follow a $1/r^2$ fall off. For each pixel within the affected region a probability test is performed and any pixels that pass have their state changed to ‘fired’. Any pixel fired due to crosstalk has the same process repeated on it allowing for crosstalk to cause further crosstalk. Pixels triggering due to crosstalk are numbered 2 and 3 for nearest and next nearest neighbour, and 4 and 5 for crosstalk causing crosstalk, nearest and next nearest neighbour. This process is shown diagrammatically below in Figure 6.6.

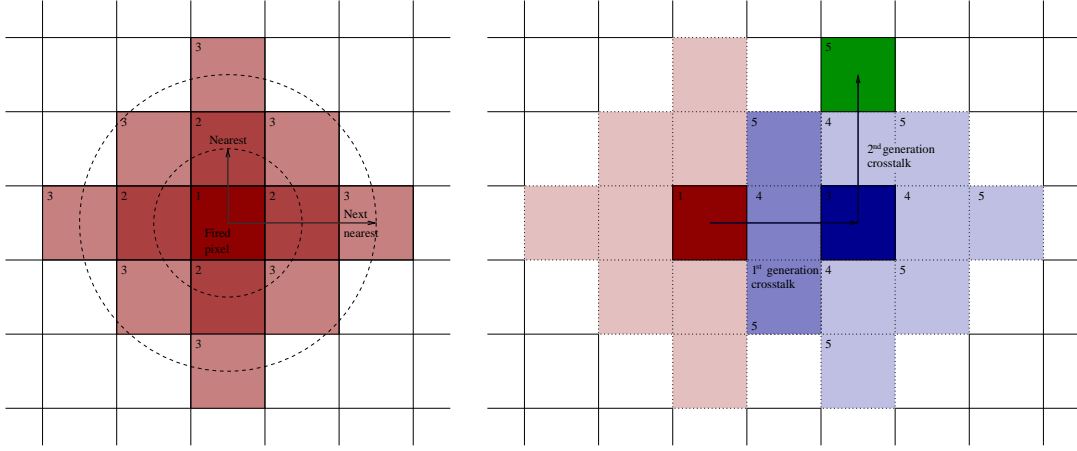


Figure 6.6: Crosstalk generation numbering scheme for use in simulation

Afterpulsing

In order to implement afterpulses in the device, the simulation must be split into smaller segments in time. For the sample pedestal spectrum, the integration gate is set to 200 ns, and the length of a pulse from the device is typically 40 ns in duration, so the 200 ns window is split into 5 sequential sub-windows plus one pre-window. The probability of a triggered pixel producing an afterpulse in a subsequent sub-window is calculated using the following expression,

$$P_{ap} = S e^{-t_{age}/t_{ap}} \quad (6.9)$$

Where S is a scaling factor, t_{ap} is the trap decay time and t_{age} is the age of the fired pixel as discussed below. Both t_{window} and t_{ap} are in units of sub-window number. The form of an exponential decay is to account for the decay like behaviour of trapped carriers [72].

The purpose of the pre-window is to account for dark count that occurs before the integration window, as there is a finite probability these will produce afterpulses within the 5 preceding sub-windows. In order to produce more realistic dark count in the device several pre-windows should be generated before the defined integration sub-windows, however, only a single pre-window has been used to reduce the computing time required.

In the pre-window, each pixel is tested against the probability of a thermal trigger. Once all pixels in the array have been considered, each surrounding pixel is tested for crosstalk. All fired pixels are then inserted into a afterpulse map and given an age, t_{ap} , of 1. In the

next sub-window each pixel fired in the previous sub-window are tested for afterpulsing and any that fire given a value of 1. The process of thermal pixel triggering is then performed over the whole array and the process repeated. All events that occur due to thermal pixel firing, crosstalk and afterpulses are counted for the 5 sub windows and placed into a histogram. This process is repeated N times in order to generate enough statistics to match sample data.

Parameter selection

In order to produce a PED spectrum which fits the experimental data presented, a 3D grid search is performed. In this search a simulation is performed for ranges of all the 3 input parameters P_{ct} , S and t_{ap} . At each position on the grid the a χ^2 test is performed, comparing the simulated pedestal spectrum with real data. This is shown in Figure 6.7, with the location of the lowest observed χ^2 shown by the black lines.

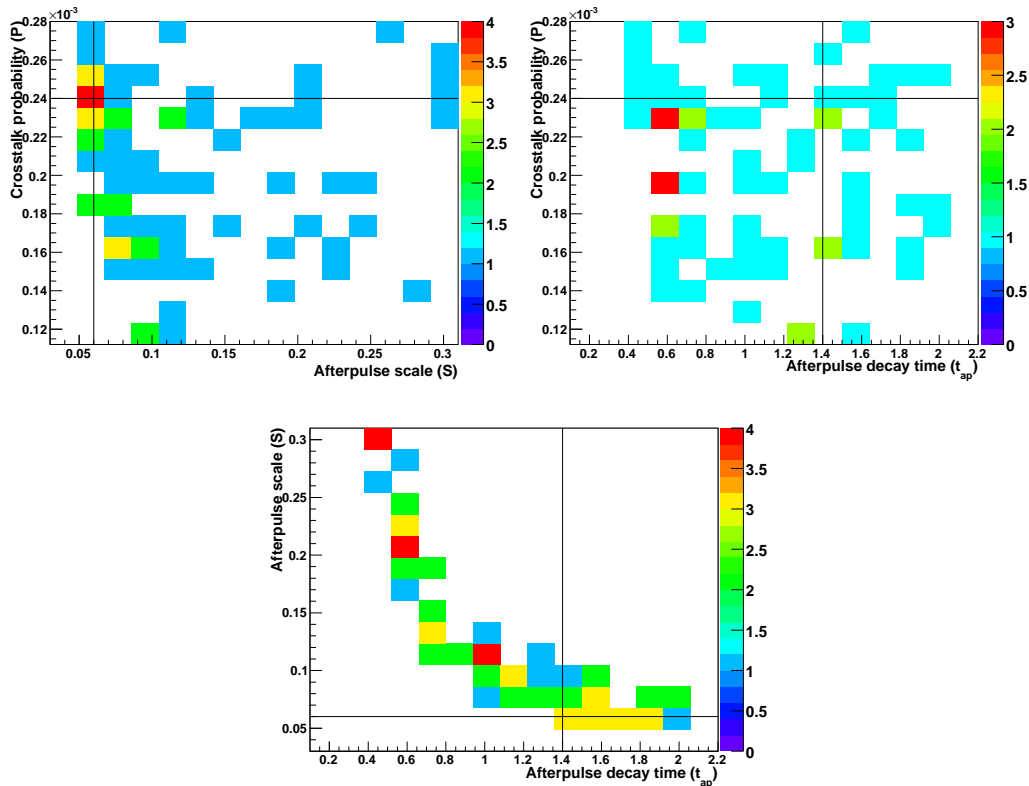


Figure 6.7: Grid search results showing the 75 parameters with lowest value χ^2 over a 15^3 cube parameter space. The black lines show the location of the lowest χ^2

This shows how for this model crosstalk and afterpulsing mechanisms are correlated and are difficult to separate, as a low χ^2 can be achieved for a particular crosstalk probability by adjusting the afterpulse decay profile. Without measuring one of these effects absolutely it is impossible to estimate the correct values using the simulation.

Despite the simplicity of the model, Figure 6.8 shows that the output of the simulation with the parameters shown in Figure 6.7. is able to match real experimental data closely. The simulation is normalised in total number of events and dark count rate. It shows the different contributions from multiple coincident dark count pixel fires, afterpulses and crosstalk.

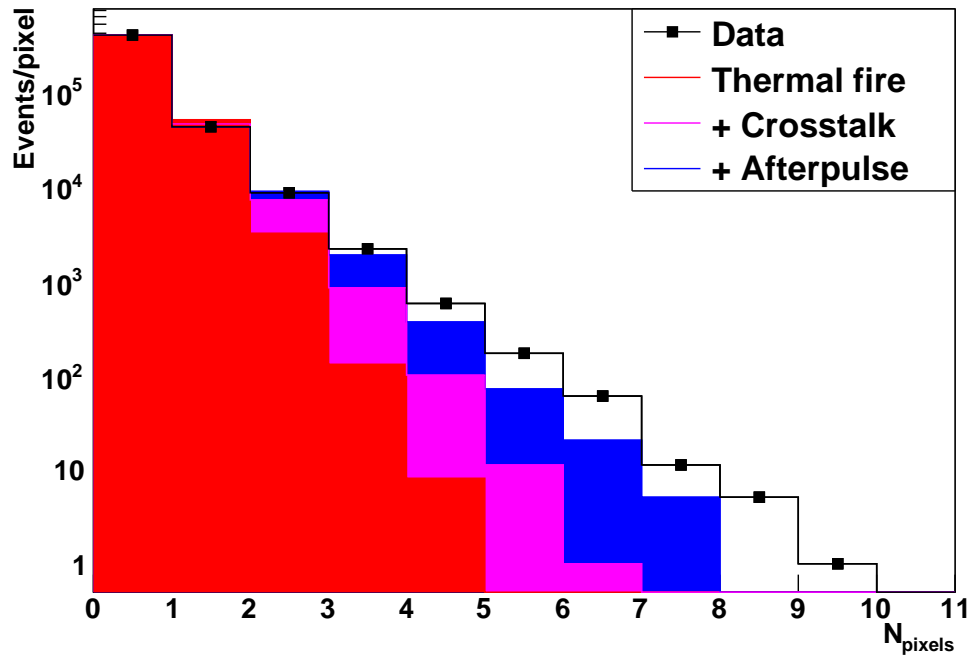


Figure 6.8: Stack plot of the final simulation using parameters shown in Figure 6.7 achieving $\chi^2/\text{ndf} = 23.9$.

6.3.2 Simulation result and discussion

The simulation discussed above and the resultant charge spectrum shows clearly that the shape of a pedestal spectrum can only be explained with the inclusion of effects such as crosstalk and afterpulsing which act to add extra charge. Without these effects, the rate of

multiple thermal trigger coincidences is not high enough to match observed experimental data. However, due to the correlation between crosstalk and afterpulsing it is difficult to give an estimation of each parameter directly from experimental data. The combination of these effects can be estimated by the ratio of events greater than 2 pixel fires to the events greater than 1 pixel fire in pedestal data.

$$P_{ap+ct} = \frac{\sum N_{>0.5pe}}{\sum N_{>1.5pe}} \quad (6.10)$$

The presence of crosstalk and afterpulse can adversely effect device performance, as high rates of afterpulsing can cause pile up if the input rate of photons is high, it is however possible to reduce this effect by externally altering the RC component of the device such that it recovers on a time scale similar to afterpulsing such that carriers released from traps before the junction have been quenched and do not cause delayed avalanches.

6.3.3 Dark count rate, crosstalk and afterpulse study

Each device listed in Table 5.10.4 with the exception of the CPTA device 1710-015 has undergone detailed pedestal scans in order to allow estimation of the dark count rate and total crosstalk+afterpulsing fraction by the methods described above. The experimental procedure and setup is described in Section 6.1.3.

Results and discussion

Figures 6.9(a) and 6.9(b) show all extracted dark count rates and total crosstalk+afterpulse fraction for the devices under study. It is clear that, for the samples available the CPTA device has a greater dark count rate and suffers from higher levels of crosstalk and afterpulsing than all others, through a smaller range of gain.

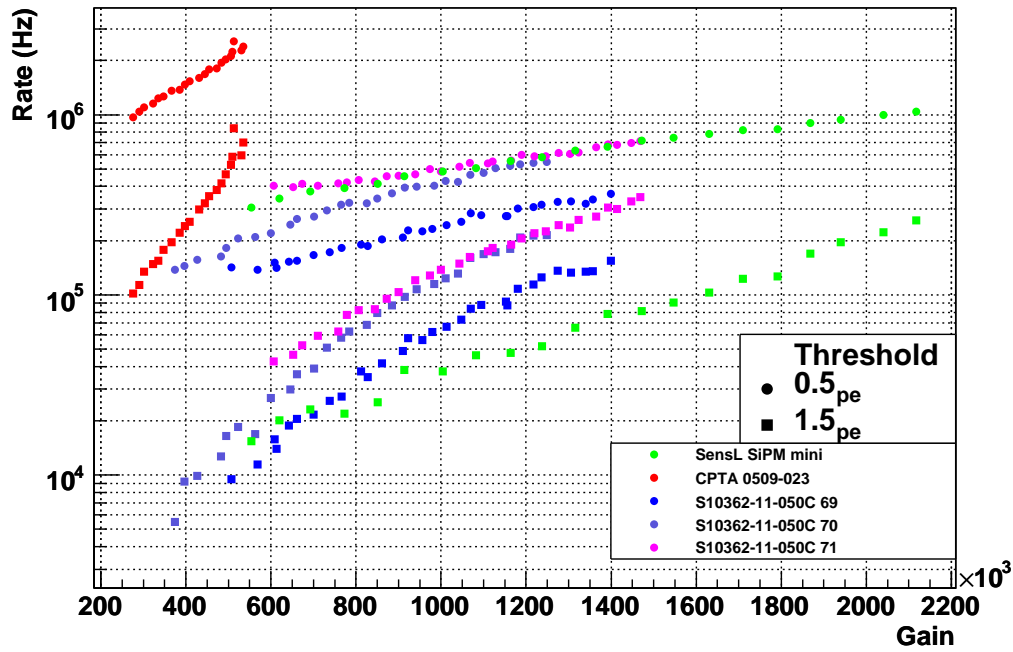
The devices obtained from HPK and SensL show much reduced dark rates and total crosstalk + afterpulse fraction over a higher range and absolute gain. Although there are only a low number of devices presented, an interesting feature of this plot is the spread in dark rates for the 3 HPK samples, and in the case of sample 70 the difference in gradient. This reflects the difficulty the manufacturer has trying to control the dark count rate on a device to device basis, even on the same silicon wafer, however, despite the spread,

Figure 6.9(b) shows that all samples have similar total crosstalk + afterpulse fraction. Since crosstalk is heavily dependant upon the physical structure of the pixels and the array and afterpulsing is dependant upon impurities and imperfections in the depletion region, HPK appear have control over these features and are able to produce devices with APDs that under bias produce predominantly identical depletion regions. It would suggest that the variation of dark count rate points to reproducibility of the areas around the depletion region and the surface of the APDs. By comparing these plots with data presented in Table 6.1 it is also observed that the dark count rate is generally higher for the HPK devices with lower breakdown voltage. This fact also supports the above statement, since for an APD the surface layers are often given a passive coating by manufacturers to allow control of the breakdown voltage (Section 5.1), suggesting that in HPK devices, the absolute breakdown voltage level could be a general indication of the expected dark count rate. While APD capacitance gives a good measure of how noisy an APD will be, all HPK devices are observed to have similar pixel capacitance and thus variations of the capacitance cannot account for the variation in dark count rate observed. Without more samples however this is extremely speculative.

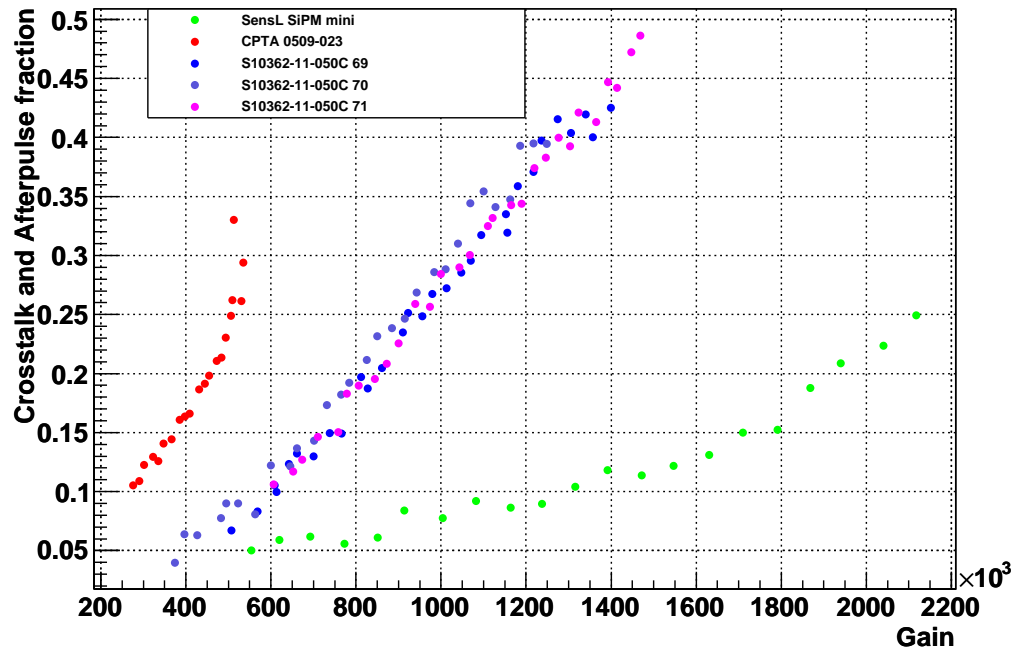
The last device shown in Figures 6.9(a) and 6.9(b) is the SensL sample. Due to the difference in device structure, this device has a dark count rate of similar order of magnitude to the HPK devices, however it operates over twice the operating gain with a lower rate of crosstalk and afterpulsing. The device also has a much larger number of pixels, thus the suppression of dark rate possibly reflects the smaller pixel pitch and capacitance used as the volume susceptible to thermal excitation is reduced. Without detailed doping profiles it is difficult to attribute this difference, nor can a spread in the dark count be compared to the HPK devices. However it is clear that the SensL device is less susceptible to crosstalk and afterpulse, thus is likely due to the use of aluminum coated trenches between APDs.

6.4 Electronics and the selection of GAMPD for use in T2K

The selection of a GAMPD from the tested samples is based upon performance, development maturity and compatibility with the developed ECal electronics. The electronics to be used in ND280 is based upon a Trigger Pipeline + Timing ASIC chip (TriP-T). Due to space constraints the electronics used to read out the GAMPDs has to occupy as



(a) Dark count rate



(b) Crosstalk + afterpulse fraction

Figure 6.9: Dark count rate and crosstalk + afterpulse fraction for initial test devices

little physical space as possible. Each Trip-T has 32 channels, each containing an fixed gain integrating pre-amplifier and an adjustable amplifier feeding an ADC. However, the dynamic range of the Trip-T will not cover the expected operating range of tested GAMPDs, and as such, the electronics have been designed to overcome this by splitting the output from each GAMPD capacitively into two channels; low and high gain. This allows a single Trip-T to readout 16 GAMPDs simultaneously. The high gain channel allows a very small dynamic range measurement of the charge, making it possible to perform a very high resolution charge integration at a low number of photoelectrons (p.e.). The low gain channel receives a comparatively smaller amount of charge from the GAMPD and so the channel is able to observe and measure a larger range of charges.

4 Trip-Ts are used for each Trip-T front end board (TFB) allowing a single board to readout 64 GAMPDs. Each board uses a single high voltage input and has 64 programmable voltage trims allowing the independent setting of each GAMPD to a desired operating voltage. However the trim range is limited to 5 V and so any GAMPD model selected must be manufactured to have a breakdown voltage range less than the trim. A small operating voltage range is also required as it will ensure that GAMPDs may be operated through a range of temperatures and allow the trim to normalise the gain. Each Trip-T is capable of applying a discrimination threshold to 16 channels, for each GAMPD the threshold will be applied to the high gain channel. The expected level will be 5 p.e. If this threshold is passed the event will be timestamped and the channel readout, thus it is important that the threshold is not passed artificially due to dark noise. Timing information will be used to reconstruct events in ND280 and, as such, it is important that dark noise of a GAMPD is as low as possible. The reason for this requirement is compounded by the programmable integration time of each Trip-T, which can be set to as short as 50 ns up to $\sim \mu\text{s}$. The integration length will be of the order ~ 520 ns. As observed by an oscilloscope performing charge integration, a longer integration window introduces more electrostatic noise, which in turn reduces single photoelectron peak resolution. It also follows that a longer integration window allows for more dark count events to be integrated in any given sample. This leads to an estimate that the highest level of dark noise should be <1 MHz.

The T2K specifications placed upon candidate GAMPDs before selection is summarised in the following table.

Parameter	Value
Area	$\geq 1 \times 1 \text{ mm}$
Gain	$4 - 8 \times 10^5$
Dark Rate	$< 1 \text{ MHz}$
Crosstalk + Afterpulse fraction	$< 20\%$
PDE	$> 15\%$ at operating votage
Dynamic Range	$< 350 \text{ pe}$
ΔV_{op}	$< 5 \text{ V}$
Packaging	non-magnetic
Price per unit	$\leq \$20$

Table 6.2: Specifications proposed for photosensors for the ND280 Electromagnetic Calorimeter. The numbers are based upon typical device specifications in 2005 [1] and were updated summer 2007 reflecting finalisation of electronics and the experience of groups working with GAMPDs

6.4.1 CPTA — MRS APD

By summer 2007 the MRS APD existed in two forms, the 1710 model as tested during this study and a later developed model known as the model 23. As observed above, the maximum operating gain of the 1710 device is $< 0.6 \times 10^6$. The dark count rate observed in MRS APDs is also typically in excess of 1 MHz, with a crosstalk+afterpulse fraction of 0.25 at a gain of 0.5×10^6 and is the highest of all GAMPDs. However the device is known to suffer from pulse shape problems in the form of a long recovery tail as discussed in Section 6.1.3; This was considered problematic for the T2K electronics due to signal resolution degradation, this effect has been observed with the sample under initial study, the single photoelectron resolution is degraded such that it is difficult to make measurements of gain and dark count rate from pedestal spectra. Over the T2K collaboration approximately 300 devices have been examined, and the results and properties observed during is initial study are in good agreement. The MRS APD was thus rejected for use with the T2K experiment.

6.4.2 SensL — SPMMini

Early sample devices from SensL were received early in 2007, thus the device was in a very early stage of development. Although observed to have impressive performance in regard to the gain ($<2.0 \times 10^6$), dark count rate (~ 1 MHz) and crosstalk+afterpulse fraction, extensive testing could not be performed on many samples in order to deduce the quality and reproducibility of the device. This device shows great promise and SensL appear to be continuing to development it for future experiments and applications. The device has undergone recent study and consideration for use in liquid argon detectors to detect scintillation light [89]. However it was decided that the maturity of the device along with its late submission for consideration are a disadvantage to T2K and thus was rejected for use with T2K.

6.4.3 HPK — MPPC

Early HPK MPPC samples obtained for study show consistency with regard to gain ($<1.3 \times 10^6$) and crosstalk+afterpulse fractions, though appear to show discrepancy in the levels of dark count rate. It is not clear if such a variation is observed over all GAMPDs or are restricted to MPPCs only, however the MPPC are not observed to have dark count rates higher than 1 MHz. Based on positive results during initial testing at Sheffield and the rest of the UK photosensor group and by the photosensor groups in Kyoto and INR the MPPC was selected for use in the T2K experiment.

Shortly after selection HPK announced the final production model MPPC for T2K would use 667 $50\mu\text{m}$ pitch pixels arranged on an 1.3×1.3 mm array. It is a custom device with serial number S10362-13-050C. A device of an area that is larger than that of the wavelength shifting fibre used in T2K will allow more efficient light collection, since light is emitted from the tip in a cone rather than being emitted parallel to the axis. However, such a design is not without disadvantages, since the increase in the number of pixels will cause an increase in the absolute dark count rate of the device.

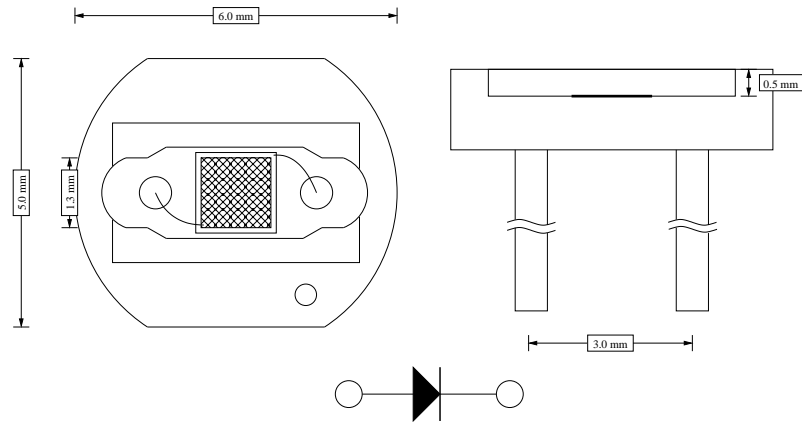
Despite the experience gathered using the S10362-11-050 model MPPC, all T2K devices will undergo extensive testing as part of Quality Assurance (QA) before being accepted for use in each ND280 sub-detector.

Packaging and ECal connector

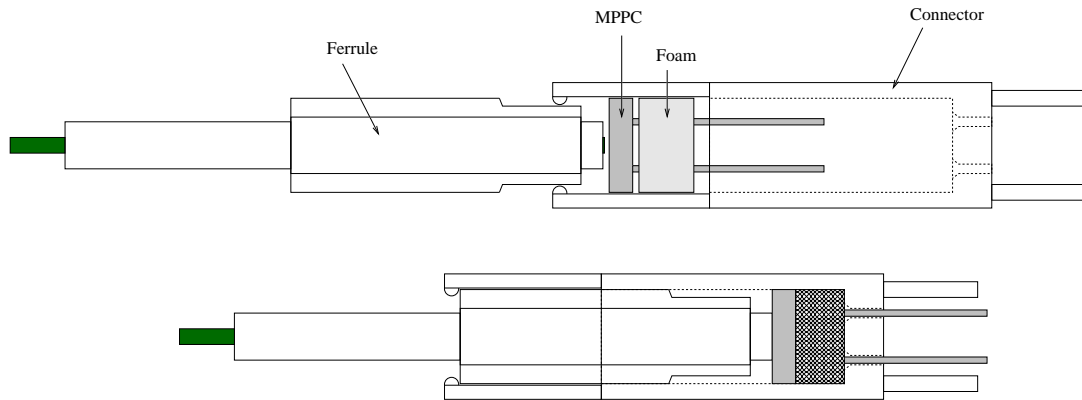
The MPPC is housed in a ceramic packaging which has two circular edges and two horizontal edges as shown in Figure 6.10 (a). The diameter of the circular section is 6 mm and the horizontal edges are 5 mm. This means the device can be securely positioned in an experimental setup with fixed rotation. The MPPC is positioned in a central cavity approximately 500 μm deep where it is wire bonded to two leads that extend from the rear of the device. To protect the MPPC and aid optical connection with a fibre the cavity is filled with clear epoxy. The fill level of the epoxy can vary between devices by up to 200 μm and forms a concave surface when under-filled. The mean depth of the MPPC under the epoxy layer is 400 μm . Figure 6.10 (b) shows the connector designed for optically coupling a length of Y-11 fibre to the MPPC. It is composed of a ferrule, sponge and an outer connector. When the connector is in its final position, the sponge provides a small force to push the MPPC against the fibre, ensuring contact between the fibre and epoxy.

MPPC Breakdown voltage temperature dependence

The observed operating voltage range of an MPPC is <2 V, which is inside of the <5 V specification. In order to fully satisfy the specification, a temperature scan is performed in order to deduce the breakdown voltage dependence on the temperature. A T2K 1.3 x 1.3 mm production MPPC has been used to study this effect. The device was cooled to 22.0°C and allowed to stabilise for 15 minutes, then a bias scan was performed as described previously. Once complete the temperature was raised in steps of 0.5°C and bias scans performed until reaching 25°C. For each spectra, the gain is extracted and plotted against bias voltage and temperature to produce Figure 6.11. If the breakdown voltage at each temperature is extracted, Figure 6.12 is generated. A linear fit to this plot reveals a MPPC breakdown voltage temperature dependence of 62 ± 1 V/°C. In order to cause a 2 V shift in the breakdown voltage a temperature change of 32°C would be required. Such temperature variations are not expected inside ND280.



(a) Hamamatsu S10362-13-050C MPPC Packaging design [65]



(b) ECal connector design

Figure 6.10: (a) Hamamatsu S10362-13-050C MPPC Packaging design, (b) Connector designed for use in the T2K Ecal to connect an MPPC to a length of Y-11 fibre.

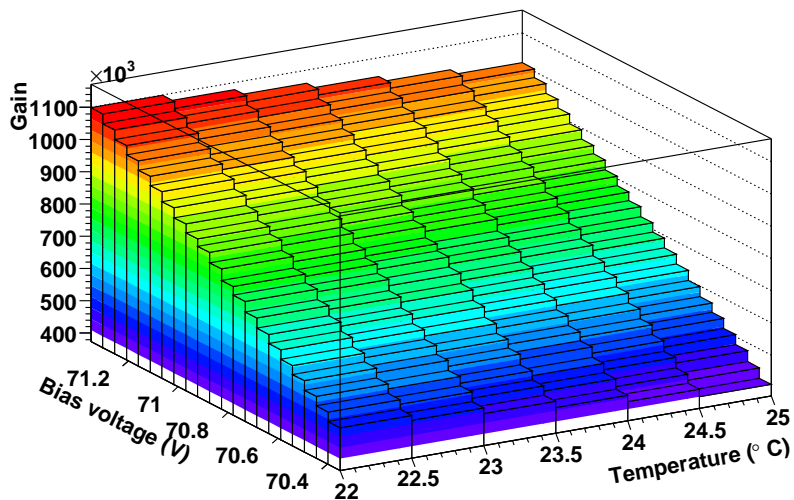


Figure 6.11: Temperature Scan of a T2K 1.3 x 1.3 mm ECal production MPPC

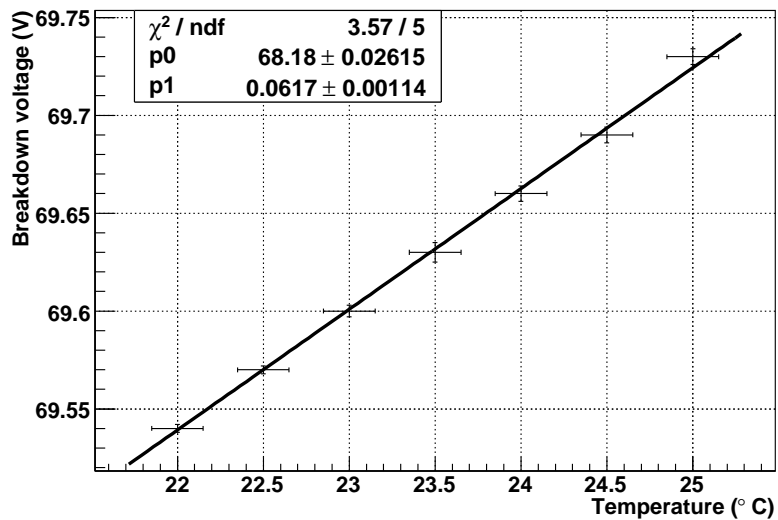


Figure 6.12: Breakdown voltage temperature dependence of a T2K 1.3 x 1.3 mm ECal production MPPC.

Chapter 7

Golden MPPC for ECal QA

The electromagnetic calorimeter of ND280 will employ approximately 22,000 MPPCs to detect photons that exit wavelength shifting fibres. Before MPPCs can be installed into each ECal module it is necessary to perform QA on each in order to determine key parameters, such as breakdown voltage, gain, dark count rate and photon detection efficiency (PDE). Measuring the PDE of an MPPC requires careful planning and systematic experimental procedures. The measurement of the PDE using an LED and a sample of wavelength shifting fibre are discussed in detail during this chapter. In order to allow the measurement of the PDE for a large number of MPPCs during the QA procedure several very well calibrated ‘Golden’ MPPCs are used as reference devices whose PDE is well known.

The measurement of PDE requires modification of the experimental setup given in Section 5.9 to include apparatus to accurately control the total intensity and the pulse profile of the LED light source. Illumination of the MPPC or another target such as a length of wavelength shifting fibre must be physically stable and reproducible. In the case of measuring the PDE when using a length of wavelength shifting fibre the setup must also be as close to real ND280 conditions as possible. This requires the use of ECal connectors for coupling the MPPC to wavelength shifting fibres.

It is also important to account for a number of experimental artefacts when measuring the PDE, the most important of these is the acceptance of the MPPC in comparison to the calibration device. The expected acceptance of the MPPC to an LED flash and also

to the photons leaving the tip of a fibre are considered in detail.

7.1 The experimental setup

The experimental setup has two configurations; using a calibrated LED flash or a small length of fibre. In both configurations a box with a 50 x 50 mm window is placed over the LED and a diffuser placed over the window. Directly in front of this a filter holder is placed into which neutral density filters can be added. The purpose of this arrangement is to ensure only photons that have passed through the filter are projected into the dark box towards the MPPC or other photosensor. For each configuration a Newport optical power meter is used to calibrate the light source, and will be discussed in more detail in the following section. The vital difference between each configuration is the collection and calibration of photons emitted by the LED.

When measuring the PDE using the photons produced by the LED directly, the MPPC is held by a connector providing physical stability and a thermal connection to a vertical cooling plate. The cooling apparatus is positioned on an optical rail allowing it to be aligned with the LED. When measuring the PDE using photons emanating from the tip of a length of WLS fibre, further apparatus is required. A screen is constructed out of black flock, this material ensures minimal reflection of photons that hit it. In the centre of the screen a hole is made and a length of WLS fibre is passed through. The fibre is then looped and connected to the screen such that it is held secure at the hole and the tip. The remaining free end of the fibre is then glued into an ECal connector ferrule.

The ECal connector consists of 3 parts, the ferrule, a sponge and the housing (Figure 6.10). The terminals of the MPPC are passed through the sponge, and the MPPC is then pushed into the housing until the terminals protrude through its base. When the ferrule is pushed into the housing it clips into place, the sponge applies pressure between the MPPC and the tip of the fibre. As the epoxy coating of the MPPC is soft, this pressure forms a good optical connection between the MPPC and fibre without the use of optical coupling grease. However, due to the use of plastic components, no direct thermal connection with the MPPC can be achieved. In order to provide temperature control of the MPPC two aluminium plates with semi-circular cut outs were constructed. The ECal connector is

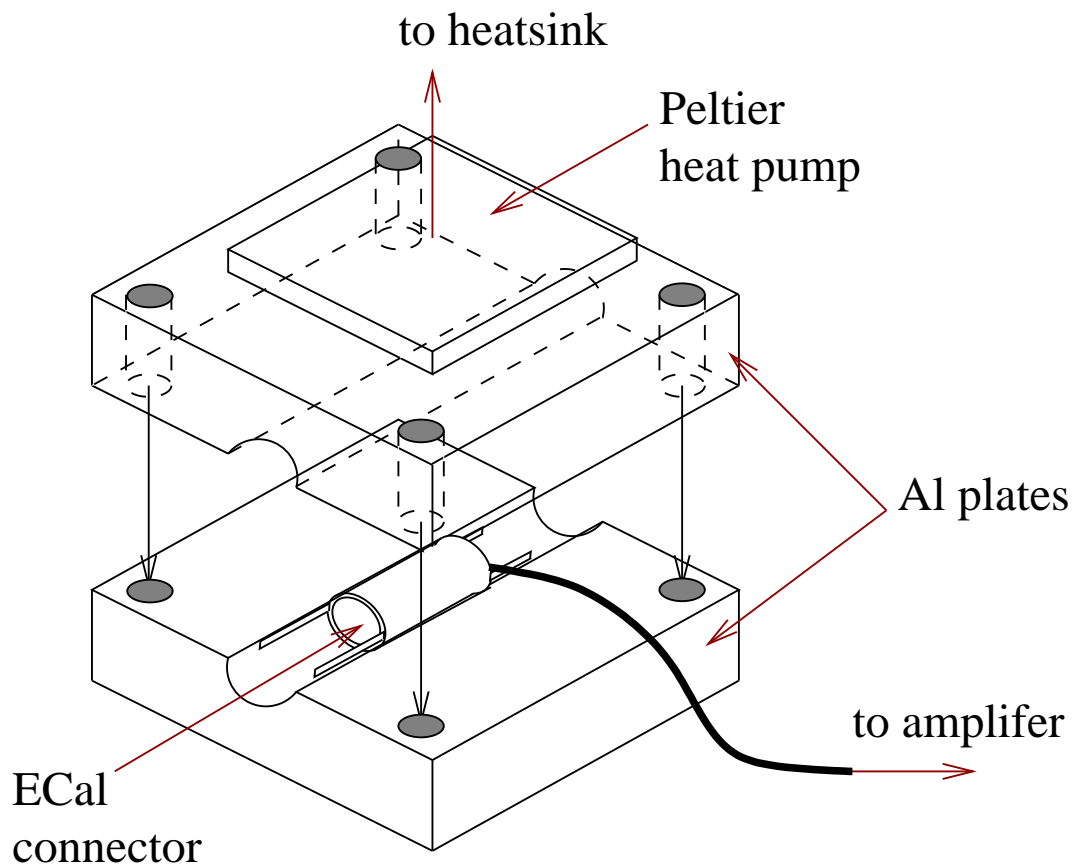


Figure 7.1: Temperature control stage for use with T2K ECal connector

then placed into the cutout on the bottom plate and then covered by the top. Thermal paste is used between the two plates to aid heat transfer between the two. This setup is shown in Figure 7.1. The purpose of this arrangement is to completely surround the ECal connector to cool the plastic and the surrounding air with the aim to control the temperature of the MPPC inside. In order to monitor the temperature of the MPPC a thermocouple is attached to one of its terminals. The temperature stability of this setup was found to be to within $\pm 0.3^\circ\text{C}$ from the result of the previous dark count rate systematic study (Section 7.2)

The LED used for all PDE measurements had a cleaved focussing lens. The reason for this is to reduce the need for accurate alignment of the equipment by producing an isotropic pulse of photons. How the focussing of the LED would affect the acceptance between the different photosensors used is given in Section 7.3.2. Despite using a very diffuse source the equipment is aligned by applying a small aperture the Newport optical power meter

and taking measurements over a range of heights through the LED pulse, and LED angles to the optical rail. The angle and height that produces the highest power measurement in the optical power meter is then used for all further measurements.

7.2 Temperature and light yield stability

While conducting measurements, it is important that the MPPC is held at a fixed temperature. When the device is coupled to a fibre using the ECal connector, there is only poor thermal contact with the cooling plates and the temperature probe. The aim of this study was to deduce the accuracy at which the temperature of the MPPC can be controlled. The experimental apparatus was setup to take a bias scan with the MPPC set at a temperature of 22.0°C. Each scan is performed after the apparatus has been used to acquire other datasets, each scan requiring 1 hour. The motivation for this is that the temperature control system is typically adjusted each day to normalise the temperature of the MPPC against the ambient temperature. If a bias scan is performed on each day of data taking it will give an account of the day to day accuracy of the temperature control, and by measuring the breakdown voltage of the MPPC, it is possible to probe temperature changes of the MPPC. The gathered data is analysed as described in Section 6.1.1 in order to extract the gain and breakdown voltage. The breakdown voltage of each run is then plotted in a histogram and the mean and standard deviation calculated.

In order to examine the light yield stability of the MPPC using the ECal Connector, a short length of Y-11 fibre exposed to a pulsed LED at a fixed intensity. It is then connected and disconnected multiple times, and a charge spectrum taken for each cycle. The mean number of observed photoelectrons of each spectrum is then extracted as described in Section 7.3.4 and plotted against the cycle number. The mean and standard deviation of the full data set is then calculated and the stability deduced.

7.2.1 Results

Figure 7.3 (a) shows the resultant distribution of breakdown voltage for an MPPC for data taken over a period of 22 days. It shows a mean breakdown voltage of 68.97 V with a standard deviation of 0.015 V. If a breakdown voltage dependence on temperature of

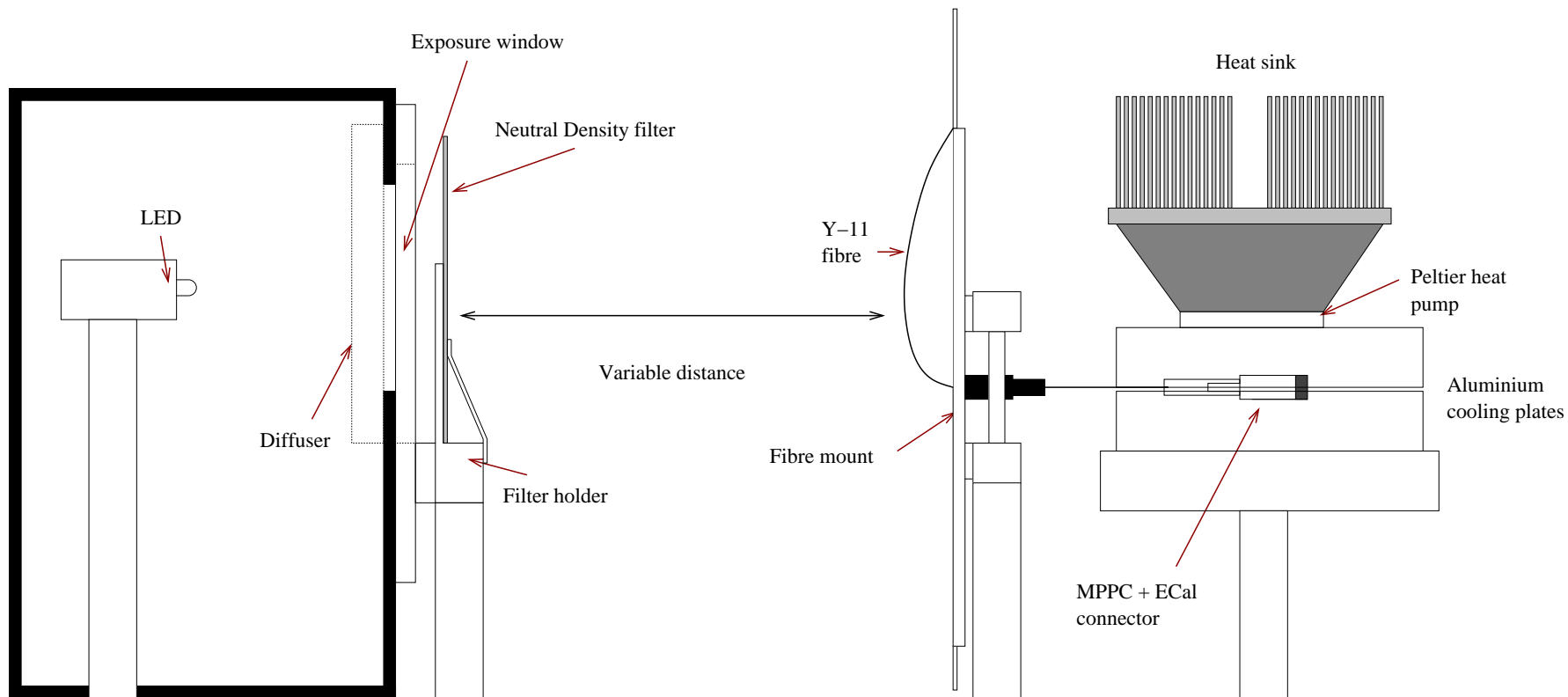
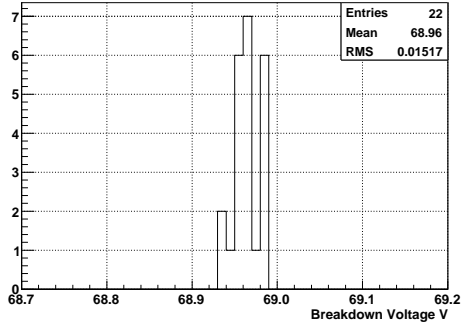
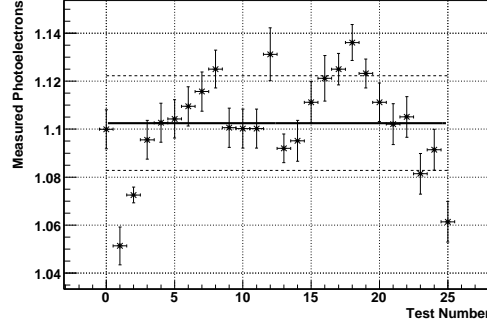


Figure 7.2: Experimental Setup for performing Golden MPPC measurements



(a) Breakdown voltage stability



(b) Light yield stability using the T2K ECal connector

Figure 7.3: (a) The breakdown voltage stability of an MPPC measured over 22 days (b) Light yield stability of the T2K ECal connector. The solid line indicates the mean, and the dashed lines indicate the standard deviation of the data.

60 mV/°C is assumed, this equates to a temperature stability of $\pm 0.3^\circ\text{C}$.

Figure 7.3 (b) shows the result of the light yield test after reconnecting the MPPC to the fibre 25 times. A light yield of 1.10 ± 0.02 pe is measured. The standard deviation of the data shows that a 1.8% fluctuation is expected over multiple reconnections of the fibre.

7.3 Filter and light source calibration

In order to control the illumination of the fibre 60 x 60 mm Neutral Density filters are positioned in the filter holder. Neutral density filters have a flat spectral transmission defined by the optical density of the filter. The optical density (OD) can be used to calculate the transmittance (T) of the filter using the following expression.

$$T = 10^{-OD} \quad (7.1)$$

However since the accuracy of this measurement is of vital importance each filter must be calibrated. In order to perform this calibration the optical power meter photo diode is positioned against the filter holder and two measurements are performed. The reason for close proximity is to ensure both measurements can be made with good signal to noise ratio. This need is more apparent when calibrating filters with high optical density. The measurements made are:

Optical Density	Transmission @ 473nm
0.30	0.475 ± 0.009
0.50	0.295 ± 0.005
0.70	0.181 ± 0.003
1.00	0.097 ± 0.002
2.00	0.0085 ± 0.0002
3.00	0.00066 ± 0.00002

Table 7.1: Transmission of Kodak wratten neutral density filters at 473 nm

1. Power measurement using an LED pulse rate of 10 kHz with a bias of -24 V without the use of a filter
2. Power measurement as above including a filter between the LED and optical power meter.

The transmittance of the tested filter is thus the ratio of the two power measurements and is listed for a wavelength of 473 nm in table 7.1

Using this small number of filters it is possible to produce a wide range of photon intensities from the LED using various combinations. In order to test whether combining the filters gave the expected photon transmission, several simple tests were performed which compared combinations of low optical density filters using the data in table 7.1 and real combinations in the experimental setup. Comparisons were observed to be in very close agreement, however in order to retain accuracy combinations of no more than two filters are used during PDE data runs.

Light source calibration

A light source such as an LED must be calibrated in terms of number of photons per flash in order to allow absolute PDE measurement. In order to perform this calibration a Newport 1835C optical power meter [90] is used. The optical power meter uses a wavelength calibrated InGaAs photo diode in order to convert an input optical signal into a measurement of power in Watts. The diode is circular with an area of 1 cm^2 and can be directly exposed to a light source or, by using an adaptor with the tip of a fibre using the

ECal connector.

In order to calibrate the LED the following procedure is carried out. Points 2 and 3 are ignored if no fibre is being used during the experiment.

1. The optical power meter photo diode is cleaned using IPA and a cotton bud. Care is taken not to use an excessive amount of IPA, as this leaves residue on the photo diode surface and thus reduces the accuracy of the calibration.
2. The flat plate holding the wavelength shifting fibre is fixed to the optical rail
3. The fibre mounting fixture is screwed into the optical power meter and it is introduced to the wavelength shifting fibre.
4. Any filters are removed from the filter holder.
5. The dark box is closed.
6. The optical power meter is powered and allowed 5 minutes to settle before it is zeroed.
7. The LED is pulsed at a rate of 10 kHz with a bias voltage of -24 V for 5 minutes to allow the optical signal to stabilise.
8. The optical power is measured and the number of photons per flash is calculated using the following,

The energy per photon is given by

$$E_{\gamma} = \frac{hc}{\lambda} \quad (7.2)$$

the energy per LED flash is given by

$$E_f = \frac{\text{Power}}{\text{Rate}} \times \text{Acceptance Correction} \quad (7.3)$$

and the number of photons per flash can be calculated from

$$N_{\gamma} = \frac{E_f}{E_{\gamma}} \quad (7.4)$$

The value of the Acceptance Correction should be determined for each operating configuration, for both a raw LED flash and when using an illuminated fibre. A discussion of

the acceptance calculations that were performed for each light source are discussed in the next section. Once the number of photons per flash has been calculated for an unfiltered LED, a set of filter combinations are chosen that will produce a mean intensity of between 0 and 10 photons per flash in no more using no more than 3 filters. This limit on the number of photons per flash is to ease analysis of the resultant charge spectrum, limiting the distribution to a low number of photoelectron peaks.

7.3.1 Source wavelength spectrum

Wavelength spectra have been measured for each light source. From the distributions the mean wavelength is found and used in Equation 7.2. In order to perform these measurements, the output of a monochromator is read out using the Newport optical power meter. Each wavelength is selected and matched to the wavelength calibration of the optical power meter and the absolute optical power at each wavelength is measured.

The LED used on the ANTARES pulser is an Agilent Technologies HLMP-CB15. It has a peak spectral intensity of 473 nm, and prior to cleaving produces photons in a cone with a half angle of 15° [91]. This LED is the same as that used to illuminate the length of Y-11 fibre (See Section 3.3.7 for fibre specifications). The fibre has an absorption range within the LED emission (broad peak from 440 to 460 nm) and so is appropriate for use in this method. In the case of the LED spectrum, the LED is positioned directly in front of the monochromator input. For the WLS fibre, a bundle of fibres is positioned at the monochromator input, while 10 cm lengths of the bundle are exposed from the side to LED light. Photons absorbed by the fibre are re-emitted at a longer wavelength are then passed through the fibre to the monochromator.

The spectra for both the LED and observed Y-11 fibre are shown in Figure 7.4. The peak mean and σ of the LED has been measured to be 471 ± 16 nm and is in agreement with the datasheet. The peak wavelength of the Y-11 fibre exposed to the LED is found to be at 506 nm, however the mean of the whole distribution is found to be 538 nm with a rms of 31 nm. A value of 538 nm is used in all calculations of the mean number of photons from the Y-11 fibre.

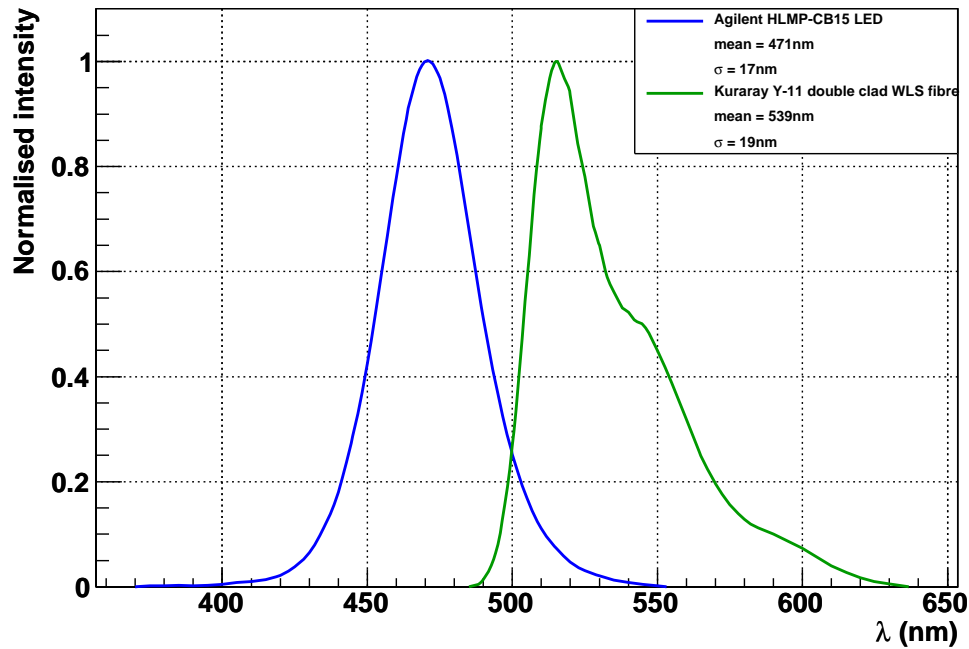


Figure 7.4: Intensity spectrum of Agilent HLMP-CB15 LED used with the ANTARES pulser, and the emission spectrum of a 30 cm length of Kuraray Y-11 fibre exposed to the LED

7.3.2 MPPC photon acceptance

The acceptance of the MPPC to photons has been calculated for both described data taking configurations. The first is the direct exposure of an MPPC to LED light, and the second when the MPPC is coupled to a length of Y11 fibre and the exposed. Each require different consideration, the first can be performed using geometric considerations and the measurement of the LED pulse profile. The second requires understanding how photons exit the fibre tip and the distribution across the whole area, in order to achieve this a photon generator was developed using the Geant 4 framework [92].

Acceptance to direct LED flashes

An LED emits light focussed into a cone by the lens of the standard packaging. This means as a photosensor is moved away from the beam, the intensity will fall. In order to counter this effect, the light is passed through a diffuser in order to smooth the intensity

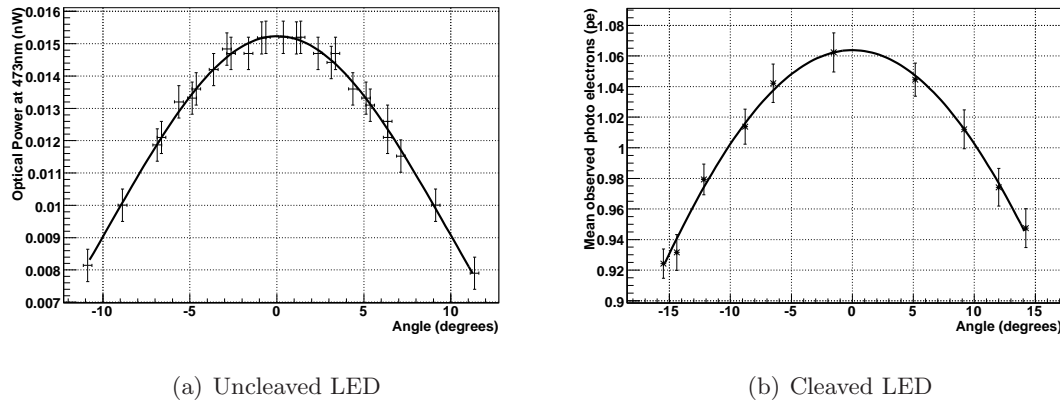


Figure 7.5: Intensity of uncleaved LED as function of angle. The curves are Gaussian with $\sigma = 9.8^\circ$ and $\sigma = 29.1^\circ$ for an uncleaved and a cleaved LED respectively. Both are in good agreement with the data

profile and to reduce any non-uniformity of the beam. Due to the different size and shape of the two types of photosensors (1 cm^2 circular optical meter and, 1 mm^2 or 1.69 mm^2 MPPCs) it is important to consider how the intensity of the LED will be integrated by each device and calculate the correct conversion factor between them. The measurement of intensity profile has been performed by two methods. The first used the optical power meter to observe the LED, while the second used an MPPC. The measurements are taken by passing the photosensor through the LED beam at different heights at a fixed distance, from this both the angle and light intensity can be deduced. The reason for using different photosensors was due to the relative size and sensitivity of the two sensors with respect to the measurement being taken. The uncleaved LED could be scanned easily using the optical power meter with a small aperture applied and still observe a signal well about noise. However for the cleaved LED it was apparent the photosensor must be closer in order to observe a wide enough angle, while using a very small sensitive area.

The results of these measurements are shown in Figure 7.5. A Gaussian function is fitted to the data, with $\sigma = 9.8^\circ$ for the uncleaved LED, and with $\sigma = 29.1^\circ$ for the cleaved LED. This is used for performing an acceptance ratio calculation that accounts for the different photosensor shapes.

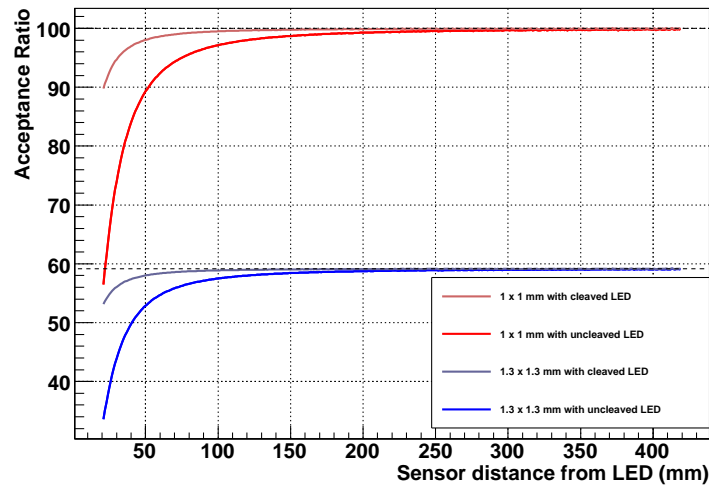
The acceptance ratio calculation is done by calculating the angle each photosensor subtends when positioned at an arbitrary distance from the LED, then performing an inte-

gration under a 2D Gaussian within the bounds of the photosensor. The ROOT analysis framework allows the integration of the volume under the 2D Gaussian, however it only integrates the volume underneath a square. This is adequate for the MPPCs which have square active areas, however in the case of the optical power meter which has a circular active area, the integration has been performed by dividing the circle into a grid of squares. In order to improve the accuracy of the integration, the grid size has been set as small as possible without requiring an extremely long calculation time. The acceptance ratio is then the ratio between the power observed by the Newport optical power meter and the MPPC. For a 1 x 1 mm MPPC this is expected to be 100 and for a 1.3 x 1.3 mm MPPC a value of 59.2 is expected.

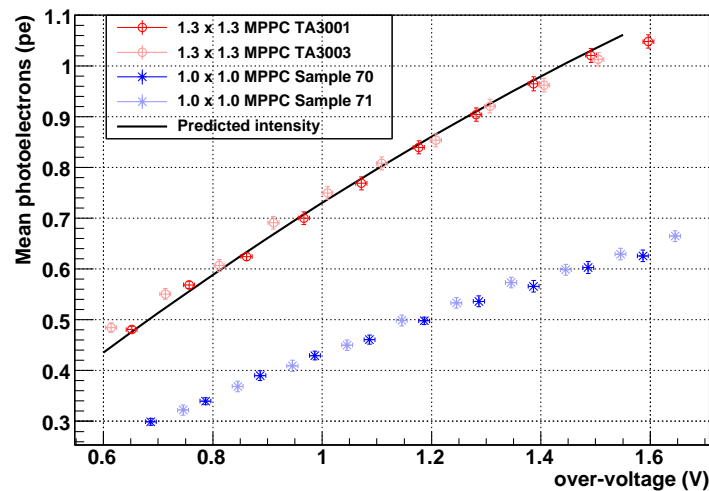
A plot of acceptance ratio as a function of photosensor distance is shown for both a cleaved and uncleaved LED source in Figure 7.6. The results show that the acceptance is only critical to the accuracy of the photosensor calibration at a separation of less than 200 mm for an uncleaved LED and less than 100 mm for a cleaved LED. In order to improve the accuracy of the photon calibration, based on this calculation a cleaved LED is used with a photosensor separation of over 200 mm is used. The figure also shows a direct comparison between the observed light yield of four MPPCs exposed to a fixed intensity cleaved LED. The black curve is a polynomial fit made to the trend by the 1 x 1 mm MPPC, which has been renormalised by a factor of 69% to match area ratio between the 1.3 x 1.3 mm and 1 x 1 mm MPPCs. This direct normalisation matches the trend in the data very well.

Acceptance of photons from wavelength shifting fibre in Geant4

The distribution of photons emanating from a length of Y-11 fibre is not easy to reproduce analytically based upon geometry and solid angle calculation. This is due to the nature of the fibre and how light is absorbed and re-emitted along its length (Section 3.3.7). Unlike normal optical fibre in which light is injected into one end and is internally reflected, Y-11 relies on photons with wavelengths in its absorption region entering the fibre. Once absorbed, photons of longer wavelength are emitted isotropically. This means that photons can emanate from any position throughout the fibre and at any angle within the acceptance of the fibre. The Y-11 fibre used in ND280 is 1 mm diameter and is double clad, with an acceptance of 45.68° to an air interface. This means that photons are expected to emerge



(a) MPPC acceptance ratio with between optical power meter



(b) MPPC light yield comparison between 1 x 1 mm and 1.3 x 1.3 mm devices

Figure 7.6: (a) Acceptance ratio between Newport optical power meter and MPPCs for cleaved and uncleaved LED, (b) Light yield comparison between 1 x 1 mm and 1.3 x 1.3 mm MPPCs using an uncleaved LED

from the fibre into air with angles from 0° up to this angle.

However, a visual inspection of a side illuminated fibre shows that beyond the acceptance angle, photons emerge from bands at the edge of the fibre (Figure 7.7). The reason for this is due to the mode in which photons are produced by the fibre. As photons within the absorption band may be absorbed at any point in the fibre, it is possible for photons to be emitted close to the cladding and take a path that spirals around the edge of the fibre toward the end. These photons may emerge with high angles to the normal. These photons are called skew photons.

The development of this simulation follows that used in [93]. However the basic design of the simulation has been improved upon to achieve more accurate reproduction of light emerging at all angles. Particular attention has been paid to improving the smoothness of the distribution of light and the accurate reproduction of skewed photons which emerge at specific locations and angles which were given no specialised treatment other than location in the basic simulation.

Simulation Coordinates

In this simulation a cylindrical polar coordinate system is used, where the origin is placed at the centre of the fibre face. Photons must be generated in terms of r , θ and ϕ , both in position and in momentum direction.

Angular distribution

In order to produce an accurate acceptance simulation, the angular and spatial distribution of photons must be studied [93]. In order to do this, photographs are taken of a Y-11 fibre at a range of angles using a digital camera. The fibre is side illuminated using a UV lamp such that the fibre continuously produces photons at its tip. Digital photographs are then taken in darkness such that only light from the lamp is captured by the camera. The exposure time and aperture of the camera is fixed for all photos, and is such that the CCD is not saturated, but the light level is above background noise. 5 sample photographs are shown for reference in Figure 7.8. A series of photographs are taken through a range of angles, the viewing angle of the camera with respect to the fibre is calculated by measuring

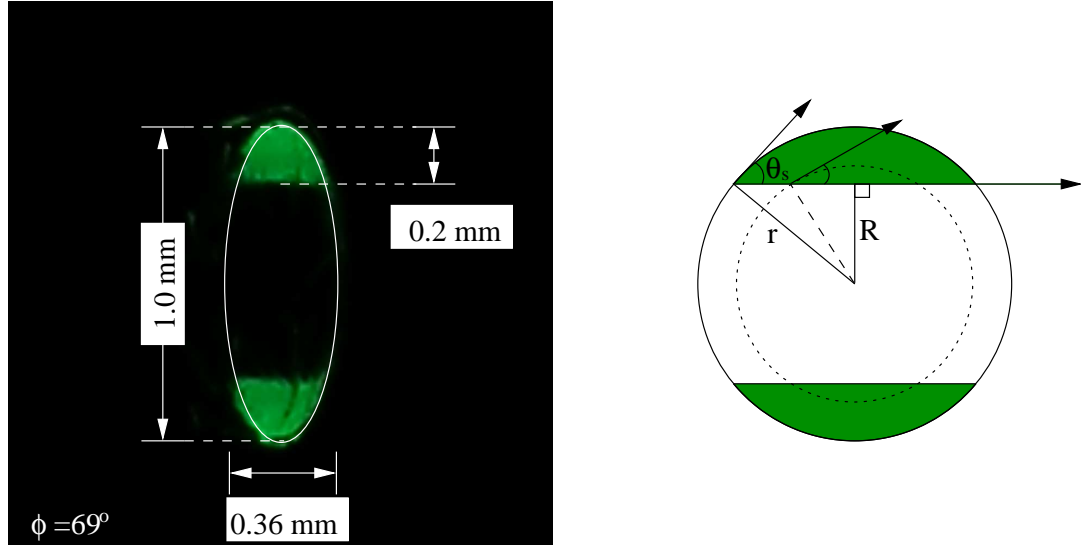


Figure 7.7: (left) Example of dimension measurements made on all photographs, and measurement of banding on the fibre face due to skew photons. (right) Geometrical consideration of maximum θ of skewed photons depending upon radius.

the dimensions of the resultant ellipse using,

$$\phi = \sin^{-1} \left(\sqrt{1 - \frac{b^2}{a^2}} \right) \quad (7.5)$$

where a is the semi-major axis and b the semi-minor axis of the ellipse.

For each photograph (angle) the total grey intensity of the fibre tip is measured using a Java based image analysis tool [94]. The intensity of each subsequent angle is integrated and divided by the total over all angles. The angle is then plotted against the normalised integrated intensity (Figure 7.9). This plot is fitted using two functions applied over different ranges of x in order to describe the data with a smooth function. The fitted functions and ranges are as follows,

$$x \leq 0.6 \quad \phi = 17.8\sqrt{15.7x} \quad (7.6)$$

$$x \geq 0.6 \quad \phi = 42.5 + 2.2x + (2.9 \times 10^{-10}) \exp(25.1x) \quad (7.7)$$

In the simulation, a random number is generated between 0 and 1, this number is inputted into the above equations depending upon the value, and the resultant value is then set as the angle ϕ for the generated photon.

Spatial distribution and skew photons

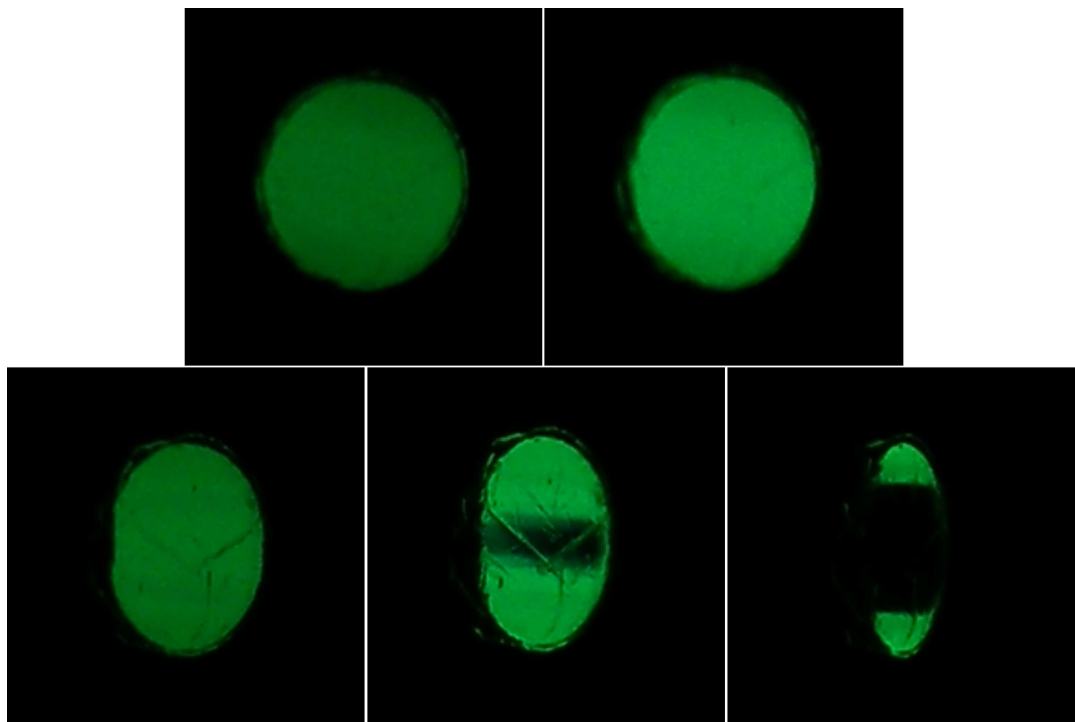


Figure 7.8: Photographs of Y-11 fibre taken at 0, 14, 37, 50 and 69° to the fibre axis

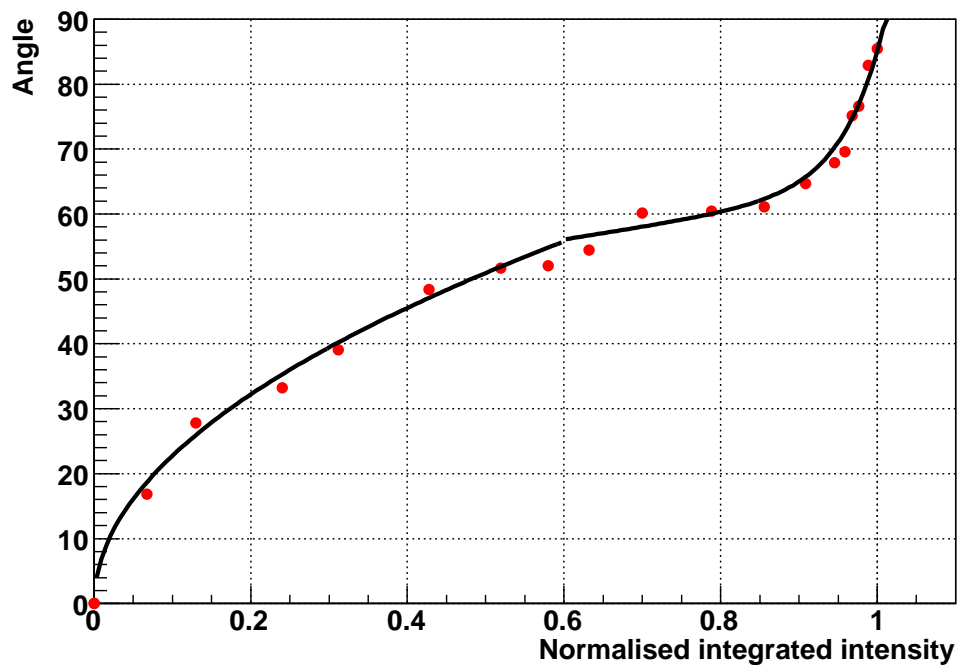


Figure 7.9: Angle as a function of integrated intensity

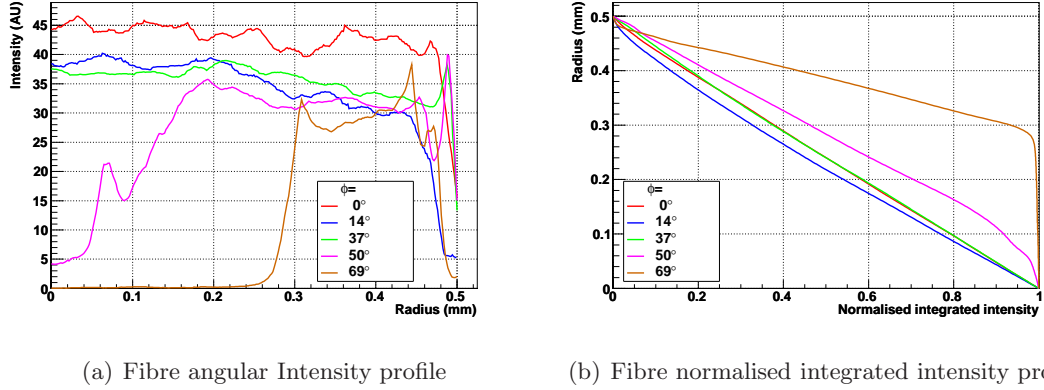


Figure 7.10: Angle as a function of integrated intensity

In order to position generated photons upon the face of the fibre, the above data set is analysed once more. In this analysis a cross-section of the image is taken along the semi-major axis of the fibre and a profile histogram produced of the grey intensity. 5 examples are shown in Figure 7.10(a). If a dark band across the fibre is visible, the width is measured and used to produce a band width vs ϕ plot. Following the method used above, normalised integrated intensity is plotted as a function of radius from the centre of the fibre, this is shown in Figure 7.10(b). A look up table is thus generated for each ϕ angle. Once the angle ϕ is selected using the above function and a random number generator, the nearest ϕ look up table is then used. Once more a random number is generated and the value of r is selected from the integrated intensity plot (Figure 7.10(b)).

For all photons, the angle θ is used twice, first to determine the the location (θ_l from here onwards) on the surface of the fibre and again to determine the direction of the photon (θ_d). When considering the location on the face of the fibre, spherical polar coordinates are used but ϕ is fixed to 0° . For locational purposes θ_l is generated randomly between 0° and 360° , following the observation that rotating the fibre on its axis has no effect on the intensity or appearance of banding. This θ_l cannot be used in order to determine the direction of the photon. If it is, all photons are projected outwards radially from the fibre, therefore θ_d is generated randomly over the same range and used for photons with $\phi < 50^\circ$. For photons $\phi > 50^\circ$, it is observed that skew photons are produced in a region on the outer radius of the fibre, and a dark band passes horizontally across the fibre face as observed in Figure 7.7. In order to reproduce this in the simulation, for each ϕ the radius of the dark band is measured and shown in Figure 7.11. The following equation is the result of

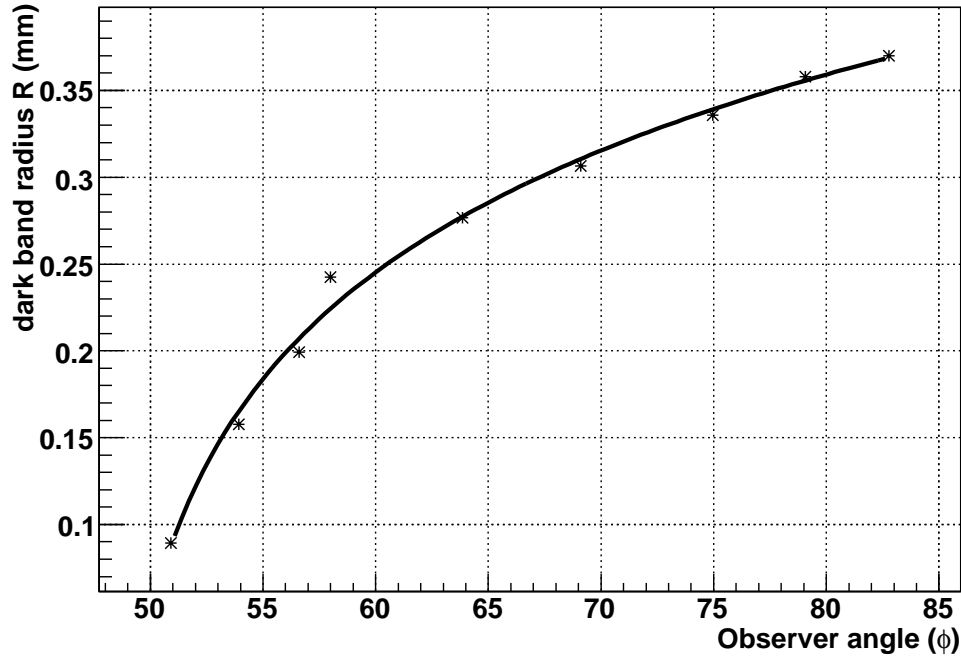


Figure 7.11: Skew photon dark band radius vs angle

an empirical fit made to the data points in order to describe the dark band radius, R at all ϕ .

$$R = 0.052 + 0.12 \ln(\phi + 47.7) \quad (7.8)$$

The band radius is used to calculate the maximum angle to the tangent of the fibre at which a skew photon can emerge from the fibre depending radial distance from the fibre centre using the following expression.

$$\theta_s = \cos^{-1}(R/r) \quad (7.9)$$

where, R is the band radius, and r is the radial location of the fibre as selected previously. In order to produce a banding like behaviour the value of θ_d is generated between

$$(\theta_l \pm 90) - \theta_s < \theta_d < (\theta_l \pm 90) + \theta_s \quad (7.10)$$

By limiting the projection of photons in this manner, photons are produced tangentially in both directions from the fibre within an allowed cone which would produce the observed banding.

The simulation contains 2 geometrical components; the photosensor and an epoxy layer. The photosensor considered in this case is the Newport optical meter photo diode. It

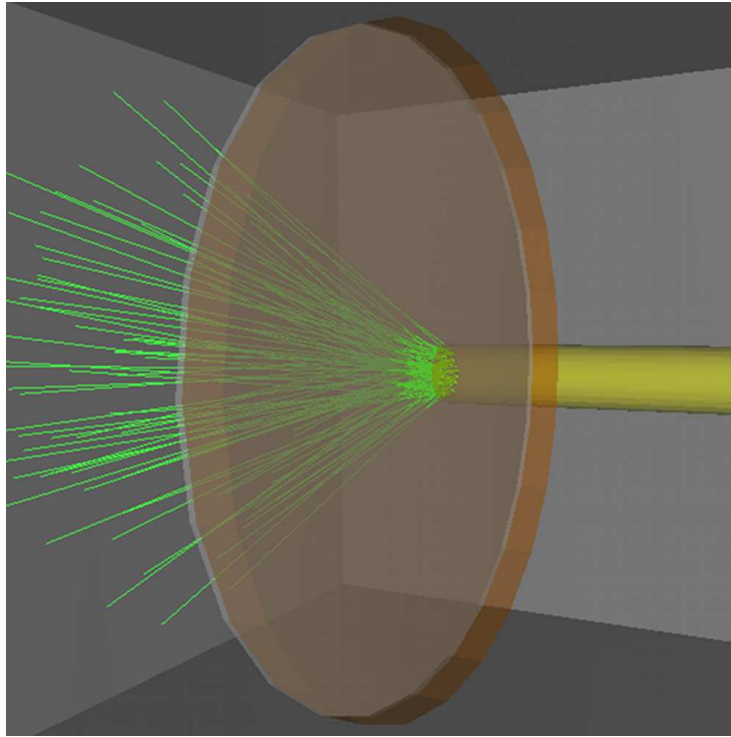


Figure 7.12: Example fibre simulation visualisation showing 100 photons (green), an epoxy layer (orange). The fibre is shown as a visual aid in yellow.

is centred upon the fibre at a selected distance and is circular with a radius of 5.6 mm. Directly in front of the photo diode is an optional layer of epoxy, with refractive index of 1.52, with the same radius but variable thickness. The photo diode much like the MPPC has a protective surface layer although no information regarding its thickness is known, thus for this simulation it was assumed it has identical thickness to the epoxy. This would not effect the result of the simulation as the area of the photo diode is approximately 100 times that of the MPPC, and the presence of epoxy causes refraction and the focussing of light from the fibre into the centre.

Each photon is generated and is tracked through the epoxy and the position at which they intersect the photo diode is recorded in Cartesian coordinates. During this study a range of epoxy thicknesses between 0.1 and 0.6 mm were examined based on the tolerances provided by Hamamatsu [95]. For comparison the simulation was performed using the same separation but without an epoxy layer.

In order to calculate the acceptance correction, a 1.3×1.3 mm and 1.0×1.0 mm square

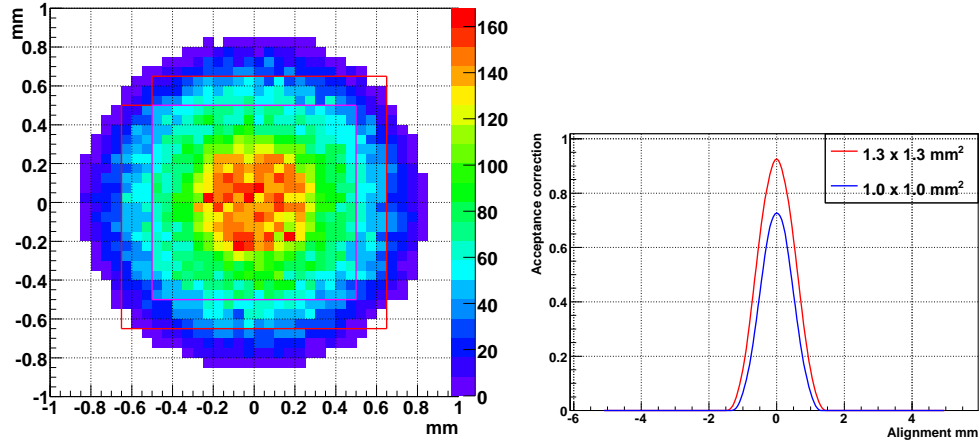
are centered vertically and tracked from the edge of the 5.6 mm radius through the centre and across the full diameter of the Newport optical meter in 0.05 mm steps. At each location all the photons within each of the two areas are integrated and divided by the total number of photons that hit the diode surface.

Figure 7.12 shows an example visualisation, Figures 7.13(a) and 7.13(b) show example intensity distributions for a simulation with and without epoxy, with acceptance ratios given as a function of alignment. It is clear from this Figure that the epoxy has the effect of greatly focussing the light from the tip of the fibre due to the closely matched refractive indices.

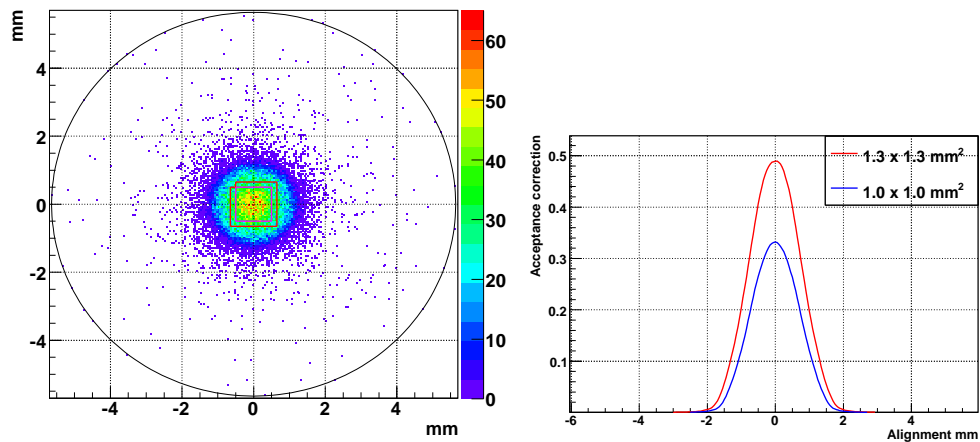
In order to account for the mis-alignment of the fibre with the MPPC due to tolerances on the connector dimensions and the gluing of the fibres, a mean mis-alignment of $50 \mu\text{m}$ is assumed to give the mean acceptance ratio and the upper and lower limits corresponding to perfect alignment and $100 \mu\text{m}$ respectively. A plot of acceptance ratio as a function of photosensor separation is given in Figure 7.14(a). This figure shows how the separation between the fibre and MPPC quickly changes the acceptance. For an MPPC with a 0.4 mm epoxy layer an acceptance is $0.94_{-0.010}^{+0.006}$ is predicted. The relative increase in acceptance between the $1.0 \times 1.0 \text{ mm}$ and $1.3 \times 1.3 \text{ mm}$ MPPC predicted by this simulation is of the order of 25% for 0.4 mm of epoxy and is shown in Figure 7.14(b). Shown in Figure 7.15 are the results of light yield measurements taken with $1.0 \times 1.0 \text{ mm}$ and $1.3 \times 1.3 \text{ mm}$ MPPCs, the back curve indicates the predicted light yield of the $1.3 \times 1.3 \text{ mm}$ devices based on the yield measured by the $1.0 \times 1.0 \text{ mm}$ devices. An increase of approximately 25% is supported by this study and also by measurements made by the T2K FGD group at Kyoto [96]. A mis-alignment of up to $100 \mu\text{m}$ in the above results predict a variation in the observed intensity by approximately 1.9%. This figure is in agreement with those produced by studying the variation of the mean number of photons in Section 7.2.

7.3.3 Preparation and data taking

The photon calibration is only valid for the specific distance between the LED and surface of the optical power meter or wavelength shifting fibre. A distance setting jig has been manufactured such that after each calibration the jig is moved into contact with the housing of the optical power meter and fixed in place. The optical power meter is then



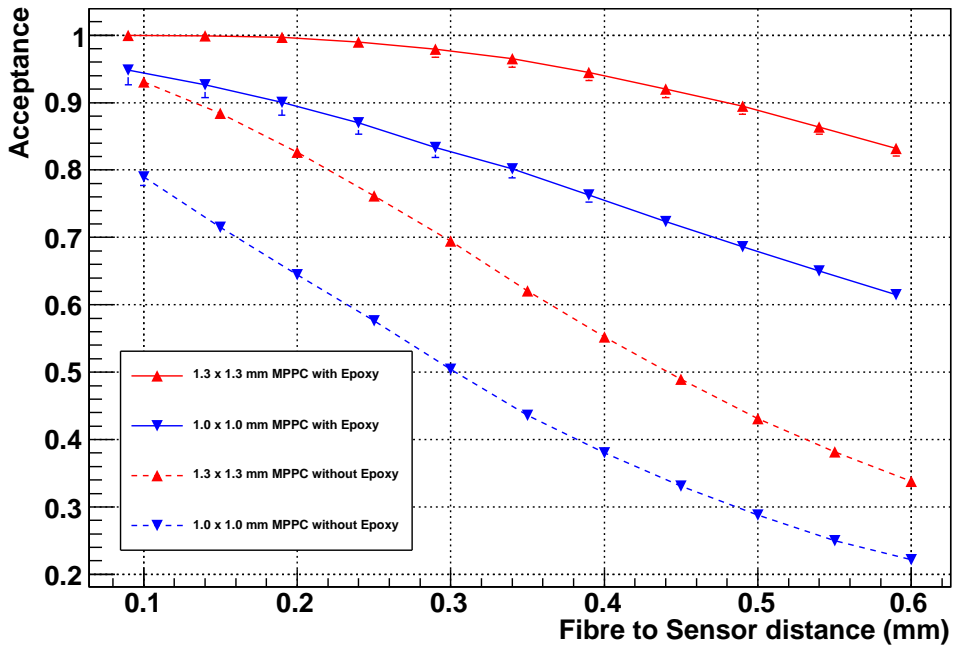
(a) Fibre acceptance simulated with epoxy layer



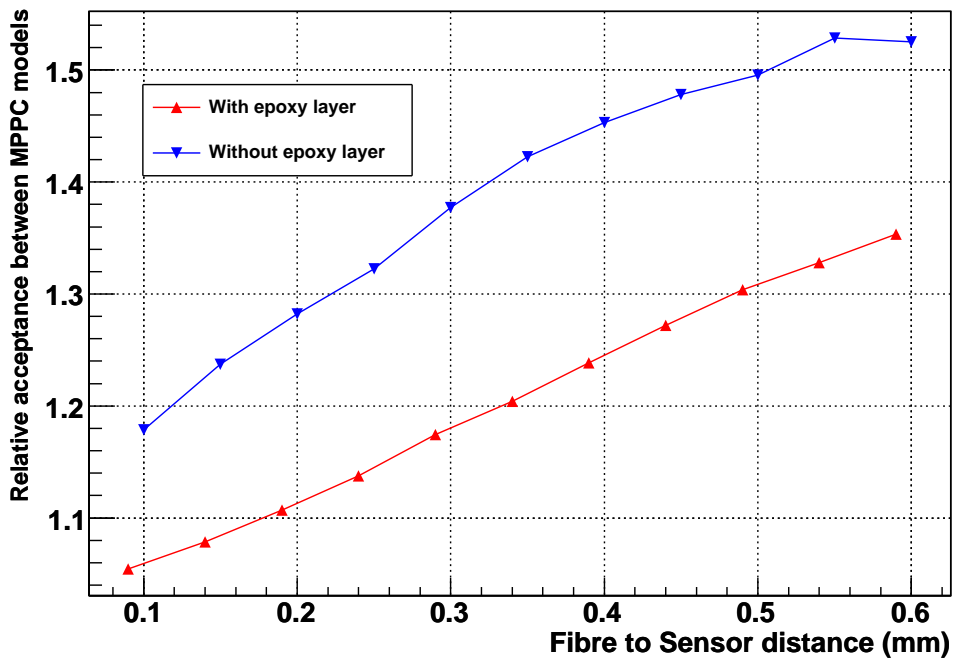
(b) Fibre acceptance simulated without epoxy layer

Figure 7.13: Simulation of 50,000 photons from the tip of a fibre, for a separation of 0.45 mm. The square boxes shown represent the active areas of each photosensor, and in the case of the simulation without epoxy the circumference of the Newport optical power meter is shown.

removed and the MPPC mounting system is then introduced to the jig. Due to cut outs made to the jig the surface of the MPPC is positioned at the same separation from the LED as the optical power meter previously. When using the fibre configuration the position of the fibre is fixed on the support structure as described previously. The optical power meter can thus be removed and exchanged for an MPPC easily using the T2K ECal connector as shown in Figure 6.10.



(a)



(b)

Figure 7.14: Acceptance comparison between different MPPC models simulated with and without an epoxy coating. (a) Shows the fall of acceptance as the separation is increased for all models and configurations. (b) Shows the relative increase in the acceptance between MPPC models.

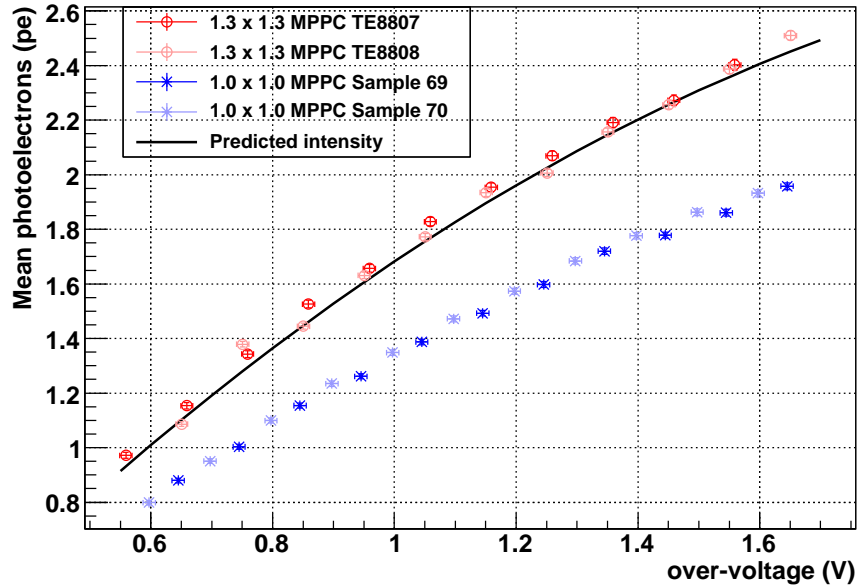


Figure 7.15: Light yield comparison between 1 x 1 mm and 1.3 x 1.3 mm MPPCs coupled to Y11 fibre, the black line indicates the predicted increase in yield compared to the 1 x 1 mm devices

Once the MPPC has been positioned or coupled to the light source, the temperature control system is switched on and set to a target temperature of 22.0°C (unless stated otherwise for a particular data set). This temperature is chosen to match the target temperature of the ND280 ECal cooling systems. A thermocouple probe is also applied to a lead of the MPPC, as the lead is wire-bonded to the substrate the aim is to measure the temperature more accurately than taking a measurement on the ceramic packaging. A K-Type Hanna Instruments digital thermometer is used to record this measurement.

While the system is cooling the selected filters are positioned into a holder between the LED and the MPPC. On one edge of each filter, its optical density value is printed in white. This text is used to orientate the filter so it may be used in the same rotation for each run. As this part of the filter is not useful to the experiment, it may be handled on this edge also. By enforcing the same rotation for each run, it ensures consistency in transmission between runs and produces more accurate calibration should the filters obtain scratches during use. Once all filters are in place the dark box is closed and the MPPC biased. The oscilloscope is setup to integrate MPPC response to the LED flash

over a period of 200 ns. At this time test charge spectra are taken at both low and high MPPC bias (typically at over-voltages of 0.7 and 2.0 V respectively) in order to check that the charge spectrum is binned correctly to show good photoelectron peak separation and that no significant over or under-shoot is evident.

Data taking then proceeds in the form of a bias scan, as discussed previously, each bias producing a charge spectrum. For calibrated data such as this, the charge distribution is used in order to extract the PDE of the MPPC at each bias.

7.3.4 Analysis

An analysis routine has been developed using the ROOT analysis framework [85]. The analysis performs basic parameter extraction as detailed in Section 6.1.1. The PDE relates to the mean number of photons as a direct conversion factor between the number of photons incident to the number of photoelectrons measured. However, this does not account for secondary effects which add extra charge to the output such as afterpulse and crosstalk. To account for these effects the analysis is split into two methods. The first attempts to extract the mean number of photoelectrons by first converting the charge spectrum into integer bins as discussed previously. Once this has been performed TMinuit is used to perform a least squares fit of a Poisson function (Equation 7.11) to the distribution. The mean extracted via this method will be referred to as the ‘Fit mean.’

The second approach aims to extract the mean number of APD triggers free of crosstalk and afterpulsing effects by examining the region of the spectrum which is independent of such processes. Thus this analysis focuses solely on the total number of events and the number of events occurring in the pedestal. In order to extract the mean from these two quantities, consider the Poisson distribution below,

$$f(k; \lambda) = \frac{\lambda^k e^{-\lambda}}{k!} \quad (7.11)$$

where k is a integer representing number of APD triggers and λ is the mean number of APD triggers for the distribution. If the only information used is the number of events occurring in the pedestal (or zero bin), k is set to zero and the distribution becomes,

$$f(0; \lambda) = \frac{\lambda^0 e^{-\lambda}}{0!}$$

$$f(0; \lambda) = e^{-\lambda} \quad (7.12)$$

By rearranging this equation to put λ as the subject the following expression is obtained,

$$\lambda = -\ln(f(0; \lambda)) \quad (7.13)$$

where $f(0; \lambda)$ is the probability of observing events in the zero bin of a distribution with mean λ . This quantity is known for each charge spectrum taken during the experiment, and is the ratio of zero charge events (N_0) to the total number of events in the spectrum (N_t) and thus the final form of the equation becomes,

$$\lambda = -\ln\left(\frac{N_0}{N_t}\right) \quad (7.14)$$

In order to correct for events that do not appear in the bin zero due to dark triggering of APDs, if equation 7.12 is considered with λ set to $(\lambda + \mu)$ by assuming the observed distribution is the sum of two Poissons with different mean values. Retracing the above considerations results in being able to subtract the mean of a pedestal spectrum from equation 7.14 in order to correct for dark counts.

$$\lambda = -\ln\left(\frac{N_0}{N_t}\right) - \mu \quad (7.15)$$

In order to calculate μ Equation 7.14 is applied to a pedestal spectrum. While the same correction is made to each spectrum, the correction becomes more influential on the extracted mean when the number of incident photons is very low. The mean extracted via this method will be referred to as ‘Poisson zero mean’.

The statistical uncertainty on λ is found by taking the uncertainty on each variable as $1/\sqrt{N}$ and thus the total expression becomes,

$$\Delta\lambda = \sqrt{\frac{1}{N_0} + \frac{1}{N_t}} \quad (7.16)$$

This is added to the statistical uncertainty on the dark count mean in quadrature.

In the case of data taken reading out the tip of a fibre, an extra uncertainty is added to the data originating from the reproducibility of the optical connection. This has been measured to be of the order 1.8% (Section 7.2) experimentally and simulated to be 1.9% based upon connector tolerances (Section 7.3.2). Thus a figure of 1.85% is used.

Once the mean number of photoelectrons has been extracted from each charge spectrum a plot is produced of mean photoelectrons against incident photons for each bias voltage. Linear fits are made to both the Poisson zero mean and fit mean plots. The gradient of the plot is used to extract the photo detection efficiency.

The quality of the data can be studied in two ways. The first is to extract the breakdown voltage for each photon intensity and check for large variation. Due to the experimental procedure it is necessary to open the dark box continuously, and so, if the temperature outside the dark box is significantly different to the target temperature, opening the box can cause large fluctuations in breakdown voltage. This is most evident at low bias voltage if the temperature of the MPPC is not allowed to stabilise. The second is to check the value of the intercept of the linear fit used to extract the PDE. As the over-voltage decreases to zero the PDE should follow and result in a value close to zero. If there is a significant offset it points to there being issues during calibration of the photon source.

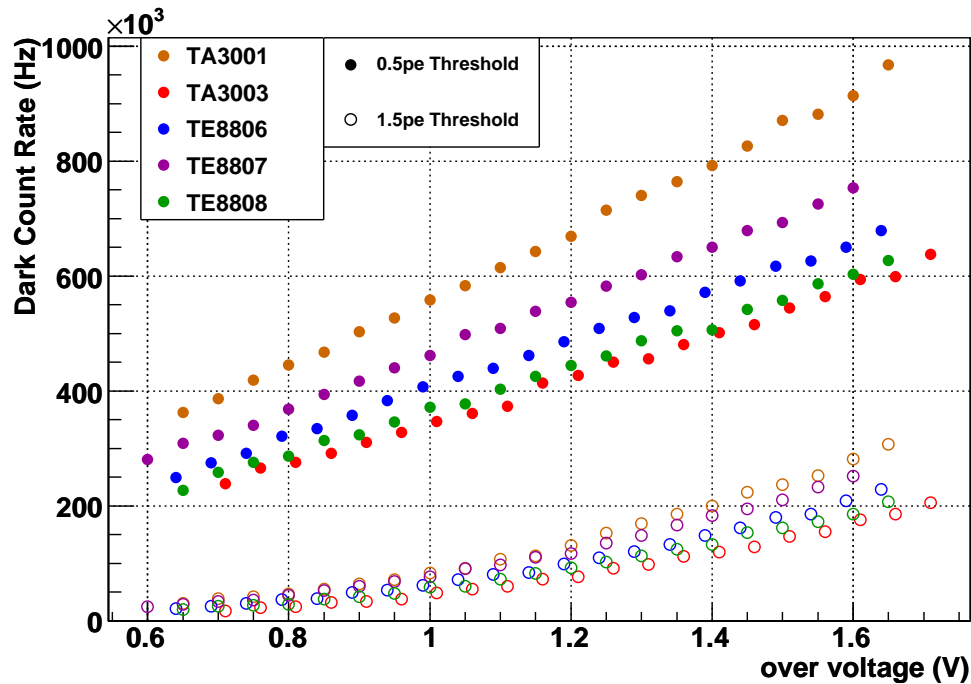
7.3.5 Results

Extraction of the PDE has been performed on final production model S10362-13-050C 1.3 x 1.3 mm device for use with QA with LED at 473 nm and at 538 nm with a 30 cm length of Kuraray Y-11 Fibre.

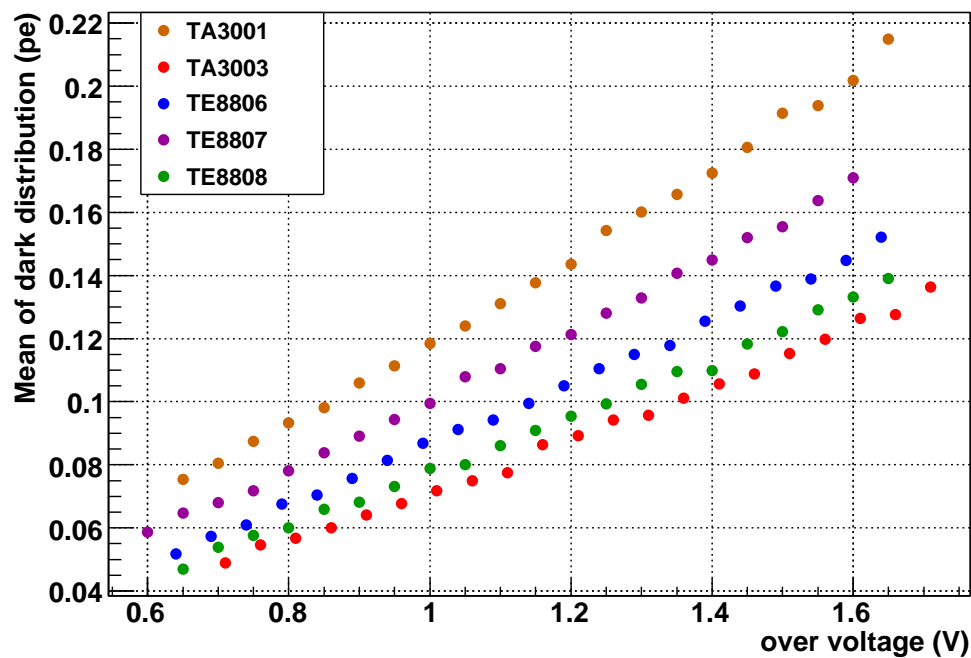
The measured dark count rate and dark mean used in the dark count subtraction of Equation 7.14 are shown in Figure 7.16 for each device then a polynomial fit is made and the value of μ at any over-voltage is found.

Figure 7.17 shows plots of extracted mean against expected number of photons for both fitting and counting methods for the device serial TA3001 exposed to pulsed LED light at 473 nm. This plot shows how the fitting method produces the predicted increase in the observed PDE compared to the intrinsic PDE extracted using the counting method. This increase is observed to be less prominent at lower voltage, which is expected as these effects are less significant when operating at low gain. At the proposed T2K operating over-voltage of 1.3 V, the device displays a intrinsic PDE of $30.8 \pm 1.1\%$.

Figure 7.18 shows plots of extracted mean against expected number of photons for both fitting and counting methods for all tested devices using Y-11 fibre. From these plots

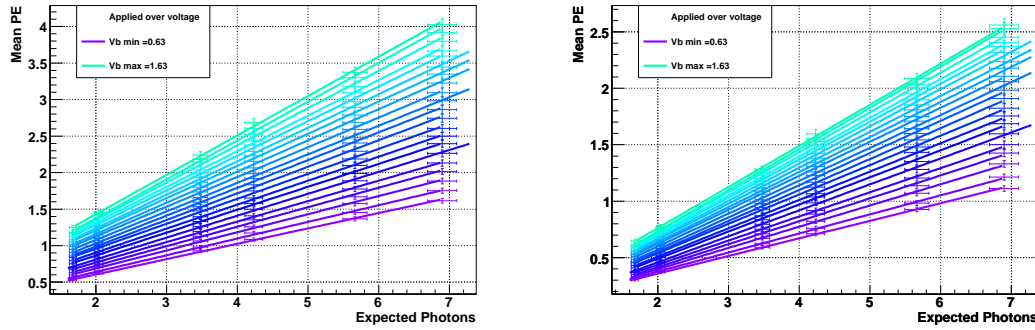


(a) Dark rate at 0.5 pe and 1.5 pe thresholds at 22°

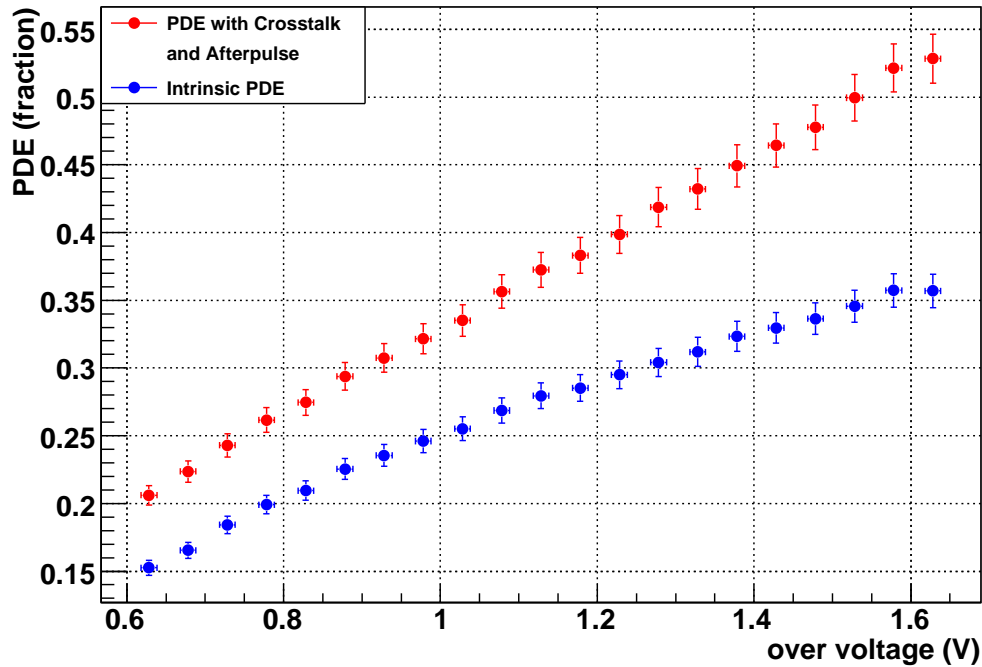


(b) Dark mean of biased devices extracted from pedestal spectrum

Figure 7.16: Darkrate and mean for T2K Devices tested for Golden MPPC calibration



(a) Mean observed photoelectrons extracted by a poisson fit against expected number of photons
 (b) Mean observed photoelectrons extracted by the counting method against expected number of photons

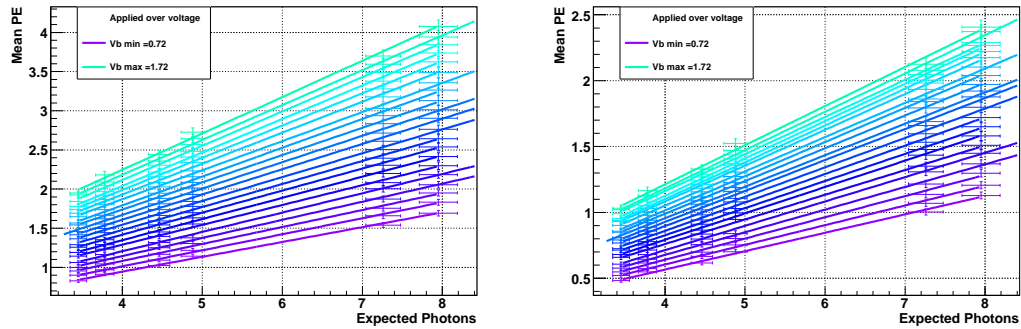


(c) Extracted PDE against over-voltage for both methods

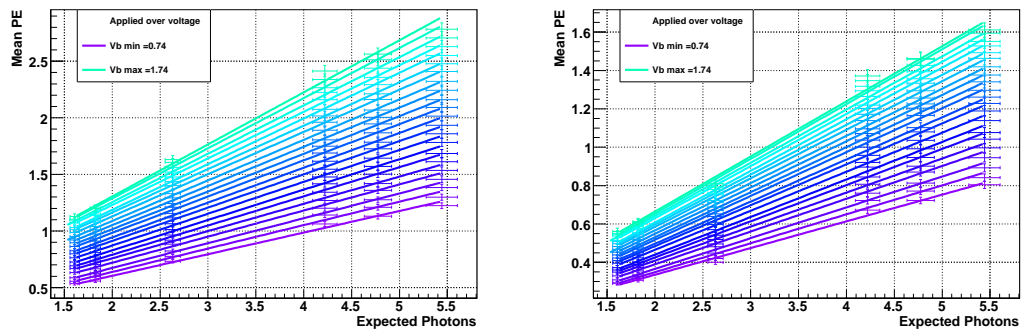
Figure 7.17: PDE dataset for T2K production device TA3001 exposed to pulsed LED light with a mean wavelength of 473 nm

the gradient of the first order polynomial is extracted for each method and applied over-voltage. This gives two values of PDE at each voltage which are shown in Figure 7.19. It shows that for the proposed operating voltage in the ND280 ECal of 1.3 V over-voltage a mean photo detection efficiency of $23.7 \pm 0.5\%$ has been observed. It is evident that the PDE as extracted using the fit mean of each spectrum produces a higher photodetection

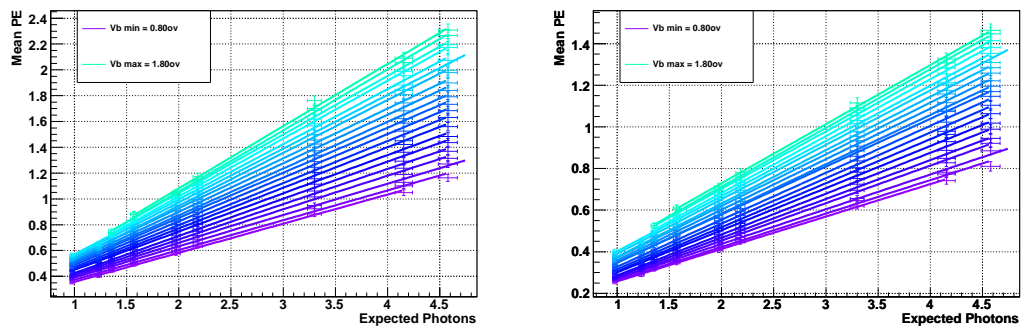
efficiency than when extracting the mean through the Poisson zero method as predicted previously. Crosstalk and afterpulse effects artificially increase the intrinsic PDE of the device by approximately 46%.



(a) TE8807



(b) TE8808



(c) TA3003

Figure 7.18: Extracted mean using fitting and counting methods respectively for devices TE8807, TE8808 and TA3005

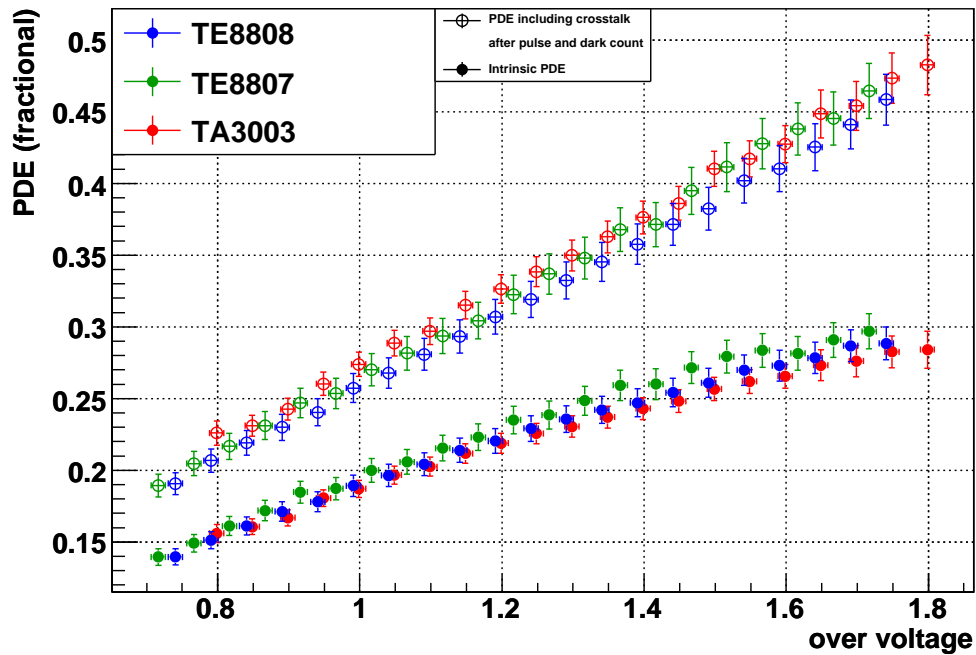


Figure 7.19: PDE of all golden MPPCs before use in QA test setups

7.4 Conclusion and discussion

The PDE of the T2K 1.3 x 1.3 mm production MPPC has been measured under two operating configurations, the first exposing the photosensor to 473 nm photons produced by an LED and the second by exposing a length of Y11 fibre and reading out the photons at one of the fibre tips. The mean wavelength of these photons was measured to be 539 nm. The two measurements of intrinsic PDE differ by approximately 10% absolute PDE at the T2K operating over-voltage of 1.3 V. In order to determine if these two measurements are in agreement the results are compared to a plot of PDE as a function of wavelength in the MPPC specification by Hamamatsu [65] shown as a solid black line in Figure 7.20.

The PDE measurements provided by Hamamatsu have been produced by reading out the leakage current of an MPPC exposed to a calibrated light source. It is expected that this measurement will include all crosstalk, afterpulse and dark count effects and such will produce a highly elevated value compared to the intrinsic PDE of the device. It is observed that for an arbitrary normalisation factor of 0.66 the photocurrent curve can be scaled to match data points at 473 nm as measured using a LED and at 539 nm as

measured with Y-11 fibre. Also shown on this plot are two more data points, at 463 nm which was produced using a pulsed laser source and at 515 nm using an LED. All these data points are in agreement with each other assuming this normalisation factor.

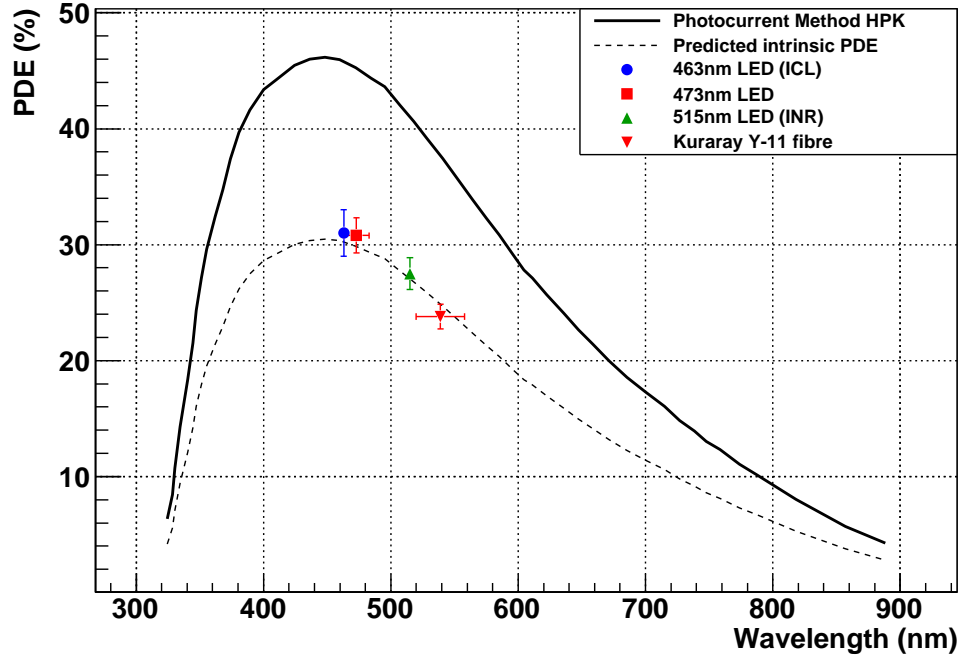


Figure 7.20: PDE measured by Hamamatsu reading out photocurrent of an MPPC. (Reproduced from [65]). The dashed line is an estimate of the intrinsic PDE by scaling the photocurrent measurement down by 0.66. Recent measurements made at ICL [97] and INR [98] along with those presented here are superimposed on the same axis. Datapoints shown in red are those presented during this thesis

If it is assumed that the black line is a similar measurement of PDE as obtained by examining the full shape of the spectrum and making Poisson fits as previously discussed, the scaling factor between the blackline and intrinsic PDE can be measured. Table 7.2 shows a summary of the measured PDE at the T2K operating over-voltage and the ratio between intrinsic and observed values. The mean ratio between observed and intrinsic PDE across all devices is 0.687. The difference between this and the arbitrary normalisation factor is small, and is possibly attributed to the length of the integration window used in these measurements, and the varying degrees of dark count rate which cannot be removed from the fit mean PDE measurement. A current leakage measurement effectively uses an

Device	Wavelength	Intrinsic PDE	Observed PDE	Ratio
TA3001	473 nm	$30.8 \pm 1.1\%$	$42.8 \pm 1.5\%$	0.70
TA3003	539 nm	$23.3 \pm 0.7\%$	$35.0 \pm 1.1\%$	0.67
TE8807	539 nm	$24.5 \pm 1.0\%$	$34.7 \pm 1.3\%$	0.71
TE8808	539 nm	$23.7 \pm 1.0\%$	$33.5 \pm 1.4\%$	0.71

Table 7.2: Summary of all PDE measurements

infinite integration gate and so observes all afterpulsing of the device beyond the 200ns limit imposed by the measurement performed in this thesis.

With a mean PDE of $23.7 \pm 0.5\%$ to photons produced by Y-11 fibre, the MPPC will meet the specifications as set out in Section 6.2. The calibration of each Golden MPPC was deemed adequate and have been installed for cross-calibration purposes at the quality assurance stations.

The PDE of the device will effect the linearity of its response to an input signal, as discussed in Section 5.4. In terms of numbers of photoelectrons observed by an MPPC, it is expected that the MPPC will exhibit a 10% deviation from linear behaviour for 141 photoelectrons. This translates into a input intensity of 414 photons if considering the PDE of the device including dark count, crosstalk and afterpulsing, and 602 photons if considering the intrinsic PDE. Figure 7.21(a) shows the deviation from linearity in terms of photoelectrons, it is observed for the dynamic range specified in Table 6.2 of 350 photoelectrons, there will be an expected 22% deviation from linear behaviour for a output signal of this magnitude.

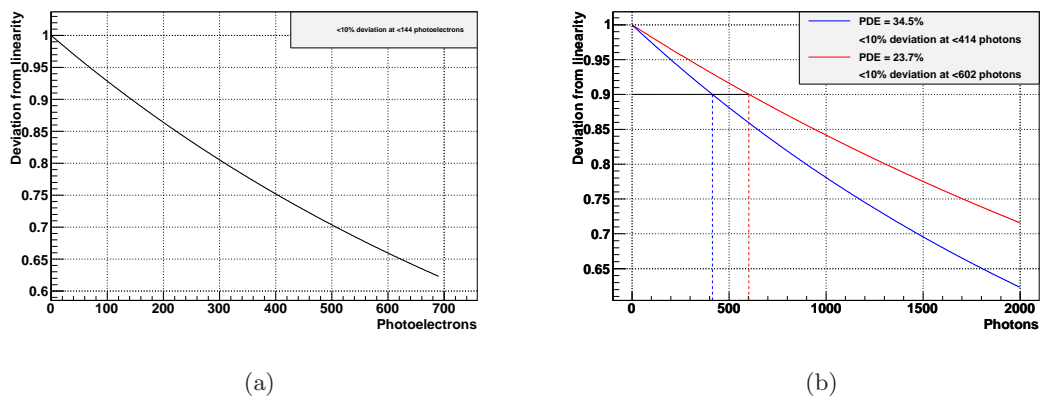


Figure 7.21: Deviations from linearity for the 1.3 x 1.3 mm MPPC, (a) shows deviation in terms of photoelectrons and (b) shows deviation in terms of input photons

Chapter 8

Conclusion

The development of the GAMPD has proceeded with haste over the last 5 years with a range of devices becoming commercially available. The GAMPD used by the T2K experiment will be the Multi-Pixel Photon Counter developed and produced by Hamamatsu Photonics. It is a custom 1.3 x 1.3 mm device composed of 667 pixels housed in ceramic packaging. The detector will employ over 43,000 MPPCs to read out 1 mm diameter Kuraray wavelength shifting fibres passed through the center of plastic scintillator bars. During this thesis basic operating parameters have been extracted for 3 GAMPDs for the purpose of aiding device selection for the ND280 ECal subdetector. The MPPC was chosen by the collaboration based upon the stability and maturity of the device in this and other studies made by the T2K collaboration. It is a requirement of the ECal to understand the operating parameters of all the MPPCs used to instrument its optical channels to a high degree of detail. The MPPC is observed to operate at a voltage of approximately 70 V and produce a gain of 7.5×10^5 at an over-voltage of 1.3 V. The observed dark count rates for the sample presented are <1 MHz at the maximum tested over-voltage of 1.6 V and <0.77 MHz at 1.3 V.

For quality assurance studies of all ECal devices, three ‘Golden’ MPPC with well calibrated absolute photon detection efficiency were chosen such that relative measurements could be made against them. In order to measure absolute photon detection efficiency it was an experimental setup was developed and studied in order to understand each component and the effect it plays on the measurement. A detailed study of the photon acceptance of the

MPPC in comparison to a calibration detector with an area of 1 cm^2 has been performed for two operating configurations, the first using a raw LED flash and the second using the LED to excite a length of wavelength shifting fibre. In the first configuration, a geometrical calculation showed that for measurements taken using a LED light source a simple ratio of device area may be used. The MPPC achieves an acceptance of 0.0169% for a LED distance of $>150 \text{ mm}$. In the second configuration, a generator was developed in GEANT4 allowing the simulation of photons emerging from a fibre tip. This allowed the coupling between the fibre and MPPC to be studied. It was found that the MPPC typically achieves an acceptance of $94.0 \pm 0.1\%$ when coupled to a 1 mm diameter fibre. To support this result, the acceptance of a smaller $1.0 \times 1.0 \text{ mm}$ MPPC was studied and compared to that of the $1.3 \times 1.3 \text{ mm}$ MPPC. A light yield increase of approximately 25% was predicted and measured experimentally.

The absolute intrinsic photon detection efficiency of a single MPPC was measured at 473 nm using an LED and found to be,

$$32.0 \pm 1.1\%.$$

When measured at 439 nm using photons produced by a length of wavelength shifting fibre, the photon detection photon detection efficiency decreases to a value of,

$$23.7 \pm 0.5\%.$$

With the addition of dark count, crosstalk and crosstalk the mean photon detection efficiency of the MPPC is increased by approximately 46% to $34.5 \pm 0.7\%$. The expected deviation of the output signal from linear behaviour is expected at a level of 22% for an 350 photoelectron signal and may be corrected for. The measured photon detection efficiency is in agreement with similar measurements taken by other T2K collaborators and with Hamamatsu Photonics datasheet information. The intrinsic photon detection efficiency, along with all operating parameters, will meet the specifications set out by the ECal group.

References

- [1] T2K Collaboration. T2k nd280 conceptual design report. 2005, URL=<http://www.nd280.org/tpc/documents/cdr.pdf>.
- [2] W. Pauli, 1930. Letter sent to the Tübingen conference.
- [3] C.L.Cowan *et al.* Detection of the free neutrino: A confirmation. *Science*, 124:103, 1956.
- [4] T. D. Lee and C. N. Yang. Theoretical discussions on possible high-energy neutrino experiments. *Phys. Rev. Lett.*, 4(6):307–311, Mar 1960.
- [5] Danby *et al.* Observation of high-energy neutrino reactions and the existence of two kinds of neutrinos. *Phys. Rev. Lett.*, 9(1):36–44, Jul 1962.
- [6] Nakamura Mitsuhiro. Result from donut – direct observation of ν_τ interaction-. *Nuclear Physics B - Proceedings Supplements*, 77(1-3):259 – 264, 1999.
- [7] W.B. Rolnick. *The Fundamental Particles and Their Interactions*. Addison-Wesley, 1994.
- [8] F. Halzen and A.D. Martin. *Quarks & Leptons : An Introductory Course in Modern Particle Physics*. John Wiley & Sons, 1984.
- [9] J.N. Bahcall. Solar neutrinos. i. theoretical. *Phys. Rev. Lett.*, 12(11):300–302, Mar 1964.
- [10] J.N. Bahcall *et al.* New Solar Opacities, Abundances, Helioseismology, and Neutrino Fluxes. *The Astrophysical Journal*, 621:L85–L88, mar 2005.
- [11] Raymond Davis, Don S. Harmer, and Kenneth C. Hoffman. Search for neutrinos from the sun. *Phys. Rev. Lett.*, 20(21):1205–1209, May 1968.

- [12] C. L. Cowan *et al.* Solar neutrinos: A scientific puzzle. *Science*, 191:264–267, 1976.
- [13] B.T. Cleveland *et al.* Measurement of the Solar Electron Neutrino Flux with the Homestake Chlorine Detector. *The Astrophysical Journal*, 496:505, March 1998.
- [14] K.S. Hirata *et al.* Search for correlation of neutrino events with solar flares in kamiokande. *Phys. Rev. Lett.*, 61(23):2653–2656, Dec 1988.
- [15] J.N. Abdurashitov *et al.* The Russian-American Gallium Experiment (SAGE) Cr neutrino source measurement. *Phys. Rev. Lett.*, 77(23):4708–4711, Dec 1996.
- [16] T. A. Kirsten. Gallex solar neutrino results. *Progress in Particle and Nuclear Physics*, 40:85 – 99, 1998.
- [17] A.B. McDonald. Solar neutrinos. *New Journal of Physics*, 6:121, 2004.
- [18] V. Gribov and B. Pontecorvo. Neutrino astronomy and lepton charge. *Physics Letters B*, 28(7):493 – 496, 1969.
- [19] Ziro Maki, Masami Nakagawa, and Shoichi Sakata. Remarks on the unified model of elementary particles. *Progress of Theoretical Physics*, 28(5):870–880, 1962.
- [20] Y. Fukuda *et al.* Atmospheric ν_μ / ν_e ratio in the multi-gev energy range. *Physics Letters B*, 335(2):237 – 245, 1994.
- [21] S. Fukuda *et al.* The super-kamiokande detector. *Nuclear Instruments and Methods in Physics Research Section A: Accelerators, Spectrometers, Detectors and Associated Equipment*, 501(2-3):418 – 462, 2003.
- [22] R. Becker-Szendy *et al.* Electron- and muon-neutrino content of the atmospheric flux. *Phys. Rev. D*, 46(9):3720–3724, Nov 1992.
- [23] D. Casper *et al.* Measurement of atmospheric neutrino composition with the imb-3 detector. *Phys. Rev. Lett.*, 66(20):2561–2564, May 1991.
- [24] Y. Ashie *et al.* Measurement of atmospheric neutrino oscillation parameters by super-kamiokande i. *Phys. Rev. D*, 71(11):112005, Jun 2005.
- [25] J. Boger *et al.* The sudbury neutrino observatory. *Nuclear Instruments and Methods in Physics Research Section A: Accelerators, Spectrometers, Detectors and Associated Equipment*, 449(1-2):172 – 207, 2000.

-
- [26] Q.R. Ahmad *et al.* Direct evidence for neutrino flavor transformation from neutral-current interactions in the sudbury neutrino observatory. *Phys. Rev. Lett.*, 89(1):011301, Jun 2002.
- [27] B. Aharmim *et al.* Independent measurement of the total active [sup 8]b solar neutrino flux using an array of [sup 3]he proportional counters at the sudbury neutrino observatory. *Physical Review Letters*, 101(11):111301, 2008.
- [28] Yuichi Oyama. K2K (KEK to Kamioka) neutrino oscillation experiment at KEK-PS. *hep-ex/9803014*, 1998.
- [29] MINOS Collaboration. Minos technical design report, 1998.
- [30] E. Aliu *et al.* Evidence for muon neutrino oscillation in an accelerator-based experiment. *Phys. Rev. Lett.*, 94(8):081802, Mar 2005.
- [31] M.H. Ahn *et al.* Measurement of neutrino oscillation by the k2k experiment. *Physical Review D (Particles and Fields)*, 74(7), 2006.
- [32] P. Adamson *et al.* Measurement of neutrino oscillations with the minos detectors in the numi beam. *Physical Review Letters*, 101(13):131802, 2008.
- [33] S. Abe *et al.* Precision measurement of neutrino oscillation parameters with kamland. *Physical Review Letters*, 100(22):221803, 2008.
- [34] M. Apollonio *et al.* Search for neutrino oscillations on a long base-line at the CHOOZ nuclear power station. *Eur. Phys. J.*, C27:331–374, 2003.
- [35] G. L. Fogli, E. Lisi, A. Marrone, A. Palazzo, and A. M. Rotunno. Neutrino oscillations, global analysis and theta(13). *arXiv/0905.3549*, 2009.
- [36] F. Ardellier *et al.* Double Chooz: A search for the neutrino mixing angle theta(13). *hep-ex/0606025*, 2006.
- [37] Xinheng *et al.*, Guo. A precision measurement of the neutrino mixing angle theta(13) using reactor antineutrinos at Daya Bay. *hep-ex/0701029*, 2007.
- [38] KamLAND Collaboration. Precision measurement of neutrino oscillation parameters with kamland. *Physical Review Letters*, 100(22), 2008.

- [39] M. Apollonio *et al.* Search for neutrino oscillations on a long base-line at the chooz nuclear power station. *The European Physical Journal C - Particles and Fields*, 27(3), 2004.
- [40] G. L. Fogli, E. Lisi, A. Marrone, A. Palazzo, and A. M. Rotunno. Hints of $\theta(13) > 0$ from global neutrino data analysis. *Physical Review Letters*, 101(14), 2008.
- [41] Japan proton accelerator research complex. 2-4 Shirane Shirakata, Tokai-mura, Naka-gun, Ibaraki 319-1195, Japan, URL=<http://j-parc.jp/index-e.html>.
- [42] ND280 Collaboration. ND280 review document for IPNS, 2006. URL=<http://www.nd280.org/convenors/ND280\%20Review\%20document\%202006/ND280-review-Tech.pdf>.
- [43] A. Izmaylov *et al.* Scintillator counters with WLS fiber/mppc readout for the side muon range detector (SMRD) of the T2K experiment. *arXiv:0904.4545v1*, 2009.
- [44] R. Terri. Status of the t2k experiment. *Nuclear Physics B - Proceedings Supplements*, 189:277 – 281, 2009. Proceedings of the Tenth International Workshop on Tau Lepton Physics.
- [45] Y. Giomataris *et al.* Micromegas: a high-granularity position-sensitive gaseous detector for high particle-flux environments. *Nuclear Instruments and Methods in Physics Research Section A: Accelerators, Spectrometers, Detectors and Associated Equipment*, 376(1):29 – 35, 1996.
- [46] M Di Marco (for the T2K TPC group). Test-bench for the characterization of micromegas modules for the t2k nd280 tpc. *Journal of Physics: Conference Series*, 65:012019 (6pp), 2007.
- [47] W. R. Leo. *Techniques for Nuclear and Particle Physics Experiments*. Springer-Verlag, 1987.
- [48] Kuraray. Ote Center Building,1-1-3, Otemachi, Chiyoda-ku, Tokyo 100-8115, Japan, URL=<http://http://www.kuraray.co.jp>.
- [49] Du pont. DuPont,P.O. Box 80728, Wilmington, DE 19880-0728, USA, URL=<http://www2.dupont.com>.

- [50] R. Becker-Szendy *et al.* Imb-3: a large water cherenkov detector for nucleon decay and neutrino interactions. *Nuclear Instruments and Methods in Physics Research Section A: Accelerators, Spectrometers, Detectors and Associated Equipment*, 324(1-2):363 – 382, 1993.
- [51] R. A. Wendell. *Three Flavor Oscillation Analysis of Atmospheric Neutrinos in Super-Kamiokande*. PhD thesis, University of North Carolina, 2008.
- [52] Y. Fukuda *et al.* Measurement of a small atmospheric ratio. *Physics Letters B*, 433(1-2):9 – 18, 1998.
- [53] I. E. Tamm and I. M. Frank. *Comptes Rendus Acad. Sciences USSR*, 14, 107(14):105, 1937.
- [54] S. Kasuga. *Observation of a Small ν_μ / ν_e Ratio of Atmospheric Neutrinos in Super-Kamiokande by the Method of Particle Identification*. PhD thesis, University of Tokyo, 1998.
- [55] Y. Koshio. *Study of Solar Neutrinos at Super Kamiokande*. PhD thesis, University of Tokyo, 1998.
- [56] Erik H. M. Heijne. Semiconductor detectors in the low countries. *Nuclear Instruments and Methods in Physics Research Section A: Accelerators, Spectrometers, Detectors and Associated Equipment*, 509(1-3):1 – 16, 2003. Proceedings of the 4th International Workshop on Radiation Imaging Detectors.
- [57] S.M. Sze. *Physics of Semiconductor Devices*. John Wiley & Sons, 1981.
- [58] C. T. Sah *et al.* Carrier generation and recombination in p-n junction and p-n junction characteristics. *Proc. Inst. Radio Engrs*, 45(1822), 1957. Proceedings of the 4th International Workshop on Radiation Imaging Detectors.
- [59] G. Parker. *Introductory Semiconductor Device Physics*. Taylor & Francis, 2004.
- [60] C.Y. Chang, S.S. Chiu, and L.P. Hsu. Temperature dependence of breakdown voltage in silicon abrupt p-n junctions. *Electron Devices, IEEE Transactions on*, 18(6):391–393, Jun 1971.
- [61] Wolfgang W. Gärtner. Depletion-layer photoeffects in semiconductors. *Phys. Rev.*, 116(1):84–87, Oct 1959.

- [62] E.D. Palik. *Handbook of Optical Constants of Solids*. Academic Press, 1985.
- [63] P. Buzhan *et al.* An advanced study of silicon photomultiplier. *ICFA Inst. Bulletin*, 23, 2003.
- [64] D. Renker. New trends on photodetectors, for. *Nuclear Instruments and Methods in Physics Research Section A*, 571(1-2):1 – 6, 2007.
- [65] Hamamatsu photonics k. k, solid state division. 1126-1, Ichino-cho, Higashi-ku, Hamamatsu City, Shizuoka Pref., 430-8587, Japan, URL=<http://www.hamamatsu.com>.
- [66] M. Kapusta *et al.* Breakthrough in quantum efficiency of bi-alkali photocathodes pmts. *Nuclear Science Symposium Conference Record, 2007. NSS '07. IEEE*, 1, 26 2007-Nov. 3 2007.
- [67] H. Dautet *et al.* Photon counting techniques with silicon avalanche photodiodes. *Appl. Opt.*, 32(21):3894–3900, 1993.
- [68] W. G. Oldham *et al.* Triggering phenomena in avalanche diodes. *Transactions on Electron Devices, IEEE*, 19(9), 1972.
- [69] J. Barral. Study of silicon photomultipliers. Internship report for Max Planck Institut für Physik, URL=<http://www.stanford.edu/~jbarral/Downloads/StageOption-Rapport.pdf>.
- [70] I. Rech *et al.* A new approach to optical crosstalk modeling in single-photon avalanche diodes. *Photonics Technology Letters, IEEE*, 20(5), 2008.
- [71] A. Lacaita *et al.* On the bremsstrahlung origin of hot-carrier-induced photons in silicon devices. *Transactions on Electron Devices, IEEE*, 40(3), 1993.
- [72] S. Cova *et al.* Trapping phenomena in avalanche photodiodes on nanosecond scale. *Electron Device Letters, IEEE*, 12(12), 1991.
- [73] National semiconductor. 2900 Semiconductor Drive, Santa Clara, CA 95051, USA, URL=<http://www.national.com>.
- [74] Texas instruments incorporated. 12500 TI Boulevard, Dallas, Texas 75243, USA, URL=www.ti.com.

-
- [75] Ortec. 801 South Illinois Avenue, Oak Ridge, TN 37830, USA URL=<http://www.ortec-online.com>.
- [76] Lecroy corporation. 700 Chestnut Ridge Road, Chestnut Ridge, NY, 10977-6499, URL=<http://www.lecroy.com>.
- [77] Hameg instruments. HAMEG Instruments GmbH, Industriestr. 6, D-63533 Mainhausen, Germany, URL=<http://www.hameg.com>.
- [78] The ANTARES Collaboration. The antares optical module. *Nuclear Instruments and Methods in Physics Research A*, 484(1-3), 2002.
- [79] J. S. Kapustinsky *et al.* A fast timing light pulser for scintillation detectors. *Nuclear Instruments and Methods in Physics Research A*, 241(1-2), 1985.
- [80] G. Barker. Private communication.
- [81] National instruments corporation. 11500 N Mopac Expwy, Austin, TX 78759-3504, USA, URL=<http://www.ni.com/labview>.
- [82] Photonique sa. ch. du Grand-Puits 38, 1217 Meyrin, Switzerland, URL=<http://www.photonique.ch>.
- [83] M. Taguchi. Development of multi-pixel photon counters and readout electronics. Master's thesis, Department of Physics, Kyoto University, 2007.
- [84] Sensl. Lee House, Riverview Business Park, Bessboro Road, Blackrock, Cork URL=<http://www.sensl.com>.
- [85] F. Rademakers R. Brun. Root - an object oriented data analysis framework. *Nuclear Instruments and Methods in Physics Research A*, 389(1-2), 1997.
- [86] J.H. Friedman. In *CERN School of Computing*, 1974.
- [87] Y. Kudenko. Study of MRS photodiodes for T2K experiment. In *International Workshop on new Photon-Detectors*, volume PD07, 2007.
- [88] A. Heering *et al.* Large-area SiPMs for the CMS hadron outer calorimeter. *Nuclear Science Symposium Conference Record, 2007. NSS '07. IEEE*, 2:1545–1550, 26 2007-Nov. 3 2007.

- [89] P. K. Lightfoot. Characterisation of a silicon photomultiplier device for applications in liquid argon based neutrino physics and dark matter searches. *Journal of Instrumentation*, 3(10):P10001, 2008.
- [90] Newport corporation. Unit 7, Library Avenue Harwell Science & Innovation Campus Didcot, Oxfordshire, OX11 0SG, UK, URL=<http://www.newport.com>.
- [91] Agilent technologies. South Queensferry, West Lothian EH30 9TG, United Kingdom, URL=<http://www.home.agilent.com>.
- [92] S. Agostinelli *et al.* G4—a simulation toolkit. *Nuclear Instruments and Methods in Physics Research Section A: Accelerators, Spectrometers, Detectors and Associated Equipment*, 506(3):250 – 303, 2003.
- [93] M. Bryant. Plastic scintillators for the T2K Fine-Grained detector. Master’s thesis, The University Of British Columbia, 2007.
- [94] W. Rasband. Imagej. URL=<http://rsb.info.nih.gov/ij/>.
- [95] Solid State Division Hamamatsu Photonics K. K. Delivery specification sheet prototype mppc, type no s10362-13-050c. Document addressed to T2K collaboration Dec 2007.
- [96] S. Gomi. private communication.
- [97] A. Vacheret. Private communication. *note: collaborative measurement of pde made at imperial collage london.*
- [98] Y. Kudenko. Private communication. Institute for Nuclear Research.